Mass loss modulation
in dust forming stellar winds

Yvonne Simis

CONTENTS

MASS LOSS MODULATION
IN DUST FORMING STELLAR WINDS

PROEFSCHRIFT

ter verkrijging van
de graad van Doctor aan de Universiteit Leiden,
op gezag van de Rector Magnificus Dr. D.D. Breimer,
hoogleraar in de faculteit der Wiskunde en
Natuurwetenschappen en die der Geneeskunde,
volgens besluit van het College voor Promoties
te verdedigen op woensdag 10 oktober 2001
te klokke 15:15

door

Yvonne Johanna Wilhelmina Simis

geboren te Purmerend in 1972

PROMOTIECOMMISSIE

Promotor   Prof. dr. V. Icke

Referent   Prof. dr. L.B.F.M. Waters   (Universiteit van Amsterdam)

Overige leden   Prof. dr. E.F. van Dishoeck
                Dr. C. Dominik   (Universiteit van Amsterdam)
                Prof. dr. H.J. Habing
                Prof. dr. H.J.G.L.M. Lamers   (Universiteit Utrecht)
                Prof. dr. G.K. Miley
                Prof. dr. D. Schönberner   (Astrophysikalisches Institut Potsdam)
                Prof. dr. C. Waelkens   (Katholieke Universiteit Leuven)
                Dr. J.M. Winters   (Max-Planck-Institut für Radioastronomie, Bonn)

voor mijn ouders

CONTENTS

1

DUST FORMING STELLAR WINDS

One attractive thing about investigating the lives of stars is the fact that all stereotypes about stars seem to be true; the small ones live their lives quietly and calmly, they do not use a lot of energy and they become very old and die peacefully, almost unnoticed. The tough and heavy guys, on the other hand, are brutally polluting their environments, possess all the gold and uranium, and live fast and die young (and very violently). Neither the small and silent nor the violent types are the subject of this thesis. This thesis is about the big middle class. While the middle class types are swelling up towards the end of their lives, their careers are far from being boring. On the contrary. As they get older, they become more and more productive. In fact, a major part of the silicates, that we on rocky planet Earth use to produce glass and computers, and the carbon that is in our trees, bodies, candy bars and that makes our skates fit comfortably, has been produced by these aging stars. But, they are not just hard workers. It is a well known fact that in nature beauty comes with age (Andersen, 1844; Carle, 1969), and this is surely true for these stars.

During the last decade, spectacular new observations of the final phases of stellar lives have become possible. Three examples of observations of aging stars can be found on the cover of this thesis. The first picture shows the star IRC +10216 (Mauron & Huggins, 1999), which is blowing away its outer layers, in the form of a massive stellar wind. Doing so, it forms concentric shells. Their presence indicates that the mass loss rate is not constant in time. The second and third picture show slightly older objects called the Egg Nebula, or CRL 2688 (Sahai et al., 1998), and the Cat's Eye Nebula, or NGC 6543 (Balick et al., 2001). After having blown away their envelopes, they are now illuminating and ionizing the nebulae they created. The detailed observations of these reveal the presence of a wealth of small scale structures. With a smaller telescope, and therefore in earlier days, these nebulae looked like round, greenish disks. This explains why we still call them Planetary Nebulae.

With the research presented in this thesis, we aim to contribute to the knowledge of the process of aging of ordinary stars, of the type of our sun and up to eight times heavier. In particular, we are interested in how a star, with its simple spherical shape, can turn into a weird shaped nebula, with all kinds of clumps, shells and more messy structure in it. We present how we found out, carrying out numerical hydrodynamics simulations, about the origin of the concentric shells seen around dying stars. It turns out that, indeed, the mass loss rate is not always constant. This is caused by the fact that the gas is not directly blown away from the star. The small, solid 'dust grains', that form in the cool envelopes of aging stars, intercept radiation from the star and

are pushed outward. They drag the gas along. The force they exert on the gas is not always constant: it depends on e.g. the density of the gas and the size of the grains. This can lead to modulated outflow. To understand why, just think of why it is not very comfortable to ride in a carriage that is being pulled by a horse on an elastic band, instead of on a solid bar.

A major amount of time was spent on the development of a special purpose hydrodynamics code for dust forming stellar winds. The innovative aspect of our code is that we allow the grains that form in the envelope to drift through the gas. Comparing with previous calculations, we have replaced the solid bar by an elastic band and have thus introduced an extra degree of freedom. The code is based on the FCT/LCD method for solving the differential equations of gas flow and it uses centered differencing. We assume spherical symmetry and use an Eulerian grid. Not just the flow of gas and dust are calculated, but also their chemical reactions and (in a simple form) their interaction with the stellar radiation. Chapter 2 is entirely devoted to an extensive description of the background of and the physics going into the hydrodynamics calculations. In Chapter 3 and 4 we discuss the results produced by the code and we attempt to explain how and when mass loss modulation in stellar winds arises.

This first chapter has two aims: to provide the framework for the rest of the thesis and to summarize the main results in it. In the first three sections, we give a general introduction to the topic of dusty stellar winds. We briefly review the stellar evolution theory concerning the last stages of a stars life in Section 1.1. Next, in Section 1.2, we inform the reader about the role of dust grains in astrophysics and in particular in the final stages of intermediate mass stars. Thereafter, in Section 1.3, we discuss some basic stellar wind theory, thereby presenting the equations that underly the numerical work presented in the rest of this work. In the final section of this introduction we give an outline of this thesis and we summarize the main results.

1.1 FROM MAIN SEQUENCE TO PLANETARY NEBULA

Stars are born from gas clouds that collapse under the influence of gravitation. Due to the enormous compression, the temperature and density in the core of the proto–star become high enough to start hydrogen fusion. From that moment we speak of a star: a gas sphere in which nuclear fusion takes place under the influence of self-gravitation. Let us, from now on, focus on the life of a star like our sun. The mass of a star at birth more or less determines its fate. Another important aspect for the evolution of a star is its place of birth: a star inherits the chemical composition of the environment in which it was born. Although most of the matter that collapses into a star is hydrogen, the small fraction of heavier elements influences the long term evolution. A star of 1 $M_\odot$ takes approximately 10^{10} years (which is 80% of its total life time) to convert all the hydrogen in its core, through the PP chain–reactions (slightly more heavy stars, $\gtrsim$ 5 $M_\odot$, 'burn' their hydrogen in the CNO cycle), into helium. During this time, its luminosity and temperature remain approximately constant. Hence, the star just sits on the Main Sequence (MS) of the Hertzsprung–Russell (HR) diagram, that describes the evolution of its luminosity and temperature.

Figure 1.1 shows the HR diagram for a sun-like star. The star moves away from the
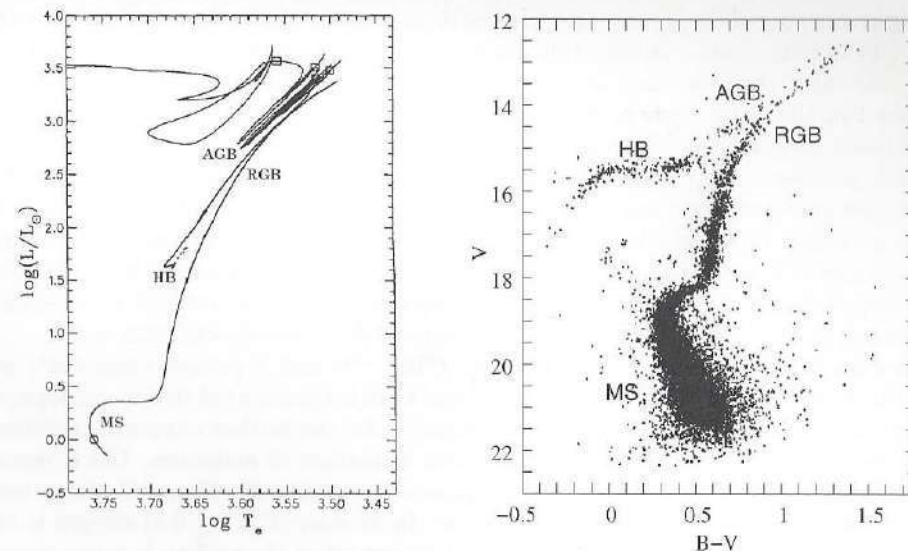
FIGURE 1.1: left: Hertzsprung–Russell diagram with the computed long term evolution of the sun. The current luminosity and temperature are indicated with a circle (adapted from Sackmann et al.(1993), in a slightly modified version by Schöier (2000)). right: observed colour-magnitude diagram of the globular cluster M3 (adapted from Buonanno et al. (1994)).

MS when no more hydrogen is left in its core so that the nuclear fusion process stops and the core contracts. Therefore, the hydrogen shell just outside the core is pulled towards the hot center and becomes hot enough to burn. This heats the outer layers of the star, which expand and cool down. The star is now redder and more luminous than before: it has moved up to the Red Giant Branch (RGB) of the HR diagram. Meanwhile, the contracting core of the Red Giant gradually gets hotter and hotter and eventually reaches helium ignition temperature ($\sim 10^8$ K). This leads to a further increase of the temperature but not of the pressure, because the helium core is degenerate. The resulting runaway process of helium burning and further heating amounts to the *helium flash*. Thereafter, the star reaches a phase of quiet core helium burning and shell hydrogen burning. The luminosity and radius of the star have decreased. The position in the HR diagram depends on the chemical composition of the object. Stars of low metalicity (0.2 – 0.002 % heavy elements, population II stars) form a *Horizontal Branch* (HB) along which their exact position is determined by the mass, and hence by the amount of mass lost in the stellar wind during the RGB phase.

When almost all the helium in the core has turned into carbon, the nuclear processes in the center stop again and the evolutionary story sketched above is more or less repeated, but now with hydrogen burning replaced by helium burning and carbon products instead of helium products. The star again evolves towards a red giant stage, and this second giant phase is called the *Asymptotic Giant Branch* (AGB). On the early AGB, helium burns in a shell around the core and heats the outer layers so that the star expands and indeed turns into a giant again.

After one to ten million years, depending on the initial mass of the star, the outer

hydrogen burning shell ignites again. This is the onset of the Thermally Pulsating AGB (TP-AGB) phase. During this phase, which lasts 500 thousand to ten million years, the inner (helium), and the outer (hydrogen) shells burn alternatingly. Helium produced in the outer shell is deposited on the inner shell. There, the temperature and density increase and the triple alpha process ($3 \, {}^4\mathrm{He} \rightarrow {}^{12}\mathrm{C}$) is accelerated. This initiates another helium burning event: the *thermal pulse* or *helium shell flash*. Due to the energy released during a TP, the star expands and cools. Hence, the nuclear fusion processes in the shells stop (and the luminosity drops) until hydrogen ignites again to start the next thermal pulse cycle. Depending on the mass of the star on the main sequence, five to a hundred thermal pulses occur. During each of these cycles, the temperature of the star gradually decreases, while its luminosity increases.

After each TP, nucleosynthesis products (${}^4\mathrm{He}$, ${}^{12}\mathrm{C}$ and s–process elements[1]) are mixed into the envelope. The amount of carbon that is transported to the envelope, or rather the C/O abundance ratio there, is decisive for the further chemical evolution. Once the envelope is cool enough to allow the formation of molecules, CO is one of the first molecules to form. Since the CO molecule is stable, the C and O atoms used do not take part in further chemical reactions. In M stars (C/O $\lesssim$ 0.8) oxygen is left after CO formation and in C stars (C/O > 1.0) not all of the carbon is incorporated in CO. Hence, an M star develops a chemistry based on oxygen and the chemistry of the envelope around the C star is characterized by the presence of carbohydrates. Also the solid dust grains, that start to form as soon as the envelope has sufficiently cooled, either consist of silicates, in the case of an M star, or they are polyaromatic hydrocarbons or simply soot particles, if they are nucleated in the envelope of a C star.

In this thesis, we are mostly interested in the extended envelope in which the stellar wind originates during the evolution on the AGB and beyond. Above, we briefly mentioned the formation of grains. They are very important in driving the AGB wind. Dust grains intercept the stellar radiation in a wide range of wavelengths, get accelerated by radiation pressure, and drag the gas away from the star. AGB stars are known to be *Long Period Variables* (LPVs), with pulsation periods of 100-1000 days. These *stellar pulsations* originate in the outer photospheric regions and should not be confused with the thermal pulses (see above) which arise in the helium shell around the core. The stellar pulsation is also a driving force for the wind. In the first place because mechanical energy is pumped into the atmosphere, and second, because pulsations lead to shock waves that create density and temperature structures beneficial for grain formation.

AGB stars lose mass at a fairly high rate (up to $10^{-4} \, \mathrm{M_\odot \, y^{-1}}$). The velocities in the wind, however, are low ($\sim$ 10-30 km s^{-1}) so that AGB winds are dense. Stars with a main sequence mass in the range of one to eight solar masses are, on the AGB, stripped off to a mere $0.5 - 1.0 \, \mathrm{M_\odot}$. The bare core of the former giant star will eventually evolve into a white dwarf (WD).

A low or intermediate mass star leaves the AGB when the mass in the envelope has dropped to about 0.01 $\mathrm{M_\odot}$. The mass loss rate at that time has decreased a few orders of magnitude, compared to its maximum value on the TP-AGB, but the velocities in

the wind have increased. The naked white dwarf and the circumstellar shell that it has blown away on the AGB can no longer be called a star. The dwarf and shell together are called a *post-AGB* object.

The temperature of the white dwarf gradually increases during the post-AGB phase. The circumstellar shell becomes illuminated and ionized and is called a *Planetary Nebula* (PN). PNe have many different shapes and are amongst the most beautiful objects in the sky. The bipolar structure of a main fraction of the PNe can be explained if the slow and dense AGB wind is denser at the equator than at the poles. The fast post-AGB wind running into the donut shaped AGB nebula would then produce the observed bipolarity (Balick et al., 1987; Icke, 1988). The enormous progress made in observational techniques during the last decade, enables high resolution observations, especially at visible (HST) and X-ray (Chandra) wavelengths. The ISO satellite and its infrared spectrometers revealed the enormous chemical richness of evolved stellar objects. These new observations provide a wealth of information on the shape of and the smaller scale structure in PNe. Also on the basis of observations of post-AGB objects and even AGB stars (Marengo et al., 2001) it has become clear now that mass loss on the AGB is often not in the form of a smooth, stationary wind, as was assumed until recently.

1.2   DUST AROUND EVOLVED STARS

It is difficult to imagine a world without solids. It is therefore surprising that it took people so long to raise the question where solid matter comes from. More than two centuries ago Herschel made the first step to the answer of this question by first raising another question: "Why are there holes in the distribution of stars in the sky?". In the next two centuries people learned that in fact there were no holes but there was something blocking the light of the stars at some places in the sky. Hoyle & Wickramasinghe (1962) attributed the interstellar extinction to carbon dust grains that originated in the outflows of red giants. Nowadays it is commonly accepted that most grains, not just carbonaceous grains but also silicates, are formed in the atmospheres of late type stars. The grains escape from there in the stellar wind. This can be seen from Fig. 1.2, which shows the infrared spectra of the AGB star OH 26.5+0.6, the post-AGB object HD 161796 and the planetary nebula NGC 6302. The expansion, and hence the cooling, of the dust shell as a function of age is observed from the fact that the continuum of the PNe spectrum peaks at longer wavelengths than that of the post-AGB and the AGB object. Spectra like these provide a wealth of information on the composition, and hence the origin and the environment at the time of formation, of dust around late type stars. The broad absorption features at 10 and 18 micron for OH 26.5+0.6 are due to amorphous silicates. The narrower features around 23, 33 and 40 micron indicate the presence of crystalline silicates and those around 43 and 60 micron are caused by crystalline water ice. Note that the spectrum of NGC 6302 also shows a number of atomic lines.

The interstellar medium (ISM) is continuously being enriched with dust from stellar envelopes. In the ISM, grains can be destroyed by shocks and UV photons. A next generation of stars that forms from the ISM, consumes the molecules released in the

---

[1] *Slow* neutron capture onto heavy elements, for example strontium, zirconium, niobium, technetium (the 'light' s–process elements), and barium, lanthanum, cerium, neodymium ('heavy' elements) (c.f. Groenewegen (1993))
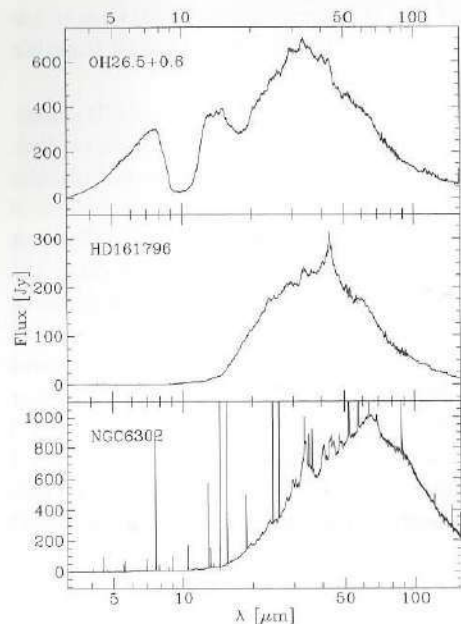
FIGURE 1.2: ISO spectra of an AGB star (OH 26.5+0.6), a post-AGB object (HD 161796) and a planetary nebula (NGC 6302). The redshift of the maximum of the emission from object to object indicates the expansion of the dust shell. The features at 10 an 18 micron are due to amorphous silicates. Those at 23, 33, 40, 43 and 60 are caused by crystalline silicates and water ice. The figure was provided by F.J. Molster.

final phases of the lives of their progenitors. Planets may form in the circumstellar disk that is the left over from the nebula in which the star formed. These stars on their turn will die, and further enrich the composition of the ISM.

Solids form through the condensation of supersaturated vapour: the pressure should be high enough and the temperature has to be quite low. Grains are sensitive to shocks and UV light, which easily destroy them. The environment, therefore, has an enormous influence on the life of the grain. Conversely, the presence of grains has a huge impact on the environment. Grains are good absorbers in a wide wavelength range and re-emit the incident radiation isotropically. Grains experience radiation pressure and are a means of converting radiation into kinetic energy. Also, small solids provide a location for chemical reactions. Summarizing, we see that when doing calculations in an area of the p–T plane in which dust grains may be present, one needs to take their presence into account since their evolution is intimately connected with the evolution of the environment itself. This is definitely the case for winds from AGB stars.

1.3 STELLAR WINDS

Almost all stars lose mass. For the sun this was first demonstrated by Parker (1958), see also MacGregor (1998). The mass loss rate of the sun is about 10^{-14} $M_\odot$ y^{-1}. This is small compared to the loss due to nuclear fusion, $\dot{M}_{\mathrm{nucl}} = L_\odot/c^2$, so the mass loss in the wind will have virtually no effect on the evolution.

Massive stars ($M \geq 30$ $M_\odot$) suffer high mass loss rates already at a younger age. Their stellar winds have been studied observationally for more than a century. Examples are luminous blue variables (LBVs), Wolf–Rayet (WR) stars, O stars and BA

supergiants. The clearest spectroscopic signatures of mass loss are the profiles of lines formed in the expanding atmosphere. The classical example for hot stars is the P Cygni profile, which has a redshifted emission 'bump' (due to stellar continuum photons that are scattered towards the observer) and a blue shifted 'trough' (photons initially heading for the observer are scattered out of the line of sight), see e.g. Fullerton (1997). Good observational indicators of dust driven mass loss are extended shells (see Fig. 1.2), gas phase CO and HCN emission lines and OH maser lines.

The rate at which a star loses mass and the time dependent behaviour of the wind are both connected to the position of the object in the HR diagram. In general the mass loss rate is low, $\dot{M} < 10^{-12}$ $M_\odot$ y^{-1}, for objects at the lower main sequence and increases with luminosity (up to 10^{-6}-10^{-4} $M_\odot$ y^{-1}). Several modes of mass loss can be distinguished: quasi-stationary; periodic and semi-regular; and episodic mass loss. Although there is a large variety in loss rates and modes, there are only two basic driving mechanisms for stellar winds: radiation and waves.

Winds from objects with a high luminosity are generally induced by radiation. Radiative acceleration goes via line absorption in the case of hot stars or via dust and molecular absorption in cooler stars. Wave energy input in the form of shocks (for LPVs and Miras) and acoustic and MHD waves (K Giants) drives the wind in pulsating stars. The fact that radiation driven outflows, especially for giants, show variability suggests that a cooperation of both driving mechanisms is quite common (Sedlmayr & Winters, 1997).

All types of winds, hot or cool, fast or slow, dense or dilute, radiation driven or pressure driven, can be described by a single basic physical formulation. The mass-continuity equation dictates that, in absence of sources, the matter that flows out of a certain shell has to flow into one of the adjacent shells. Accordingly,

$$\dot{M} = 4\pi r^2 \rho(r) v(r) \qquad (1.1)$$

Hence, if there are no sources or sinks of matter (e.g. due to dust formation) the mass loss rate is constant throughout the atmosphere for a stationary outflow. In this introductory section, we only discuss stationary solutions. We do this because this shows clearly the structure of the equations that are used in the time dependent calculations which are the actual topic of this thesis.

The equation of motion in the stationary wind is

$$v\frac{\mathrm{d}v}{\mathrm{d}r} = -\frac{1}{\rho}\frac{\mathrm{d}p}{\mathrm{d}r} - \frac{GM}{r^2} + f(r) \qquad (1.2)$$

where the first term on the right hand side is the outward force due to the gas pressure, the second term is gravity and the third term is an extra force. Assuming that the atmospheric gas can be described by the ideal gas law, the pressure derivative can be written as

$$\frac{1}{\rho}\frac{\mathrm{d}p}{\mathrm{d}r} = \frac{\mathcal{R}_g}{\mu}\frac{\mathrm{d}T}{\mathrm{d}r} + \frac{\mathcal{R}_g T}{\mu\rho}\frac{\mathrm{d}\rho}{\mathrm{d}r} \qquad (1.3)$$

Differentiation of Eq.(1.1) and substitution of this derivative and of Eq.(1.3) in Eq.(1.2) yields

$$\frac{\mathrm{d}v}{\mathrm{d}r} = v\left(\frac{2c_s^2}{r} - \frac{\mathrm{d}c_s^2}{\mathrm{d}r} - \frac{GM}{r^2} + f(r)\right) / \left(v^2 - c_s^2\right) \qquad (1.4)$$
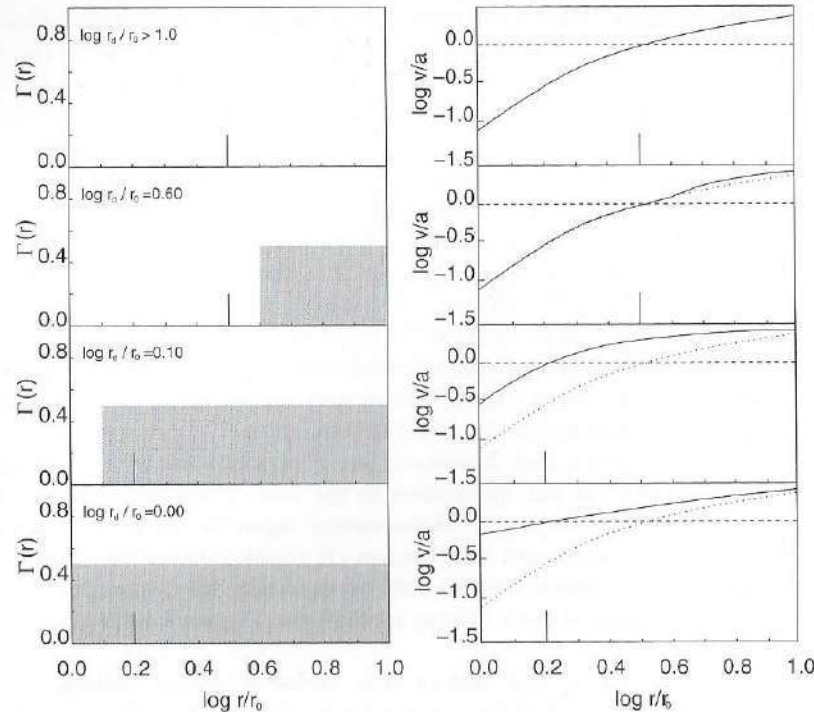
FIGURE 1.3: The effect of a force of the form $f(r) \propto \Gamma(r)/r^2$ with $\Gamma(r) = 0$ for $r < r_{\mathrm{d}}$ for various values of r_{d}. The panels at the left hand side show the distribution of $\Gamma(r)$. The frames at the right hand side show the actual flow velocity (solid line) and the flow velocity for the case $\Gamma(r) = 0 \; \forall \, r$ (dotted line) in terms of the velocity at the critical point (a). The location of this is annotated with a tick mark. This figure is adopted from Lamers & Cassinelli (1999) in a slightly modified form.

Here c_s is the isothermal sound speed:

$$c_{\mathrm{s}}^2 = \frac{\mathcal{R}_{\mathrm{g}} T}{\mu} \qquad (1.5)$$

If $v^2 = c_{\mathrm{s}}^2$, equation Eq.(1.4) has a singularity. Therefore there are six different types of solutions for the momentum equation. There is only one solution that can represent a stellar wind. This is the solution that starts subsonic and has a finite, supersonic, velocity at infinity. It passes through the critical point, the location of which is, in an isothermal envelope, given by

$$r_{\mathrm{c}} = \frac{GM}{2c_{\mathrm{s}}^2} - \frac{f(r_{\mathrm{c}})r_{\mathrm{c}}^2}{2c_{\mathrm{s}}^2} \qquad \text{if} \qquad v^2(r_{\mathrm{c}}) = c_{\mathrm{s}}^2 \qquad (1.6)$$

Note that in the isothermal case the critical point coincides with the sonic point $v = c_{\mathrm{s}}$ but that this is not true in general (Lamers, 1997).

The atmospheres that are studied in this thesis are definitely not isothermal. However, the isothermal case can be used to study the effect of the force $f(r)$. The expression for the location of the critical point, Eq.(1.6), shows that an outward force f

pulls the critical point inwards. Hence, $v = c_{\mathrm{s}}$ is reached at a lower value of r than was the case in the absence of the force. At the same time, the velocity gradient below the critical point decreases if a force f is added, see Eq.(1.4). Thus, everywhere below the critical point, addition of an outward force leads to an increase of the velocity. For stationary winds, in the absence of mass source terms, the mass loss rate is constant throughout the atmosphere (see Eq.(1.1)). This implies that an outward force results in an increase of the mass loss rate, when applied below the critical point. This condition is crucial. If f is of the form

$$\begin{aligned} f(r) &= 0 && \text{for} && r < r_d \\ f(r) &> 0 && \text{for} && r \geq r_d \end{aligned} \qquad (1.7)$$

and $r_{\mathrm{d}} > r_{\mathrm{c}}$, it is easily seen from Eq.(1.6) that the critical point is not pulled in. Hence, the force does *not* increase the mass loss rate in that case. It does, however, increase the velocity of the wind. This is due to the fact that for $r > r_{\mathrm{c}}$, a positive force will increase $\mathrm{d}v/\mathrm{d}r$. Figure 1.3 illustrates the effect of a force of the form $f(r) \propto \Gamma(r)/r^2$ on the location of the critical point and the on the mass loss rate. This increases if the force is nonzero in the subsonic region, as can be seen from the increased velocities (with respect to the case in which the force is not active in the subsonic region).

The name we gave the boundary of the region in which the force operates, r_d, suggests a connection with dust forming envelopes. Such a connection indeed exists: the region of dust formation in the circumstellar envelopes of AGB stars is quite precisely located and the critical point can always be found in the vicinity of this region.

Hence, the force due to radiation pressure on dust that drives the wind on the AGB is of the form Eq.(1.7). So, without having done any modelling one can already state that only the dust that forms below the critical point can lead to an increase in the mass loss rate. For this reason it is extremely important that numerical models cover the lower part of the atmosphere and not just the outer regions: the important physical processes occur between the photosphere and the sonic point. This too is the most challenging region for a numerical hydrodynamics code, since transonic winds are not trivial.

1.4 THESIS SUMMARY

In the previous sections, we have described the general context of the research in this thesis. We discussed the late evolutionary stages of solar-type stars and we mentioned the fact that they produce dust, which is essential for driving the stellar wind. Finally, the basics of stellar wind theory were given. In the current section, we first give a brief outline of the research (Section 1.4.1). Thereafter, we give a detailed summary of the main results. Section 1.4.2 is the summary of Chapter 2, which describes the implementation of various physical processes in a numerical hydrodynamics code for dust forming stellar winds. In Sections 1.4.3 and 1.4.4 we highlight the results from the calculations performed in Chapters 3 and 4. Ideas for future work on dust forming stellar winds as well as other applications of the hydrocode are discussed in Section 1.4.5.

1.4.1 RESEARCH GOALS AND SETUP

As is often the case in scientific research, the original research goal for the project resulting in this thesis was quite different from the results finally obtained. The aim of this work was to develop a new two dimensional numerical hydrodynamics code in order to investigate the transition from the AGB to the PNe phase. Two fluid flow was meant to be just a feature of the code, but when developing the one dimensional test version, grain behaviour appeared to have a major influence on the flow in the circumstellar envelope.

The extra degree of freedom introduced by grain drift turned out, to our surprise, to permit the genesis of a wind with a modulated mass loss rate at a time scale of the order of a hundred years. Without grain drift the outflow is much smoother, and only disturbed by the influence of the stellar pulsation, which has a much shorter time scale (typically a few hundred days).

The presence of concentric shells around certain PNe was known. Their origin was unknown, however, and their characteristic time scale could not be related to thermal pulses (which occur once every ten thousand to hundred thousand years) or stellar pulsations (every few hundred days). Linking our mass loss modulations with the observed shells was an attractive thought. The justification of this connection was provided by a paper by Mauron & Huggins (1999), very shortly after we first found mass loss variability in our AGB star calculations. They reported the detection of shell structure around the post-AGB object IRC+10216, and thereby suggested that the shells had formed when the star was still on, or had just left, the AGB.

To ensure that the mass loss modulations in our calculations would still exist by the time the gas had reached a distance equal to the size of the shells around IRC+10216, we extended our calculated grid out to approximately $1000\ R_*$. At this distance from the star, the match between the observed time scale and shell/inter shell density contrast and the values coming from our calculations was good.

It is often thought that, as soon as a certain effect occurs in a model, the modeller knows the origin of the effect. In our case this was not at all true. By comparing our calculations with and without drift, we could see that drift was important. But we could not immediately tell what caused the mass loss variability on this particular time scale. Our calculations are self-consistent. This means that we provide a set of initial parameters for the star and all the rest of the evolution of our model is generated within the calculation itself, without further interference. Therefore, the results generated with our hydrodynamics code can be as surprising to us as the details of an observation can surprise the observer.

The remaining time of the PhD project was spent on trying to find an answer to the questions of how and when exactly these shells can form around AGB stars. Doing so, one of the original aims of the research, namely generating a two dimensional hydrodynamics code, was deferred to a later time. Although not exactly in the way it was originally meant, the work described in this thesis has contributed to a deeper understanding of the evolution of an AGB star to a Planetary Nebula. We have shown that the concentric shells around PNe originate on the AGB. More important is the conclusion that something as easily overlooked as grain drift, can have profound implications for the dynamical gas evolution. More generally, we have shown that the circumstellar
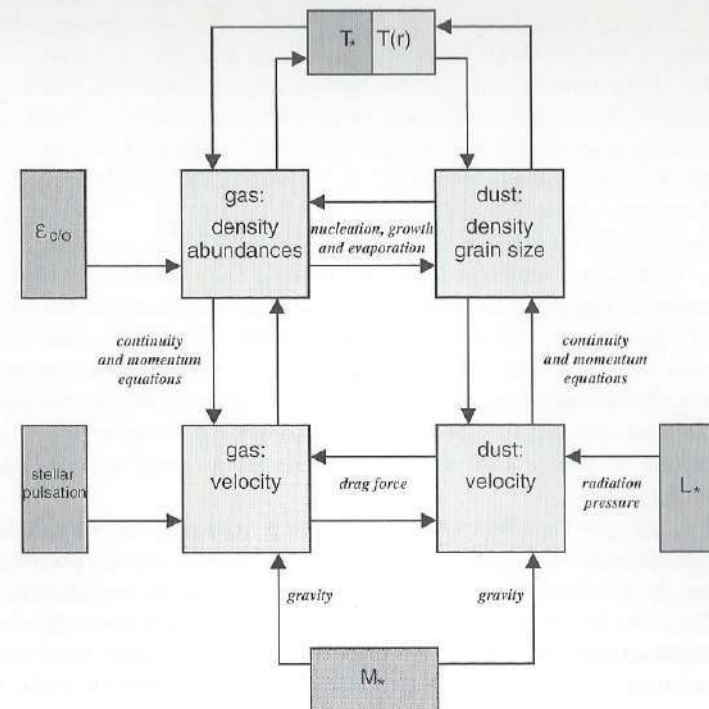
FIGURE 1.4: Schematic representation of the interdependencies between the various flow variables, forces and stellar parameters that are taken into account in our hydrodynamics code.

envelope is an extremely nonlinear environment in which various effects show extreme interdependencies. Hence, simple assumptions like a constant outflow velocity and a power law for the density distribution are very likely to underestimate and overlook the fascinating physical processes that take place in and are decisive for the evolution of the envelope.

In the remaining part of this summarizing chapter, we will first highlight the details of our hydrodynamics code, as described in Chapter 2. Thereafter, we answer the questions how and when (i.e. under which conditions) shell structure forms. The answers to these questions summarize the contents of the Chapters 3 and 4.

1.4.2 A NUMERICAL HYDRODYNAMICS CODE FOR DUST FORMING STELLAR WINDS

In Chapter 2, we provide the complete 'recipe' for our hydrodynamics code. After giving an introduction to the ideas behind numerical hydrodynamics, we present the details of the FCT/LCD (Flux Corrected Transport/Local Curvature Diminishing) method applied (Boris, 1976; Icke, 1991). A general code for fluid flow becomes a tool for a specific setup by the incorporation of source terms ('forces'). We perform calculations of the gas flow from dust forming stellar winds, in which grains can drift with respect to the gas. Hence, the source terms that we take into account are gravity; the nucleation, growth and evaporation of grains; radiation pressure on grains; the gas

pressure; and the drag force between grains and gas. For the implementation of the latter, we present a new method, based on individual gas-grain collisions. This allows us to keep track of the momentum transfer between both fluids on a much shorter time scale than the hydrodynamical time scale. It provides an expression for the drag force in which no assumptions about the value of the drift velocity have to be made. We discuss extensively the implementation of the forces, as well as the calculation of the equilibrium chemistry network for the gas.

With the ingredients mentioned, our code is self-consistent: to start a calculation, only the mass, luminosity, effective temperature and the pulsation period and amplitude of the central star and the carbon-to-oxygen abundance ratio in the envelope have to be provided. Results generated by the code involve all the relevant flow variables as velocities and densities (for gas and dust), grain size, pressure, temperature etc. The importance of self-consistency lies in the extreme interrelations that exist between the various chemical, dynamical and radiative processes in the envelope. An elaborate overview of various feedbacks and instabilities that are a result of these interrelations is given by Woitke (2001).

In Figure 1.4, we give an overview of the various relations between flow variables, forces and stellar parameters that are taken into account in our hydrodynamics code. From this figure, it is immediately clear that feedback loops and instabilities may show a different behaviour of even completely disappear if simplifying assumptions are made. Examples of assumptions that are often made are stationary flow, fixed grain sizes, a limited incorporation of the radiative processes and the neglect of grain drift. It is one of the main results of this work that we find a new instability loop, that causes modulated outflow if grain drift is taken into account. On the other hand, we too, make assumptions, e.g. we do not fully calculate the radiative transfer. This is inherent in modelling but it is important to be aware of the possible consequences.

To determine if our code is producing reliable results, we compare our calculations with the results from other groups. When doing so, we run our models in a single fluid mode, so omitting grain drift, because no two-fluid calculations with which we can compare our work exist. The results of our hydrodynamics code in single fluid mode appear to be comparable to previous results of other groups with similar codes.

1.4.3   How do shells around mass losing late-type stars form?

Chapter 3 contains the results of the first two-fluid calculation. For that, we used the stellar parameters of the extreme carbon star IRC +10216 (Winters et al., 1994). Without applying a time dependent inner boundary, or any other time dependent force, our calculations reproduce the concentric shells around this object. Both the time scale of the modulation and the shell/intershell density contrast found in our models match the observations. From these results, we conclude that the shells are formed by a hydrodynamical oscillation in the envelope, while the star is on the AGB. Responsible for this effect is a subtle mechanism, involving an intricate nonlinear interplay between gas-grain drift, grain nucleation, radiation pressure, and envelope hydrodynamics. In previous calculations by other groups the shells were not found because either grain drift, or a self-consistent description of the grain chemistry were not part of the model. Figure 1.4 shows that this can indeed prevent such an oscillation to take place.
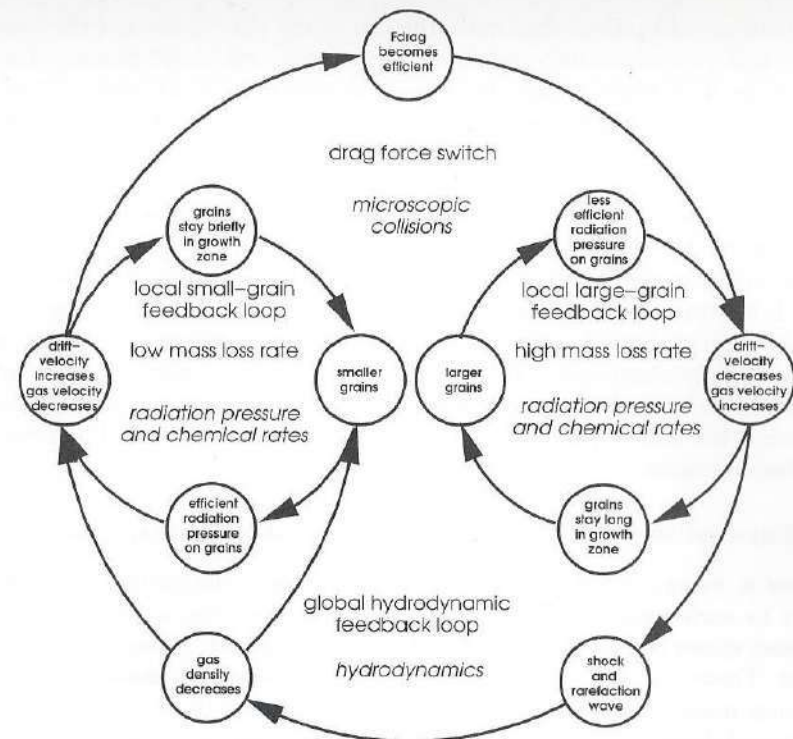
FIGURE 1.5: Schematic representation of the mechanism driving the mass loss variability. For details, see Section 1.4.3.

A schematic representation of the mechanism driving the mass loss variability is given in Fig. 1.5. The physical processes mentioned in it relate to the subsonic parts of the envelope. Only there, changes in the driving forces have effect on the mass loss rate. Obviously, there are two modes of outflow: low and high mass loss. The mass loss rate is low when the momentum transfer from grains to gas is inefficient. The velocity of the gas, in this phase, is low and we also refer to this phases a the 'slow phase'. The drift velocity of the grains is high, so the passage of the grains through the zone in which grain growth is efficient, is fast. This results in small grains. Small grains are very efficiently accelerated by the radiative force, because they have a large surface to mass ratio and because the grain extinction cross section is proportional to the geometrical cross section. So, during the phase of low mass loss, the average grain gradually becomes smaller and drifts faster.

If the mass loss rate is high, exactly the opposite feedback loop determines the fate of the grains. The momentum transfer rate is high so that the gas reaches high velocities (hence the 'fast phase') and the drift velocity of the grains is low. Hence, the grains move relatively slowly through the region of efficient grain growth. This results in rather large grains, with a large collision cross section and therefore a short mean free path. This, in turn, leads to a high momentum transfer rate and a further decrease of the drift velocity.

The two turn-around points, that mark the end of the slow phase and the onset of the fast phase and vice versa, turn out to be triggered by one single process: the sudden increase of the drag force at the end of the low mass loss (slow) phase. This increase is a result of the quadratic dependence of the drag force on the drift velocity: the increasing drift leads to an increase of the momentum transfer per gas-grain collision *and* it prevents a further decrease of the rate of collisions due to the declining grain size. The new efficiency of the drag force heralds the onset of the fast phase with its high mass loss rate. The suddenness of the transition involves the development of a shock and hence a rarefaction wave moving towards the stellar surface. This wave, that is a direct consequence of the onset of the drag force, brings a decrease of the gas density. As a result thereof, grains can no longer grow as efficiently as before and their mean free paths increase again. Hence, the onset of the slow phase is triggered by the same process that ended it during the previous cycle. The time scale of the mass loss modulation is the time required by the rarefaction wave to cross the dust forming part of the subsonic region.

1.4.4   WHEN DO SHELLS AROUND MASS LOSING LATE-TYPE STARS FORM?

In Chapter 4, we investigate under which circumstances the outflow of an AGB star is subject to such mass loss modulation. To do so, we run a series of 20 models, with various values for the stellar parameters T_*, L_* and M_*. Also, we include stellar pulsations. These do not disturb the mechanism that causes the mass loss modulation. We find that mass loss modulation is a transient phase on the AGB. With increasing luminosity and decreasing effective temperature and stellar mass, the outflow gradually becomes smoother. Hence: late AGB (high luminosity, low temperature) stars are more likely to have smooth outflows than early AGB (low luminosity, high temperature) stars. Note that the usage of 'late' and 'early' should not be taken too literally here: as a result of the thermal pulses both the temperature and the luminosity are not monotonic functions of time.
The density scale height at the bottom of the envelope,

$$\mathcal{H}(R_*) = \frac{\mathcal{R}_g T_*}{\mu g(R_*)} \propto \frac{L_*}{M_* T_*^3} \tag{1.8}$$

turns out to be a useful quantity to describe the variability behaviour. For early AGB stars it is low, and for late AGB stars it is high. Due to its dependence on the temperature and the luminosity (through the radius), the scale height is not a monotonic function of time either. But since the mass of an AGB star decreases, $\mathcal{H}(R_*)$ increases, although not strictly, with time.

The higher $\mathcal{H}(R_*)$, the flatter the density gradient. In combination with the relatively low effective temperature in late AGB stars, this enables the formation of grains at lower radii than in early AGB objects. Hence, the radiative force and the drag force are active at these low radii already. Consequently, in the AGB objects with a large density scale height, the sonic point is located closer to the star than in the AGB objects with a small scale height. Therefore, the subsonic region in the first is narrower. This leads to a shorter time scale for mass loss modulation. The amplitude of the modulation is constrained by the scale height as well. In objects with a large density

scale height, the density in the subsonic region is relatively high and the maximum drift velocity is therefore limited.

Summarizing, our calculations provide indications for the existence of a transient phase of mass loss modulation on the AGB. The mass loss both increases and becomes smoother towards the end of this phase. For objects in an earlier evolutionary phase, prior to this 'variability strip', it seems possible that only the grains are driven out. Note that we do not intend to claim that objects that are located below the variability strip in the HR diagram cannot have a dusty wind. It is very well possible that stars with mass loss that is not caused by radiation pressure on dust reach a state in which their envelope enables the formations of grains (Salpeter, 1974a). At the very end of the AGB, when, as a consequence of the rapidly increasing temperature, the scale height drops again, another phase of high grain drift might occur.

Finally, we compare our calculations *with* drift taken into account with an identical series of calculations *without* drift (single-fluid flow). We show why the importance of grain drift is easily overlooked: If grain drift is assumed to be negligible, so that gas and grains are forced to have the same velocity, the amount of momentum transfer to the gas is artificially kept high. This leads to a relatively large density in the subsonic region. In such an environment, decelerating collisions with the gas occur frequently. Consequently, the drift velocity of the grains is low and the neglect of grain drift *seems* justified.

1.4.5   FUTURE WORK

The results obtained with our hydrodynamics code have provided an explanation for the occurence of spherical shells around (post-)AGB objects and PNe. Moreover, from the fact that these shells form while the star is still on the AGB we gained new insights in its long term evolution. Still, the detailed images and spectra that have become available during the last decade, show much that we cannot explain. To improve our understanding of the late stages of stellar evolution of solar-type stars, we need to extend our models. There are many ways to make the hydrodynamics code used in this research more realistic, we mention three of them here.

First, the implementation of the physical processes that are taken into account could be improved. E.g. one could take into account the complete grain size distribution, instead of assuming all grains to have the average grain size. Also the interaction of the radiation field with the gas and the dust could be improved by simultaneously solving the hydrodynamics equations and the full radiative transfer problem.

Most PNe are far from being spherically symmetric. Hence, in order to fully understand the transition from an AGB star into a PN, hydrodynamical simulations in more dimensions are the way to proceed. Two dimensional hydrodynamical calculations of PNe have been succesfull in explaining the bipolar shape of many of them (Balick et al., 1987; Icke, 1988), assuming the presence of a donut shaped AGB nebula. By extending our hydrodynamics to higher dimensions, we may actually learn what causes the formation of this equatorial density enhancement at the end of the AGB.

The final point of improvement to be mentioned here is the time coverage of the model calculations. In Chapter 4, we have drawn conclusions about the long term evolution of stars on the AGB, on the basis of calculations that did not even cover

a complete thermal pulse cycle. We have used external prescriptions for the basic stellar parameters (mass, temperature, luminosity etc.). In reality, there is a mutual dependence between the properties of the central star and the envelope. The most trivial example is of course the influence of the mass loss rate on the mass of the star. When performing calculations which cover a number of thermal pulse cycles, the influence of the mass loss on the central star must be taken into account. Especially in combination with stellar evolution calculations, this will provide new insights in the long term evolution on the AGB and beyond.

Combining the suggested improvements will very likely contribute to a better understanding of the late stages of stellar evolution. However, an extention of a numerical code brings about an increase in the CPU time required to perform the calculations. This is definitely the case for the improvements proposed above, so that combining them is not yet possible with the current generation of computers.

We have seen that taking into account grain drift in dusty stellar winds leads to instabilities that were unknown before. It is very likely that two fluid flow is also important for other astrophysical problems in which both gas and dust are present. As a first step towards a broader application of our hydrodynamics code we have adapted our code for the calculation of gas flow in circumstellar disks (Kamp & Simis, 2001). The aim of these calculations is to see if the grains can completely decouple from the gas. In that case, the grains are driven out by the radiation pressure, but the gas is not. In a viscous disk, this may lead to the re-accretion of the gas. Since the re-accretion takes places after the formation of dust, the gas is depleted in metals. This scenario might explain the extremely low metal abundances observed for a number of post-AGB objects and for the λ Boo stars.

1.4.6 STYLE

The reader may have noticed that, although only one author was mentioned on the cover of this thesis, this work is written in the 'we' form. There are a number of reasons for this. One of them is the fact that scientific research is always based on cooperation. Science is based on asking questions, and the best and most critical questions arise in discussions with others. Two of the chapters in this thesis have appeared (or will soon appear) in scientific journals as papers with three authors on them. The first author has her name on the cover of this thesis. The tradition at Leiden University, however, does not allow mentioning the other authors in the acknowledgements. Their contribution and enthusiasm, though, have been of great value. It is also therefore that this thesis is written in the 'we' form.

2

STARTING A STELLAR WIND

[1] The slow and dense winds by which Asymptotic Giant Branch (AGB) stars eject their envelopes are driven by radiation pressure on grains that form in the wind. Through these grains various physical processes become tightly coupled, resulting in an extremely nonlinear system involving large scale and molecular dynamics, chemical reactions, nucleation, growth and evaporation of grains, and radiation transport. The interaction between these physical processes can easily become very complicated. In order to correctly interpret observations or to make predictions about the behaviour of the envelope it is therefore essential to develop self-consistent numerical models. These should be based on the equations of motion for gases, i.e. hydrodynamical models, combined with radiative transfer calculations and chemical networks. In the context of dust driven winds from AGB stars, a number of these models has been developed; we will discuss them in the next chapter.

The purpose of this chapter is to provide an overview of all ingredients going into such modelling. The presentation of results is deferred to the next chapters. We give a detailed description of the techniques and methods underlying the hydrodynamics code that we have constructed and we provide references to alternative approaches. Also, we want to discuss the difficulties involved with the implementation of the various physical processes as source terms in the numerical hydrodynamics. We will not spend much time describing the detailed mathematical background and concepts of computational fluid dynamics; many good sources exist in the literature and we will refer to them whenever needed.

Producing a numerical hydrodynamics code for general fluid flow is straightforward. There are many papers and textbooks which provide an almost step-by-step manual to do so. Examples are Boris (1976) and Icke (1991) who together provide all the ingredients to get started with the FCT/LCD code, or the very complete textbook by Laney (1998), or the lecture notes by LeVeque (1998). In order to calculate the flow for a specific (astro)physical setup one will however always need to take into account physical effects as source terms. The incorporation of these is less trivial, first, because they will almost always introduce new interdependencies between the flow variables and, second, because all of them have their characteristic time scales, which may differ by orders of magnitude from the dynamical time scale.

Even the most sophisticated, complete and self-consistent hydrodynamics code is completely useless without carefully constructed boundary conditions. Since nature

[1]The contents of this chapter overlap largely with Simis et al. (2001a). Section 2.2.4 is published as a part of Simis et al. (2001b)

does not possess boundaries this is a non-trivial problem. The imposed behaviour of the boundary cells can have huge implications for the results of the calculations and therefore needs great attention. We discuss boundary conditions which are meant to influence the flow on the grid and also boundary conditions designed to influence the flow as little as possible.

Related to this is the problem of the initial conditions. Starting a numerical hydrodynamics calculation is always an unphysical event and may give rise to transient solutions which are mathematically correct but do not represent a realistic physical state. We discuss several possibilities to smoothly start the computation.

Although we focus in this paper on the construction of a hydrodynamics code to calculate the dust driven winds from AGB stars, the methods we use and the problems we discuss are very generally encountered when modelling (astro)physical fluid flow. We have tried to construct this chapter so that the reader interested in numerical hydrodynamics of any kind of flow, but not interested in the implementation of the physics specific to the problem of winds from AGB stars can easily skip these parts without missing any of the points we make.

2.1   NUMERICAL HYDRODYNAMICS

2.1.1   BASIC PRINCIPLES

Numerical hydrodynamics is, roughly spoken, based on two facts. Firstly, it is possible to translate a Partial Differential Equation (PDE) into a Finite Difference Scheme (FDS). Secondly, over the years people have invented methods that enable to compensate for the fact that these FDS are intrinsically discrete, which is necessary for numerical calculations, whereas gas flow is a continuous process. In this section we aim to make the reader familiar with the basics of numerical hydrodynamics. We present a step-by-step overview of the method we have used in our AGB wind numerical code. Also, we will mention alternative methods and provide references to useful literature.

FINITE DIFFERENCE THEORY

The basic equations for hydrodynamics are the conservation equations for mass, momentum and energy. We write them in advection form:

$$\frac{\partial w}{\partial t} + \frac{\partial (vw)}{\partial r} = S(r, t) \tag{2.1}$$

where $w = w(r, t)$ is the flow variable (i.e. the mass, momentum, or energy density), v is the transport velocity, and $S(r, t)$ is the source term. Note that here the coordinate r denotes a Cartesian coordinate and that we have limited ourselves to one dimensional flow. Other coordinate systems will be treated later.

The basic equations of hydrodynamics (Eq.(2.1)) form a non-linear system of first order hyperbolic equations. There are various ways to translate this kind of equations into a Finite Difference Scheme (FDS), i.e. to discretize them, which is needed to use them in a numerical calculation. A very complete overview of Finite Difference

Methods, as well as a thorough introduction to the principles of computational gas dynamics can be found in Laney (1998). In a more concise review, in which a wealth of other useful references can be found, LeVeque (1998) covers the most relevant matter as well.

In our AGB wind code we have used the following discretization scheme (Icke, 1991),

$$w_n^{l+1} = w_n^l - v\frac{\Delta t}{2\Delta r}(w_{n+1}^l - w_{n-1}^l) + S\Delta t \tag{2.2}$$

where the subscripts and superscripts represent the position index and the time index respectively. This FDS is an Euler scheme which uses *centered differencing*, and gives second order accuracy in space. Furthermore, it is an *explicit* scheme, i.e. variables at time step $l + 1$ do not depend on other variables at $l + 1$,

$$w_n^{l+1} = f(\{w^l\}). \tag{2.3}$$

Implicit schemes, on the other hand, allow w_n^{l+1} to depend on both values of w in nearby cells at time l and $l + 1$,

$$w_n^{l+1} = g(\{w^l\}, \{w^{l+1}\}). \tag{2.4}$$

In this case, a nonlinear algebraic system has to be solved at each grid point for each time step. Hence advancing one time step with an implicit scheme in general is more time consuming than in an explicit scheme. On the other hand: the time step to be taken in an explicit code is limited (see below) whereas in an implicit scheme it can be chosen freely. In our applications, we have used an explicit scheme. We have done so because our hydrodynamics code is suitable for two-fluid hydrodynamics, which brings about complicated and extremely non-linear sources terms so that an implicit method would be very inefficient.

STABILITY, CONSISTENCY AND CONVERGENCE

The time step in an implicit code can simply be taken to be equal to the desired time resolution. In an explicit code one has to take into account that there is a maximum communication speed u (the sum of the local fluid velocity and the sound velocity) which limits the time step as follows:

$$\epsilon = u\frac{\Delta t}{\Delta r} < 1 \tag{2.5}$$

This is the Courant-Friedrichs-Lewy (CFL) condition (Courant et al., 1928). It says that the physical domain of dependence must completely lie within the numerical domain of dependence. This means that no information (density fluctuations, pressure waves) is allowed to travel faster than the sound crossing time through a computational cell, Δr. Note that Δt should be equal for all r, so that the numerical time step in fact has to be the minimum of Eq.(2.5) over all coordinates. The presence of source terms, i.e. forces with their own characteristic time scale, may constrain the time step even further. The numerical time step must obey the CFL condition in order to have

stability. We will address this issue below and will see that respecting Eq.(2.5) alone is not always sufficient to achieve stability.

Eq.(2.5) only provides a necessary condition for stability, a proper analysis is required to determine an accurate stability condition in terms of Δt and Δr. A useful criterion is given by the linear stability analysis by Neumann (c.f. Colella & Puckett (1997)). A solution of the homogeneous equivalent of Eq.(2.1) is

$$w(r,t) = We^{\sigma t}e^{i\omega r} \tag{2.6}$$

Or, in discrete form (on a homogeneous mesh)

$$w_n^l = W(e^{\sigma \Delta t})^l e^{i\omega n \Delta r}. \tag{2.7}$$

Here $(e^{\sigma \Delta t})$ is the amplification factor. This factor should be smaller than or equal to unity in order to ensure that the scheme is stable. In that case one can be sure that enhancing time resolution does not lead to larger errors. Now define

$$\theta = e^{\sigma \Delta t} \tag{2.8}$$
$$k = \omega \Delta r. \tag{2.9}$$

Substitution of Eq.(2.7) in the homogeneous Eq.(2.2) then leads to

$$\theta = 1 + iv\frac{\Delta t}{\Delta r}\sin k. \tag{2.10}$$

Hence

$$\theta\theta^* = 1 + (v\frac{\Delta t}{\Delta r})^2\sin^2 k, \tag{2.11}$$

which means that the amplification factor exceeds unity for every combination of Δt and Δr. Thus the centered differencing Euler scheme is unstable, even for combinations of Δt and Δr that satisfy the CFL condition.

The *local truncation error* (LTE) of a numerical method can be found by inserting the exact solution of the problem into the FDS at a single point in space time. The LTE is a measure of how well the FDS locally models the original differential equations. A numerical method is called *consistent* if the LTE goes to zero if Δr and Δt become infinitely small. If a method is both stable and consistent it is called *convergent*.

GRID

Numerical hydrodynamics calculations are performed on a $N + 1$ dimensional grid, where N is the number of spatial dimensions of the problem. For now, we limit our discussion to the case of one spatial dimension and a Cartesian geometry. The simplest grid in this case is a grid with equidistant steps in both space and time. In practice, the time resolution of the grid will not be fixed a priori but will be determined just before the time step is taken. In explicit calculations subsequent numerical time steps will only be of equal size if the flow is stationary.

The grid spacing in the spatial dimension also does not need to be uniform over the range of the grid. In general the best choice is to choose the finest grid spacing in the region where one can expect the steepest gradients in the flow variables. In regions where the flow is expected to be quiescent the cells should be chosen as big as possible, since taking unnecessarily small cells is memory consuming. It is recommended to make the grid smooth: the sizes of adjacent cells should not differ more than a few percent, otherwise artificial source terms will be introduced, for which one will need to correct.

If one expects steep gradients to occur at various locations and times, e.g. in the case of moving shocks, an adaptive or moving grid may be useful. This can simply be achieved by using a Lagrangian formulation of the fluid equations. In that case the grid points move along with the fluid. Boris (1976), in his step-by-step treatment of the Flux Corrected Transport method (which will be introduced below) provides ready-to-use expressions in both Eulerian and Lagrangian coordinates. Alternatively, the grid points can be moved to concentrate around regions of rapid variation of the flow variables. A more sophisticated approach is *Adaptive Mesh Refinement* (AMR), in which grid cells are split into smaller cells whenever a higher resolution is desired to resolve the structure of the local flow. A good brief introduction to AMR can be found in the lecture notes by LeVeque (1998) and Dorfi (1998) and references therein. The advantage of adaptive grids is that they provide the desired resolution everywhere, depending on the evolution of the flow. The disadvantage is that recalculating the grid and re-mapping the flow on the grid takes computer time and there is a risk of losing accuracy.

For our applications we use a fixed grid with a high resolution near the stellar surface, where the driving of the AGB winds and all the interesting physical and chemical processes take place, and a much wider grid spacing further out. The cells in our grid are distributed according to

$$\frac{r[n] - r[n-1]}{r[1] - r[0]} = q^{n-1/n_{\max}-1} \tag{2.12}$$

where $n_{\max}$ is the number of cells in the grid, and q is the size ratio between the innermost and the outermost cell. Both can be defined by the user to create the desired grid.

2.1.2   METHODS FOR NUMERICAL HYDRODYNAMICS

Once the differential equation is translated into a FDS it can be used to calculate the evolution of the flow variables. From Eq.(2.2) it appears to be straightforward to calculate the state $\{w^{n+1}\}$ from $\{w^n\}$. This however is not the case, because the FDS does not cover more than the second order of the Fourier expansion of Eq.(2.1). The second term in the r.h.s. of Eq.(2.2) can be interpreted as the net advective flux through the boundaries of cell n with the adjacent cells. Obviously, the fluxes are very poorly approximated because the higher order terms are omitted. The various numerical methods distinguish themselves by the way in which the fluxes are calculated.

When interpreting the advective terms in the numerical scheme as fluxes one speaks of a Finite Volume Method rather than of a Finite Difference Method. The difference between both is that the flow variable w_n^l is not considered as an approximation to the single value $w(r_n, t_l)$ but as an approximation of the average w over the interval

$\Delta r = (r_{n-1/2}, r_{n+1/2})$. The main advantage of this is that this way the numerical method is guaranteed to be conservative ("what flows out of a certain cell must flow into one of the adjacent cells"). We will later show how our FDS can be represented as a finite volume method.

One can distinguish two different categories of methods for solving the Euler equations: flux approaches and wave approaches (or Riemann solvers). An extensive introduction to wave methods can be found in the book by Laney (1998). An example of a wave method is the Roe solver (Roe, 1991). Roe's method is based on the use of characteristics. These are the trajectories of the flow discontinuities (shock, contact discontinuity and rarefaction wave) in space-time.

A completely different method, not based on solving the Euler equations at all, is the Bhatnagar–Gross–Krook (BGK) (Bhatnagar et al., 1954; Slyz & Prendergast, 1999) method. A very clear outline of this method can be found in lecture notes by Xu (1998). The BGK method makes use of kinetic gas theory, so that, in contrast with Euler methods, it is also applicable in non-equilibrium states, like strong shocks. In the remaining part of this section we will discuss in detail the flux based method we have used in our AGB wind code.

FCT/LCD

In this section we describe the FCT/LCD method. FCT is short for Flux Corrected Transport and was developed in the seventies by Boris & Book (Boris & Book, 1973; Book et al., 1975; Boris & Book, 1976; Boris, 1976). Their papers provide a very clear description of the method and can be easily used as a manual for the development of a FCT code. In order to suppress unwanted high-frequency behaviour near discontinuities in FCT calculations, Icke (1991) added the concept of Local Curvature Diminishing (LCD). We present below this FCT/LCD scheme, with a small modification of the LCD term. Initially, we will present the equations in finite difference form and in one dimension and Cartesian coordinates. Afterwards, we present the method in finite volume form and we will give expressions for the equations in spherical and cylindrical symmetry. Also we will address the idea of a two step, predictor-corrector method.

It was shown by e.g. Icke (1991) that centered differencing (c.f. Eq.(2.2)) without any modification is unstable since the amplitude of each partial wave solution is multiplied by a complex number with absolute magnitude larger than unity. This means that advection of a pure sine wave will produce a sine wave which shows a gradual increase of amplitude. The obvious way of opposing this is to introduce diffusion. This is done by inserting a term for numerical or artificial viscosity (von Neumann & Richtmyer, 1950). The diffused homogeneous differential scheme is

$$w_n^D = w_n^A + \nu_n(w_{n-1}^l - 2w_n^l + w_{n+1}^l)$$
$$= w_n^l - \epsilon_n(w_{n+1}^l - w_{n-1}^l) + \nu_n(w_{n-1}^l - 2w_n^l + w_{n+1}^l) \tag{2.13}$$

where w_n^A is the advected flow variable, defined by the l.h.s. of Eq.(2.2). For stability we need $\nu < \frac{1}{2}$ and $\nu > \frac{1}{2}\epsilon^2$, hence $\epsilon < 1$. This implies the CFL condition Eq.(2.5) becomes a sufficient condition for stability when numerical diffusion is added to the

Euler scheme. Furthermore, phase errors can be suppressed up to fourth order by choosing

$$\nu = \frac{1}{6} + \frac{\epsilon^2}{3} \tag{2.14}$$

Though numerical viscosity is helpful to acquire stability it also has disadvantages. It turns out that for advection speeds close to zero, a considerable artificial diffusion speed is produced by second–order errors. The diffusive character of numerical viscosity makes it a powerful tool to suppress instability but at the same time causes a general smoothing of the flow profile. This is a most unwanted effect since a major part of the interesting physical phenomena (narrow dust formation region, shocks) show sharp structures.

To solve the problem of the diffusive systematic errors it seems reasonable to apply diffusion only where it is needed, i.e. near steep gradients, where the risk of unstable behaviour is large. This is what the Flux Corrected Transport (FCT) method does. FCT consists of two major stages. In the first step the advection and diffusion (c.f. Eq.(2.13)) are carried out, in the second stage an anti-diffusive flux is applied wherever diffusion was not essential for the stability of the solution. The anti-diffusion equation can be derived as follows (Boris & Book, 1973). As mentioned in the previous section, phase errors can be suppressed up to fourth order by choosing the right value for the numerical diffusion coefficient, see Eq.(2.14). Unwanted diffusion in case of low advection speed is a more serious problem. When the advection speed is zero, a pure diffusion equation is produced from Eq.(2.2)

$$w_n^D = w_n^l + \frac{1}{6}(w_{n-1}^l - 2w_n^l + w_{n+1}^l) \tag{2.15}$$

The exact solution however should be $w_n^D = w_n^l$. When we assume the intended solution after the anti-diffusion step (w_n^{AD}) to be equal to w_n^{l+1} we can write

$$w_n^D = w_n^{AD} + \frac{1}{6}(w_{n-1}^{AD} - 2w_n^{AD} + w_{n+1}^{AD}) \tag{2.16}$$

Solving this implicit equation would lead to the corrected solution. However, for the applications we have in mind an explicit method is preferred. Therefore we derive from Eq.(2.16) the following explicit anti-diffusion equation

$$w_n^{AD} = w_n^D - \frac{1}{6}(w_{n-1}^D - 2w_n^D + w_{n+1}^D) \tag{2.17}$$

In the general case of nonzero advection speed the scheme becomes

$$w_n^{AD} = w_n^l - \epsilon_n(w_{n+1}^l - w_{n-1}^l) + \nu_n(w_{n+1}^l - 2w_n^l + w_{n-1}^l) - \mu_n(w_{n+1}^D - 2w_n^D + w_{n-1}^D) \tag{2.18}$$

With the choice

$$\mu = \frac{1}{6} - \frac{\epsilon^2}{6} \tag{2.19}$$

relative phase errors in a locally uniform grid are reduced to fourth order (Boris & Book, 1976; Icke, 1991).

The modifications of the quantity w_n^l should be interpreted as advective, diffusive, and anti-diffusive fluxes through the boundaries of cell n:

$$
\begin{aligned}
w_n^{AD} = w_n^l &- \epsilon_{n+1/2}(w_{n+1}^l + w_n^l) + \epsilon_{n-1/2}(w_n^l + w_{n-1}^l) + \\
&\nu_{n+1/2}(w_{n+1}^l - w_n^l) - \nu_{n-1/2}(w_n^l - w_{n-1}^l) - \\
&\mu_{n+1/2}(w_{n+1}^D - w_n^D) + \mu_{n-1/2}(w_n^D - w_{n-1}^D)
\end{aligned}
\tag{2.20}
$$

Or,

$$
w_n^{AD} = w_n^l - F_{n+1/2}^A + F_{n-1/2}^A + F_{n+1/2}^D - F_{n-1/2}^D - F_{n+1/2}^{AD} + F_{n-1/2}^{AD}
\tag{2.21}
$$

The fact that we now also need to know the values of our flow variables at the cell boundaries rather than the cell centers poses no problem. On the contrary: we will later discuss the implementation of the current FDS in a two-step predictor-corrector method, in which we actually want the fluxes and velocities to be defined at the cell boundaries.

A drawback of merely applying anti-diffusion is the fact that it might introduce artificial extrema or accentuate existing maxima and minima. This violation of monotonicity (Wesseling, 1992) will cause 'wiggles' near discontinuities and is of course unwanted. To correct for non–monotonic behaviour, FCT algorithms contain a *flux limiter*. The idea is to limit the anti-diffusive fluxes so that nowhere on the grid anti-diffusion pushes the density value beyond the density value in the adjacent cells. A further constraint on the FCT scheme is that it should not violate conservation, i.e. a flux that contributes positively to the density in a certain cell should contribute negatively to the density in another cell. In other words, the FCT scheme should not create matter, momentum or energy at cell boundaries.

Flux limiters make the FCT scheme non–linear since linear monotone schemes are at most first order accurate (Harten et al., 1976). Boris & Book (1973) constructed a positive, conservative, flux limiting FCT scheme in which the anti-diffusive fluxes $F_{n+1/2}^{AD}$ in Eq.(2.21) are replaced by the FCT fluxes

$$
F_{n+1/2}^{FCT} = \text{Sgn}(\Delta_{n+1/2})
$$
$$
\text{MAX}\{0, \text{MIN}[\text{Sgn}(\Delta_{n+1/2})\Delta_{n-1/2}, \text{Sgn}(\Delta_{n+1/2})\Delta_{n+3/2}, \mu_{n+1/2}|\Delta_{n+1/2}|\}
\tag{2.22}
$$

Where

$$
\Delta_{n+1/2} = w_{n+1}^D - w_n^D
\tag{2.23}
$$

It is easy to see that this FCT flux does what it should do. First, near a maximum or minimum it becomes zero; $F_{n+1/2}^{FCT} = 0$ if $\Delta_{n+1/2}$ and $\Delta_{n-1/2}$ or $\Delta_{n+3/2}$ (or both) have opposite sign. Hence, near extrema diffusion is not opposed by anti-diffusion. If neither grid point n nor grid point $n+1$ shows an extremum for w and if the slope of the w profile is nonzero there will be anti-diffusion. The anti-diffusive flux will be directed opposite to the diffusive flux F^D. Its size is given by the original anti-diffusive flux (Eq.(2.20)) unless this flux pushes w_{n+1} beyond w_{n+2} or w_n beyond w_{n-1}. In that case the anti-diffusive flux is limited to a flux that leads to $w_{n+1} = w_{n+2}$ or $w_n = w_{n-1}$ respectively. This concept will maintain monotonicity. Since $F_{n+1/2}^{FCT}$

appears in Eq.(2.20) and a similar expression for grid point $n+1$ with opposite token the scheme is obviously conservative.

Icke (1991) points out that the FCT scheme, when applied to (astrophysical) situations involving large gradients, may be rather noisy. He presents a method to suppress the very–high–frequency Fourier (VHF) components by selectively reducing the effectiveness of anti-diffusion, using Local Curvature Diminishing (LCD). In this method, the second derivative of the flow variable is used as an indicator for the amount of VHF power. The anti-diffusive flux is modified by a substitution of the parameter μ as follows

$$
\tilde{\mu}_{n+1/2} = \mu_{n+1/2} - \eta |H|_{n+1/2}
\tag{2.24}
$$

Here, η is a positive parameter of which the value will be determined hereafter and H is a four point second derivative divided by the local average value of the flow variable:

$$
H_{n+1/2} = \frac{w_{n-1} - w_n - w_{n+1} + w_{n+2}}{w_n + w_{n+1}}
\tag{2.25}
$$

A useful choice for η is found by demanding $\tilde{\mu}_{n+1/2} = 0$ for the shortest wavelength, $\lambda_{\min}$. On a computational grid of grid spacing Δr we have $\lambda_{\min} = 4\Delta r$. Hence we have a maximum value for the phase number k (see Eq.(2.9)) given by

$$
k_{\max} = \frac{2\pi}{\lambda_{\min}}\Delta r = \frac{\pi}{2}
\tag{2.26}
$$

Substituting Eq.(2.7) in Eq.(2.25) one finds that, for all n,

$$
|H|_{n+1/2} = 2 - 2\cos k
\tag{2.27}
$$

(Icke, 1991). Hence, indeed $|H|_{n+1/2}$ has a maximum value of 2 for $k = k_{\max}$. So, demanding $\tilde{\mu}_{n+1/2} = 0$ for $k = k_{\max}$ one finds that for all n maximal suppression of the VHF components is reached for

$$
\eta = \frac{\mu}{2}
\tag{2.28}
$$

INCORPORATION OF SOURCE TERMS

Above, we have presented the FCT/LCD method for the homogeneous PDE. But in our AGB wind code, none of the hydrodynamics equations is homogeneous. On the contrary, we will be dealing with stiff source terms, for which a very accurate implementation is crucial. Straightforward incorporation of the sources in the FCT/LCD scheme will not give reliable results however. This is because the presence of a source term does not have any influence on the diffusive fluxes, but it will influence the anti-diffusive fluxes, which are calculated from the diffused flow variable, which is (replacing the homogeneous form Eq.(2.13)) given by

$$
w_n^D = w_n^l - \epsilon_n(w_{n+1}^l - w_{n-1}^l) + \nu_n(w_{n-1}^l - 2w_n^l + w_{n+1}^l) + S_n\Delta t
\tag{2.29}
$$

Van Leer (1984) and Eulderink (1993), based on an earlier method by Liu (1979), proposed a more accurate incorporation of the source terms. A description of the

implementation of this method in the FCT/LCD code is given by Icke (1991). The idea is to remove the unwanted anti-diffusion of the source terms by partially incorporating them in the advective fluxes. With

$$F^{A}_{n+1/2} = \epsilon_{n+1/2}(w^l_{n+1} + w^l_n) + \mu_{n+1/2}(r_{n+1} - r_n)(S_{n+1} - S_n) \qquad (2.30)$$

it turns out that the errors in the source term are reduced to fourth order.

FINITE VOLUME METHOD

A more general form for the continuity equation (2.1) is

$$\frac{\partial w}{\partial t} + \frac{1}{r^{\alpha-1}}\frac{\partial}{\partial r}\left(r^{\alpha-1}wv\right) = \frac{C_1}{r^{\alpha-1}}\frac{\partial}{\partial r}\left(r^{\alpha-1}D_1\right) + C_2\frac{\partial D_2}{\partial r} + D_3. \qquad (2.31)$$

In this expression, D_1 is a vector quantity in the divergence source term, D_2 is a scalar quantity in the gradient source term, D_3 is a source term in non–derivative form, and C_1 and C_2 are constants. The shape of the grid is determined by α:

$\alpha = 1$ Cartesian coordinates and symmetry
$\alpha = 2$ Cylindrical   ,,   ,,   ,,
$\alpha = 3$ Spherical   ,,   ,,   ,,

Following Boris (1976) we introduce the cell volumes $\{\Lambda_n\}$ $(n = 1, \cdots, k)$ and the cell interface areas $\{A_{n+1/2}\}$ $(n = 1, \cdots, k)$:

$$
\begin{array}{lll}
\Lambda_n = [r_{n+1/2} - r_{n-1/2}] & A_{n+1/2} = 1 & (\alpha = 1) \\
\Lambda_n = \pi [r^2_{n+1/2} - r^2_{n-1/2}] & A_{n+1/2} = \pi r_{n+1/2} & (\alpha = 2) \\
\Lambda_n = \frac{4\pi}{3}[r^3_{n+1/2} - r^3_{n-1/2}] & A_{n+1/2} = \frac{4\pi}{3}r^2_{n+1/2} & (\alpha = 3)
\end{array}
$$

The FDS, in that case, only taking into account the advective fluxes (c.f. Eq.(2.2)), reads

$$\frac{w^A_n - w_n}{\Delta t} + \frac{1}{r^{\alpha-1}_n}\frac{(r^{\alpha-1}_{n+1/2}w_{n+1/2}v_{n+1/2} - r^{\alpha-1}_{n-1/2}w_{n-1/2}v_{n-1/2})}{r_{n+1/2} - r_{n-1/2}} =$$

$$\frac{C_1}{r^{\alpha-1}_n}\frac{r^{\alpha-1}_{n+1/2}D_{1,n+1/2} - r^{\alpha-1}_{n-1/2}D_{1,n-1/2}}{r_{n+1/2} - r_{n-1/2}} + C_2\frac{D_{2,n+1/2} - D_{2,n-1/2}}{r_{n+1/2} - r_{n-1/2}} + D_{3,n} \qquad (2.32)$$

For a Cartesian grid

$$\Lambda_n = A_n(r_{n-1/2} + r_{n+1/2}). \qquad (2.33)$$

When assuming the same for $\alpha = 2, 3$ we automatically find the equation in finite volume form

$$w^A_n\Lambda_n = w_n\Lambda_n - A_{n+1/2}w_{n+1/2}v_{n+1/2}\Delta t + A_{n-1/2}w_{n-1/2}v_{n-1/2}\Delta t +$$
$$C_1(A_{n+1/2}D_{1,n+1/2} - A_{n-1/2}D_{1,n-1/2})\Delta t +$$
$$C_2(D_{2,n+1/2} - D_{2,n-1/2})\Delta t + D_{3,n}\Lambda_n\Delta t \qquad (2.34)$$

With this format, conservation is indeed guaranteed: the flux through cell wall $n+1/2$ takes away from cell n exactly the amount of mass, momentum or energy that it adds to cell $n+1$, see Fig. 2.1. Addition to this scheme of the diffusive and FCT/LCD fluxes in finite volume form is straightforward, see also Boris (1976).
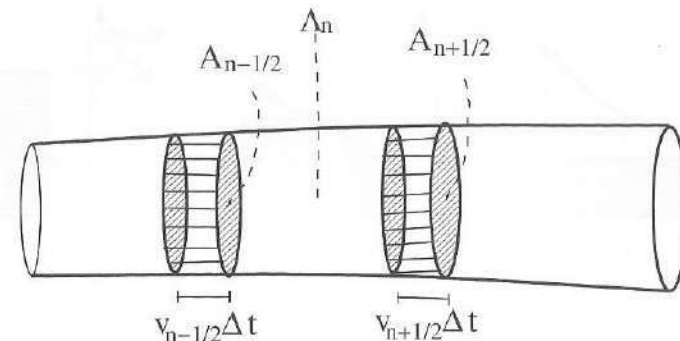
FIGURE 2.1: Finite Volume Method: $v_{n-1/2}A_{n-1/2}\Delta t$ is the volume, located in cell $n-1$, the contents of which will flow into cell n during Δt. Similarly, the contents of the volume $v_{n+1/2}A_{n+1/2}\Delta t$ will flow from cell n into cell $n+1$ during this time step.

TWO-STEP PREDICTOR-CORRECTOR METHOD

The flux through cell wall $n-1/2$ is proportional to the fluid velocity at this location. More precisely, the total influx through cell boundary $n-1/2$ during time step $\Delta t = t^{l+1} - t^l$ is proportional to $v_{n-1/2}A_{n-1/2}\Delta t$, i.e. to the volume, located in cell $n-1$, the contents of which are transferred to cell n during Δt. This is illustrated in Fig. 2.1. Since the fluid velocity itself is also a time dependent variable this volume is better approximated by $v^{l+1/2}_{n-1/2}A_{n-1/2}\Delta t$ than by $v^{l-1}_{n-1/2}A_{n-1/2}\Delta t$ or $v^{l+1}_{n-1/2}A_{n-1/2}\Delta t$, this is illustrated in Fig. 2.2. The corresponding FDS will be of the form

$$w^{l+1}_n = w^l_n + F(v^{l+1/2}_{n-1/2}) - F(v^{l+1/2}_{n+1/2}) \qquad (2.35)$$

In order to be able to update w according to Eq.(2.35), it is necessary to first calculate the velocities after half of the time step. This is done by first performing a *predictor* step, over $\Delta t/2$. From that we than can calculate the fluxes at time $l+1/2$ at the cell walls. Subsequently, these are used in Eq.(2.35), which is called the *corrector* step. We use the two-step predictor corrector method as in Boris (1976), though various similar methods exist (e.g. Richtmyer, MacCormack or Lax Wendroff (Laney, 1998)).

2.2 IMPLEMENTATION OF PHYSICAL PROCESSES IN NUMERICAL HYDRODYNAMICS

In the previous section, we have provided the tools to construct a numerical hydrodynamics code. Although we have done so having in mind the development of a hydrodynamics code for the calculation of dust driven winds from AGB stars, the theory and techniques discussed are very general. In this section, we will discuss the physical phenomena that are relevant to AGB winds and their implementation in the hydrodynamics code.

Hoyle & Wickramasinghe (1962) suggested that radiation pressure on grains could be a driving mechanism for the observed winds from late type stars. In the following years observational evidence for the presence of dust grains was given by e.g. Ney &
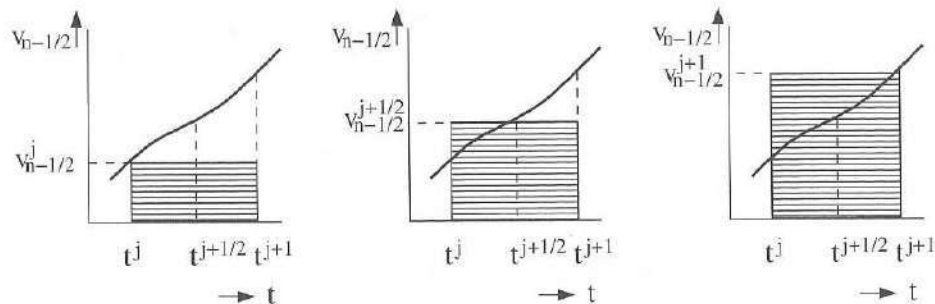
FIGURE 2.2: The volume of which the contents flow from cell $n-1$ into cell n during a time Δt is better approximated by $v_{n-1/2}^{l+1/2} A_{n-1/2} \Delta t$ (middle) than by $v_{n-1/2}^{l-1} A_{n-1/2} \Delta t$ (left) or $v_{n-1/2}^{l+1} A_{n-1/2} \Delta t$ (right).

Allen (1969) and Hackwell (1972). Salpeter (1974b; 1974a) provided a first, but very complete, overview of the consequences of the presence of grains in stellar outflows.

Today, the idea that winds from late type stars can be dust driven is generally accepted. Small solid particles form in the extended atmospheres of dying solar type stars (1-8 $M_\odot$). These grains are efficient absorbers of stellar radiation in a broad wavelength regime. They experience a net outward radiation pressure and move through the gas with nonzero *drift* velocity. In the absence of grain drift, gas and dust particles will collide frequently due to the thermal motion of the gas, but no net momentum transfer from one state to the other will take place since the collisions are random. When the grains are accelerated with respect to the gas due to radiation pressure, the rate of collisions between particles of both 'fluids' increases. Moreover, now there will be momentum transfer from grains to gas because the velocity distribution of the grains is no longer random.

Clearly, the mechanism of dust driven winds depends on the complex interplay of various processes, such as grain formation, growth and evaporation, radiation pressure on grains, fluid flow etc. Numerical hydrodynamics provides an excellent tool to explore parameter space of dust driven winds and to find out more about the way the relevant physical processes influence each other. Preferably, a numerical simulation should be self-consistent. In general this means that only the initial state is provided and everything else is calculated within the code. Hence, a fully self consistent code includes gas chemistry, grain formation and growth, gas-grain interactions, time dependent hydrodynamics in which all states are separate, but coupled, fluids, radiative transfer etc.

The first (stationary) numerical model calculation, including gravitation, radiation pressure on dust, momentum transfer from dust to gas and grain-growth and sputtering, was presented by Kwok (1975). Since then, various groups have modelled several aspects of the outflows of late type stars. Stationary models, focused on a realistic implementation of grain nucleation and growth, have been developed in the 'Berlin group', initially for carbon rich objects (Gail et al., 1984; Gail & Sedlmayr, 1987) and recently also for the more complicated case of silicates in circumstellar shells of M stars (Gail & Sedlmayr, 1999). Two-fluid models, in which not necessarily all the momen-

tum absorbed by the grains is transferred to the gas, have been studied by few people. Berruyer & Frisch (1983), Berruyer (1991) and MacGregor & Stencel (1992), pointed out that, for stationary and isothermal atmospheres, the assumption of complete momentum coupling breaks down at large distances above the photosphere and for small grains. Self-consistent, but again stationary, two-fluid models, considering the grain size-distribution, dust formation and the radiation field were developed by Krüger and co-workers (Krüger et al., 1994; Krüger & Sedlmayr, 1997). Time-dependent hydrodynamics has been applied to study pulsations (Bowen, 1988; Fleischer et al., 1992). The coupled system of radiation hydrodynamics and time-dependent dust formation was solved by Höfner et al. (1995).

Two-fluid time-dependent wind models were computed in the very early work of Woodrow & Auman (1982) and by Mastrodemos et al. (1996). Both models are not self-consistent however and Mastrodemos et al. adopt a simplified description of grain formation and give only a heuristic description of the inner 5-10 R_*. It is the aim of this work to combine the aspects mentioned above and construct a two-fluid, time-dependent hydrodynamics code that self-consistently calculates the outflow under the assumption of spherical symmetry, for a given set of initial parameters ($M_*, L_*, T_*, \epsilon_{C/O}$). The main physical and chemical processes in AGB winds are the gas chemistry, grain nucleation, growth and evaporation, radiation pressure on dust and momentum transfer from grains to gas through collisions. These processes will be discussed in this section. We will extensively address the way in which the chemistry and the physics are modelled and the implementation of the models in numerical hydrodynamics. The implementation of physical and chemical processes as source terms in a numerical hydrodynamics code can be straightforward, e.g. in the case of gravity, or totally non-trivial, as is the case for the momentum transfer (collisional drag force) from grains on the gas. In general we can say that taking into account a certain physical or chemical process as a source term in the hydrodynamics equations becomes more difficult if the characteristic time scale associated with it becomes small compared to the dynamical time scale. Except for the gas chemistry, radiation transport, and stellar pulsation, the physical and chemical processes discussed below will appear as source terms in the hydrodynamics equations. These equations, which are all of the form of Eq.(2.1), are the continuity equations for the gas and the dust and the momentum equations for both. An energy equation for the gas could be added as well. Because of the proximity of the luminous central star, we use an external method to calculate the temperature stratification, and hence we can omit the energy equation. The source term in the continuity equations for the gas and dust, $s_{\mathrm{cond,g,d}}$, covers the nucleation, growth and evaporation of grains. In these processes matter is transferred from one state to another. Since the total mass is conserved we have

$$\frac{\partial \rho_{\mathrm{g,d}}}{\partial t} + \frac{1}{r^2}\frac{\partial}{\partial r}(r^2 \rho_{\mathrm{g,d}} v_{\mathrm{g,d}}) = s_{\mathrm{cond,g,d}} \qquad s_{\mathrm{cond,g}} = -s_{\mathrm{cond,d}} \qquad (2.36)$$

The source terms of the momentum equation are the forces relevant for the wind system. These are gravity, the pressure gradient, the radiative force (radiation pressure), the viscous drag force and the momentum transfer due to the formation or destruction of

grains. Note that dust grains have no appreciable thermal motion so that dust pressure is not considered. Radiation pressure on the gas is negligible. The momentum equations are

$$\frac{\partial}{\partial t}(\rho_g v_g) + \frac{1}{r^2}\frac{\partial}{\partial r}(r^2 \rho_g v_g^2) = -\frac{\partial P}{\partial r} + f_{drag,g} - f_{grav,g} + v_g s_{cond,g} \qquad (2.37)$$

$$\frac{\partial}{\partial t}(\rho_d v_d) + \frac{1}{r^2}\frac{\partial}{\partial r}(r^2 \rho_d v_d^2) = f_{rad} + f_{drag,d} - f_{grav,d} - v_g s_{cond,g} \qquad (2.38)$$

These equations form a system of two fluid hydrodynamics, i.e. gas and dust are each described by their own set of hydrodynamics equations. The equations couple via the source terms. The momentum equations couple via the viscous drag force of radiatively accelerated dust grains on the gas. Since no momentum is lost, we have

$$f_{drag,g} = -f_{drag,d} \qquad (2.39)$$

The drag force is proportional to the rate of gas–grain collisions and the momentum exchange per collision and is therefore of the form

$$f_{drag} = \Sigma_d n_g n_d m_g |v_D| v_D \qquad (2.40)$$

where Σ_d is the collisional cross section of a dust grain and v_D is the drift velocity of the grains with respect to the gas. In Section 2.2.4 we extensively discuss this force and the way in which it can be implemented in numerical hydrodynamics.

The radiative force (radiation pressure) on grains is of the form (cf. Eq.(2.77))

$$f_{rad} = \frac{L_* \kappa_d \rho_d}{4\pi r^2 c} \qquad (2.41)$$

where κ_d is the mass extinction coefficient of the dust. In Section 2.2.3 we discuss the implementation of the radiative force. The most simple force is gravity

$$f_{grav,d,g} = \frac{GM_* \rho_{d,g}}{r^2} \qquad (2.42)$$

Since the implementation of the gravitational force is straightforward, we do not discuss it. The radiative force is large compared to gravity, in the case of dust driven AGB winds. One should, however, not use this as an argument to neglect gravity. Our computations show that, without gravity, however small, it will be unrealistically easy to drive the stellar wind.
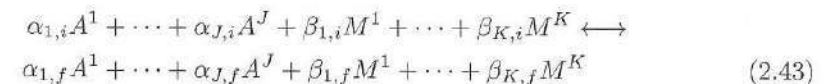
2.2.1 GAS PHASE CHEMISTRY

The interplay between dynamics and chemistry in the winds of late type stars is extremely subtle. This demands that the implementation of both is very accurate. In order to model the nucleation and growth of solids consistently, accurate information about the availability of the constituents is needed. Another reason to keep track of the molecular composition of the gas is its relevance for diagnostics, see Sedlmayr & Winters (1997).

Amongst late type stars, two types of chemically very different objects can be distinguished. In M-stars, oxygen is more abundant than carbon, and in C-stars the ratio is opposite. The distinct between both classes is very strict because the CO molecule is the first molecule to emerge in the flow, due to its high bond energy (~ 11.1 eV). In the absence of dissociating UV photons, the least abundant of C and O will be blocked out, leaving the other for the formation of complex molecules and grains. In this work, we assume the C/O ratio to be larger than unity. The sole motivation for this choice is the fact that the nucleation and growth of hydrocarbon–based grains is well studied an can be calculated relatively easily, which is an advantage when implemented in a time–dependent hydrodynamics code. Apart from CO, our equilibrium gas chemistry involves H, H_2, C, C_2, C_2H and C_2H_2.

A network of competing chemical reactions determines the formation and dissociation of molecules. Rate coefficients of these reactions depend on the abundances of the participating species and on the temperature. The abundances of each molecule can be found by simultaneously solving all rate equations. This, however, is computationally very expensive, since it implies solving a set of stiff nonlinear differential equations. An alternative method, more suitable for implementation in time dependent hydrodynamics is chemical equilibrium. Under the assumption of chemical equilibrium each reaction is balanced by its reverse. Now a much simpler a system of coupled equations (for the partial pressures of each element) has to be solved. The resulting concentrations are no longer time dependent. This is a problem if the characteristic time scale of the gas chemistry is larger than the dynamical time scale. The actual implementation and solution of the equilibrium gas chemistry are presented below.

In the present work we use dissociation equilibrium chemistry (e.g. Gail et al. (1984)) in a reduced form (Dominik, 1992). In equilibrium chemistry every reaction is balanced by its reverse. Assuming chemical equilibrium in the current work seems justified since large non–equilibrium effects due to UV radiation are not expected. Firstly, because interstellar UV photons will be absorbed by the dust and hence cannot penetrate into the dust formation regions[2]. Secondly, because late type stars do not have active chromospheres (Dominik, 1992). Consider an equilibrium chemistry consisting of J elements $A^j, j = 1, \ldots, J$, out of which K molecules ($M^k = A^1_{l_{1,k}} A^2_{l_{2,k}} \ldots A^J_{l_{J,k}}$) can be formed via chemical reactions of the form

$$\alpha_{1,i}A^1 + \cdots + \alpha_{J,i}A^J + \beta_{1,i}M^1 + \cdots + \beta_{K,i}M^K \longleftrightarrow$$
$$\alpha_{1,f}A^1 + \cdots + \alpha_{J,f}A^J + \beta_{1,f}M^1 + \cdots + \beta_{K,f}M^K \qquad (2.43)$$

The partial pressures of the molecules and the atoms are related by the dissociation constants, κ_{M^k}, which depend on the temperature only:

$$\kappa_{M^k} = P_{M^k} / \prod_{j=1}^{N} (P_{A^j})^{l_{j,k}} \qquad (2.44)$$

---

[2]Interstellar UV radiation is important in the outer envelope regions (Glassgold, 1996) but we ignore this because we are mostly interested in the inner regions of the wind, where the composition of the gas, via the formation of grains, can influence the mass loss rate. When calculating the gas abundances for diagnostic reasons it should be taken into account, though.

Here $l_{j,k}$ is the multiplicity of the atom species A^j in the molecule M^k. For each element participating in the chemistry, the total number of atoms is given by

$$n_{<A^j>} = \epsilon_j n_{<H>} = n_{A^j} + l_{j,1} n_{M^1} + \cdots + l_{j,K} n_{M^K}, \qquad j = 1, \ldots, J \qquad (2.45)$$

where ϵ_j denotes the abundance of the element A^j relative to hydrogen. Multiplication of Eqs.(2.45) with $k_B T$ then gives a set of J coupled equations for the partial pressures P_{A^j}. With known dissociation constants κ_{M^k}, temperature T, hydrogen density $n_{<H>}$ and abundances ϵ_j the system can be solved and all densities $n_{<A^j>}$ and n_{M^K} can be calculated. When solving the dissociation equilibrium one often uses the huge differences in abundances of the elements to decouple Eqs.(2.45). For example in the dissociation equilibrium of hydrogen, only H and H_2 are taken into account. This will violate mass conservation. In stationary calculations this is not a problem as long as the error is small. When dealing with time–dependent calculations, small errors will grow in time and mass conservation will be heavily violated. Hence, in the present time dependent calculation we solve the complete system iteratively. This limits the number of molecules that can be taken into account.

Due to the fact that the chemical composition of the gas is calculated assuming equilibrium it is not necessary to consider each of the atom and molecule number densities as a separate flow variable. To keep track of the abundances, it is sufficient to solve the continuity equation for each element A^j. The source term in this equation should account for the net consumption of this element as a result of the formation, growth and evaporation R_f of grains (see next section). The chemical equilibrium is calculated at the end of every time step, i.e. when the consumption or restitution of gas particles by the grains has been accounted for, and the temperature stratification has been calculated. The largest molecule in our equilibrium chemistry model is acetylene (C_2H_2). Hence, this molecule will be the largest to take part in the nucleation and growth of grains, which is described in the next section. This is not entirely realistic: there are indications that polycyclic aromatic hydrocarbons (PAHs) form in the carbon rich winds of late type stars, see e.g. (Cherchneff et al., 1992). Acetylene is the basic building block for these large molecules. They, may in turn form the basis for the formation of grains (Cherchneff & Cau, 1999). When we calculate the nucleation and growth of dust grains, we ignore the intermediate phase of the large aromatic molecules. Instead, we assume that small carbonaceous molecules are the nucleating species.

2.2.2 Nucleation, Growth and Evaporation of Grains

The formation and growth of solid particles from the supersaturated gas phase can be described as a diffusion process in cluster size space. Two main regimes can be distinguished: first the formation of condensation kernels and second the further development of those kernels to macroscopic grains. In the following the first step will be called nucleation, the second step growth. Furthermore, one can discriminate between heterogeneous and homogeneous processes contributing to grain formation.

Condensation of vapour on existing dust particles or ions is called *heterogeneous* nucleation. In this section we consider *homogeneous, heteromolecular* nucleation, i.e. the formation of small clusters of molecules by random adsorption and evaporation of single molecules. The regimes of grain nucleation and grain growth are separated

by the critical cluster size N_*. Clusters consisting of less than N_* monomers have a high evaporation probability. This is because their surfaces are strongly curved and the vapour pressure on a curved surface is higher than on a flat surface. N_* is the size of a cluster for which both kinds of vapour pressure are equal (and hence equal to that of the surrounding gas). A cluster consisting of N_* monomers is in equilibrium with the vapour and the probability for growth or evaporation is the same. For an extended review of this classical nucleation theory, see Feder et al. (1966). The value N_* corresponds to a maximum of the free energy ΔG_N and hence to a minimum in the equilibrium density of N–mers, given by

$$n_0(N) = n(1) \exp(-\Delta G_N^0 / k_B T) \qquad (2.46)$$

where $n(1)$ is the concentration of monomers in the vapour.

For self–consistent modelling of the dust forming wind, one is interested in the evolution of Eq.(2.46). The dynamical evolution of the cluster size spectrum is given by the master equation (Gail & Sedlmayr, 1988),

$$\frac{\partial n(N,t)}{\partial t} + \frac{1}{r^2} \frac{\partial (r^2 v_N n(N,t))}{\partial r} =$$
$$R_f(N_-, N) - R_d(N, N_-) - R_f(N, N_+) + R_d(N_+, N) +$$
$$R_f^c(N_-, N) - R_d^c(N, N_-) - R_f^c(N, N_+) + R_d^c(N_+, N) \qquad (2.47)$$

Here, $R_f(N_-, N)$ is the rate of formation of clusters of size N from clusters of size $N_- < N$, $R_d(N, N_-)$ is the rate of destruction of clusters of size N, $R_f(N, N_+)$ is the rate at which clusters of size N grow to become larger clusters by adsorption and $R_d(N_+, N)$ is the rate of production of N–clusters by destruction of larger structures, the rates R^c similarly, denote destruction and formation rates due to chemical reactions of the type (in case of carbon grain formation)

$$C_{N-i} + C_j A_k B_l \ldots \to C_N + C_{j-i} A_k B_l \qquad (2.48)$$
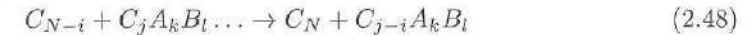
Note that negative values of i correspond to chemical sputtering, grain forming atoms (e.g. carbon) are removed from the cluster surface in collisions. The efficiencies of the destruction and formation processes are, in the case of thermodynamic equilibrium (TE), related by the Milne relations. Although circumstellar dust grains are not in TE with their environment, the Milne relation will be applied to eliminate the evaporation terms from the master equation (Gail & Sedlmayr, 1988). Combining constructive and destructive (reaction) rates one can find an expression for the effective transition rates J_N and J_N^c. The master equation in terms of these transition rates becomes

$$\frac{\partial n(N,t)}{\partial t} + \frac{1}{r^2} \frac{\partial (r^2 v_N n(N,t))}{\partial r} = \sum_{i=1}^{I} J_{N,i} - \sum_{i=1}^{I} J_{N+i,i} + \sum_{i=1}^{I'} J_{N,i}^c - \sum_{i=1}^{I'} J_{N+i,i}^c \qquad (2.49)$$

for $N > I$, I is the maximum size of clusters contributing to nucleation and growth. A further simplification can be achieved by introducing the discrete form of the zeroth moment of the density distribution,

$$K_0(N_l, N_u, t) = \sum_{N=N_l}^{N_u} n(N,t) \qquad (2.50)$$

The dynamical behaviour of K_0 follows directly from Eq.(2.49),

$$\frac{\partial K_0}{\partial t} + \frac{1}{r^2}\frac{\partial(r^2 v_N K_0)}{\partial r} = J(N_l, t) - J(N_u, t) \qquad (2.51)$$

where

$$J(N, t) = \sum_{i=1}^{I}\sum_{j=1}^{i} J_{N-1+j,i} + \sum_{i=1}^{I'}\sum_{j=1}^{i} J^c_{N-1+j,i} \qquad (2.52)$$

is the effective transition rate for all transitions of clusters of sizes $N_- < N$ to clusters of sizes $N_+ > N$. Since arbitrarily large clusters do not exist, the limit for $N_u \to \infty$ of Eq.(2.51) becomes

$$\frac{\partial K_0}{\partial t} + \frac{1}{r^2}\frac{\partial(r^2 v_N K_0)}{\partial r} = J(N_l, t) \qquad (2.53)$$

Here K_0 denotes the total number density of clusters consisting of more than N_l monomers. Consequently, $J(N_l, t)$ is the net formation rate of these clusters. With the choice $N_l = N_*$, $J(N_*, t) = J_*$ becomes the net nucleation rate. Note that the reasoning above is just a sketch of the complete argument, for which the reader is referred to the work of Gail & Sedlmayr (1988).

To proceed, and enable implementation of grain nucleation and growth in time–dependent calculations, we adopt the moment method of dust formation (Gail et al., 1984; Gail & Sedlmayr, 1988; Gauger et al., 1990) in conservation form (Dorfi & Höfner, 1991). The idea of this method is to minimize the amount of information about the characteristics of the size spectrum. It turns out that the time–dependent behaviour of a number of average grain properties (number density, size) can be monitored by following the time dependency of the moments of the density distribution,

$$K_j = \sum_{N=N_l}^{\infty} N^{j/d} n(N, t) \qquad j = 0, \ldots, 3 \qquad (2.54)$$

For spherical grains ($d = 3$), the moments have the following interpretations:

K_0 is the number density of dust grains, n_d
K_3 is the number density of monomers condensed into grains
$r_0 K_1/K_0$ is the average grain radius $\langle r \rangle$
K_3/K_0 is the average grainsize $\langle N \rangle$

The time dependence of the moments is given by

$$\frac{\partial K_0}{\partial t} + \frac{1}{r^2}\frac{\partial(r^2 v_d K_0)}{\partial r} = J_* \qquad (2.55)$$

$$\frac{\partial K_j}{\partial t} + \frac{1}{r^2}\frac{\partial(r^2 v_d K_j)}{\partial r} = \frac{j}{d}\frac{1}{\tau}K_{j-1} + N_l^{j/d} J_* \qquad (2.56)$$

(Gail et al., 1984; Gail & Sedlmayr, 1988; Dorfi & Höfner, 1991). Hence, the moments behave as ordinary flow variables, which allows an easy implementation in the numerical hydrodynamics code. In order to calculate the evolution of the momenta of the grain

density distribution, we need to know the net growth and nucleation rates, $1/\tau$ and $J(N_l, t)$. The latter is given by

$$J(N_l, t) = N_l^{d-1/d}\frac{1}{\tau}n(N_l, t) \qquad (2.57)$$

If $\tau > 0$, we have nucleation and the stationary nucleation rate, $J_* = J(N_*, t)$, i.e. the local current density of clusters flowing upwards in cluster size space at N_* is given by

$$J_* = Z n_0(N_*) A_{N_*} \sum_{i=1}^{I} i^2 n_0(i) v(i) \alpha(i) \qquad (2.58)$$

(Gail et al., 1984; Dorfi & Höfner, 1991), where Z denotes the Zel'dovich factor (of order unity),

$$Z = \left(\frac{1}{2\pi}\left(\frac{\partial^2 \ln n_0(N)}{\partial N^2}\right)_{N_*}\right)^{1/2} \qquad (2.59)$$

and $\alpha(i)$ is the average sticking coefficient. We have adopted the values from Gail et al. (1984): $\alpha(1) = 0.37$ and $\alpha(1) = 0.34$. N_* can be calculated by demanding

$$\frac{\partial \ln n_0(N)}{\partial N} = 0 \qquad (2.60)$$

which results in

$$N_* = 1 + \frac{N_{*,\infty}}{8}\left\{1 + \left[1 + 2\left(\frac{N_h}{N_{*,\infty}}\right)^{1/3}\right]^{1/2} - 2\left(\frac{N_h}{N_{*,\infty}}\right)^{1/3}\right\}^3 \qquad (2.61)$$

$$N_{*,\infty} = \left(\frac{2\Theta_\infty}{3T \ln S}\right)^3 \qquad (2.62)$$

Here, N_h is the particle size for which the surface tension reduces to one half of its value σ for bulk material. The free energy, corresponding to the formation of a cluster of size N from N monomers, is given by

$$\Delta G_N = (N-1)^{2/3}k_B\Theta_N - (N-1)k_B T \ln S \qquad (2.63)$$

(Draine & Salpeter, 1977; Gail et al., 1984), Θ_N is defined as follows

$$\Theta_N = \frac{\Theta_\infty}{1 + [N_h/(N-1)]^{1/3}}; \qquad \Theta_\infty = 4\pi r_0^2 \sigma/k \qquad (2.64)$$

(Gail et al., 1984; Dorfi & Höfner, 1991). The (hypothetical) radius of a monomer, r_0, and the radius of a grain of size N are given by

$$r_0 = \left(\frac{3 A m_p}{4\pi \rho_{gr}}\right)^{1/3} \quad \text{and} \quad r = r_0 N^{1/3} \qquad (2.65)$$

where A is the atomic weight, m_p is the proton mass and ρ_{gr} is the average density of the grain material. The surface of a grain is

$$A_N = 4\pi r_0^2 N^{2/3} \tag{2.66}$$

The supersaturation ratio S is the ratio of the partial pressure of the condensing species in the gas phase and the vapour saturation pressure,

$$S_i = \frac{P_i}{P_{\text{sat},i}} = \frac{n(i)}{n_0(i)} \tag{2.67}$$

The net (growth minus evaporation) growth rate, $1/\tau$, is the sum over the net growth rates of all i-mers contributing to grain growth. Each of these terms consists of the thermal velocity, $v_{\text{th}}(i)$, and the inverse mean free path $iA_1 n(i,t)$, the product of which is the collision frequency. This is multiplied by the average sticking coefficient. The evaporation rate, which is proportional to the inverse of the supersaturation ratio is subtracted. In Eq.(2.56) we use the following expression for the net growth rate, which was adopted from Gauger et al. (1990). The reader is referred to that paper for a detailed derivation.

$$\frac{1}{\tau} = \sum_{i=1}^{I} iA_1 v_{\text{th}}(i)\alpha(i)n(i,t)\left\{1 - \frac{1}{S_1^i}\frac{1}{b_i}\alpha_*(i)\right\} \tag{2.68}$$

Following Dorfi & Höfner (1991), we assume that deviations from thermal and chemical equilibrium are negligible, so that $T_{\text{gas}} = T_{\text{dust}}$ and $\alpha_*(i) = b_i = 1$.

If the net growth rate is positive, the moment equations describe dust formation. Then, the growth rate and the nucleation rate calculated with Eq.(2.58) can be used in Eqs.(2.55,2.56) to update the moments. If the net growth rate is negative, this is due the fact that the supersaturation ratio S is less than unity. In that case, grains will evaporate and the moment equations describe the destruction of dust.

In order to calculate the rate of grain destruction one needs to know the value of the grain size distribution function at the lower size limit N_l, $n(N_l, t)$. Gauger et al. (1990) invented an efficient method to derive this distribution, based on the fact that the rate of change of the grain radius is independent of the grain radius itself.

The inverse of the net growth rate, τ, represents the time needed to add to or remove from a grain of size N, one layer of monomers. Hence,

$$\frac{dN}{dt} = \frac{1}{\tau}N^{d-1/d} \tag{2.69}$$

describes the evolution of the number of monomers, N, in a macroscopic particle. A dimensionless particle radius can be defined by

$$a = N^{1/d} \tag{2.70}$$

and its rate of change is given by

$$\frac{da}{dt} = \frac{1}{\tau d} \tag{2.71}$$

This indeed shows that a changes irrespective of the particle size. This means that the size distribution function for the particle radius, $n(a,t)$, which is defined by

$$n(N,t) = n(a,t)\frac{1}{d}N^{(1-d)/d} \tag{2.72}$$

'maintains' its shape. That is to say, during a phase of grain formation the values of the distribution function (in terms of the grain radius) of dust particles that were formed at time t_0 are shifted to larger radii as a result of growth. The shift is equal for all grain sizes so that the shape of the distribution function is indeed conserved. At the lower side, due to nucleation, new values are added. Once the net growth rate of the grains becomes negative, the distribution curve will be translated in the opposite direction, continuously destroying the smallest grains.

Dominik et al. (1989) showed that the value of the distribution function for the particle that has been formed at time t_0 and at the current time t has size $a_t(t_0)$ is given by

$$n(a_t(t_0),t) = dJ_*(t_0)\tau(t_0) \tag{2.73}$$

Where $J_*(t_0)$ and $1/\tau(t_0)$ represent the nucleation and growth rates at the time t_0 when the particles were created. Note that this is indeed independent of t, i.e. that the distribution function gets fixed at the moment of particle creation. Hence, by the time that the particles that were created at $t = t_0$ will be destroyed, say at $t = t_d$, their number density is still given by Eq.(2.73):

$$n(a_{t_d}(t_0),t_d) = n(a_t(t_0),t) = dJ_*(t_0)\tau(t_0) \tag{2.74}$$

Gauger et al.'s method is based on the following. At the time t_0 when the particles were created, we *know* J_* (from Eq.(2.58)) and τ (from Eq.(2.68)) and from these, using Eq.(2.73), we can *calculate* the value of the distribution function for these particles. By the time the particles will be destroyed we still *know* the value of the distribution function, because it has not changed during the growth and shrinking of the particles, and we will use it to *calculate* the rate at which they will we destroyed, using Eq.(2.57). Therefore, it seems necessary to keep track of the complete particle size distribution. Alternatively, one could just store the values of this function for the smallest particles (of size $a_l = N_l^{1/d}$) and determine the time at which the particles that were created at time $t = t_0$ will be destroyed. In order to do so Gauger et al. (1990), make clever use of the fact that the increase (or decrease) of the particle radius is the same for all sizes of particles, at any time, as follows. We want to determine the value of the grain size distribution function for the particles that formed at time $t = t_0$ and destroyed at $t = t_d$. At both of these instances, immediately after creation and immediately before destruction, the size of these particles is a_l. In the interval between $t = t_0$ and $t = t_d$ the particle radius was larger. Now consider the largest particles present at time $t = t_0$. At $t = t_d$, they too will have reached the same size they had at $t = t_0$. Gauger et al. (1990) realized that the maximum particle radius is a single valued function of time and hence can be used to determine when the particles that formed at $t = t_0$ will, after increasing and subsequently decreasing their radius will again be of size a_l. This time, t_d, can simply be determined if we store the evolution of the maximum grain
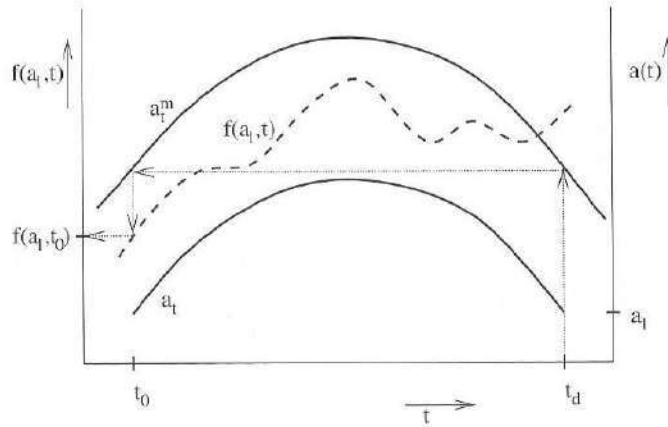
FIGURE 2.3: Determination of $n(a_l, t_0)$. The upper solid line is the evolution of the maximum particle radius as a function of time. The lower solid line is the evolution of the radius of the particle that formed at $t = t_0$ as a function of time. The dashed line represents the evolution of the value of the particle size distribution function for grains of size a_l as a function of time. The arrows correspond to Gaugers method.

size. If the maximum grain size at t_0 is $a_{t_0}^m$, then t_d is the time at which the maximum grain size, for the first time after t_0 is equal to $a_{t_0}^m$.

Hence, in order to determine the value of the grain size distribution function at the lower limit at a time t, $n(a_l, t)$, we determine the maximum grain size at t, say a_t^m. Next, we look up when was the previous time when this size was a_t^m. This gives us the time at which the grains that will evaporate at time t were created. Since we had stored the value of the grain size distribution function for a_l as a function of time we can now determine $n(a_l, t)$ and calculate the grain destruction rate from Eq.(2.57) and Eq.(2.68). This is illustrated in Fig. 2.3.

The gain of Gauger et al.'s method is the fact that it is not necessary to store the complete distribution as a function of time, but that is is sufficient to keep track of its value at the lower size limit, $n(a_l, t)$ and of the evolution of the maximum grain size, which can be calculated with Eq.(2.71).

It should be noted that this method to calculate the evaporation rate of grains is only applicable if grains of various sizes are assumed to have equal velocities. The fact that this is the case in our calculations also facilitates the use of the method in our Eulerian models, whereas it was originally intended to be used in Lagrangian coordinates.

The argumentation given above is only a sketch of Gauger et al.'s method, for the full technical details of it the reader is referred to the original paper (Gauger et al., 1990).

The implementation of the nucleation, growth and evaporation in the code is done as follows. At the beginning of each (half) numerical time step the grain growth rate is calculated from Eq.(2.68). If the growth rate is positive, the nucleation rate is determined, using Eq.(2.58). If the growth rate is negative, grains will evaporate and the evaporation rate can be determined using the method sketched in Fig. 2.3. Once the nucleation and growth or evaporation rates are known, these can be used

to proceed the momenta of the grain size distribution function one (or one half) time step, according to Eq.(2.55) and Eq.(2.56). Note that the mass density of the dust component is proportional to the third moment,

$$\rho_d = \frac{4}{3}\pi a_0^3 \rho_{gr} K_3 \qquad (2.75)$$

where a_0 is the (hypothetical) radius of a monomer and ρ_{gr} is the mass density of the grain material. This means that, when the momenta of the grain size distribution function are treated as fluid variables, there is no more need to take into account the continuity equation for the dust component. The value of the maximum grain size has to be updated as well, by Eq.(2.71). The momenta $K_j, j = 0, \ldots, 3$ and a_m are treated as normal flow variables and updating them is done using the same FCT/LCD scheme as for the density and velocities. The source terms of Eq.(2.55) and Eq.(2.56) register the transfer of matter from the gaseous to the solid phase and will be used as well as source terms in the continuity equations of the density and the total number densities of carbon and hydrogen. This may give rise to a limitation of the time step to be taken. In the case of high nucleation and growth rates the numerical time step should be adjusted in order to avoid that all the gaseous carbon is consumed by dust formation in a single step. It is usually a good idea to allow only 10% of the available carbon to be used per time step. Similarly, in the case of negative growth rates and dust evaporation one has to make sure that the time step is adjusted to avoid the destruction of all the grains in a single time step.

When adjusting the time step to avoid rapid gas depletion or grain destruction, there is a risk of forcing an enormous reduction of the step. In practice, in our calculations the reduction hardly ever was worse than a factor of 100. Larger reductions are often a sign that the gas abundances or the grain densities are locally very low and a special treatment is required.

2.2.3   INTERACTIONS BETWEEN GRAINS AND STELLAR RADIATION

The influence of the dust grains on the dynamics of the envelope is huge. Through scattering and absorption of stellar radiation the grains gain momentum and energy. This gives rise to acceleration and heating of the dust component which will dominate the dynamics and temperature structure in the envelope.

RADIATION PRESSURE ON GRAINS

The radiative force ('radiation pressure'), exerted on dust grains by the radiation field, is actually a magnetic force. Consider an electromagnetic wave, propagating in the x-direction with an electric component E_y and a magnetic component B_z. When incident on a macroscopic particle of electrical conductivity σ_E, the electric component will cause a current $J_y = \sigma_E E_y$. Subsequently, the magnetic component of the electromagnetic wave exerts a force $J_y B_z dxdydz$, or a pressure $J_y B_z dx$, parallel to the direction of wave propagation.

The radiative force exerted on the grains by the radiation field can be calculated as follows. If L_λ is the luminosity of the source at wavelength λ, this source emits

$\lambda L_\lambda / hc$ photons of wavelength λ per second. The momentum associated with each of these photons is h/λ. The fraction of photons of wavelength λ that is intercepted by the grains at radial position r per unit volume is

$$\frac{\kappa_\lambda \rho_{\rm d}}{4\pi r^2} = \frac{1}{4\pi r^2} \int_0^\infty \pi a^2 Q_{\rm pr}(a,\lambda)n(a)da \qquad (2.76)$$

and the radiative force is

$$f_{\rm rad} = \frac{\int L_\lambda \kappa_\lambda \rho_{\rm d} {\rm d}\lambda}{4\pi r^2 c} \qquad (2.77)$$

where κ_λ is the mass extinction coefficient and $n(a)$ is the number density of grains with radii between a and $a+da$. $Q_{\rm pr}(a,\lambda)$ is the efficiency factor for radiation pressure, which accounts for the amount of momentum that is removed from the incident beam and consists of a scattering and an absorption part. The absorbed radiation is removed from the beam completely whereas the radiation that is scattered at angle θ with respect to the incident beam will still contribute partially:

$$Q_{\rm pr}(a,\lambda) = Q_{\rm ext}(a,\lambda) - g_\lambda Q_{\rm sca}(a,\lambda) = Q_{\rm abs}(a,\lambda) + Q_{\rm sca}(a,\lambda) - g_\lambda Q_{\rm sca}(a,\lambda) \quad (2.78)$$

where g_λ is the mean cosine of the scattering angle θ. It turns out, see e.g. Lamers & Cassinelli (1999), that for wavelengths beyond approximately 2 μm scattering is almost isotropic, so that $g_\lambda = 0$. Hence, in the following, we will use the extinction efficiency factor $Q_{\rm ext}$ instead of the radiation pressure efficiency $Q_{\rm pr}$.

To proceed, we assume that the grain radius is small compared with the mean wavelength of the radiation field, so that the mass extinction coefficient can be calculated in the small particle limit of Mie theory (c.f. Lucy (1976), Fleischer et al. (1992) and references therein). The integral in Eq.(2.76) can then be replaced by

$$\rho_{\rm d}\kappa_{\rm d} = \frac{3}{4}V_0 K_3 Q'(T) \qquad (2.79)$$

see Fleischer et al. (1992). Here V_0 is the volume per monomer for the grains, K_3 is the third moment of the grain size distribution function (see previous section) and the extinction efficiency of the grain material can be approximated by its Rosseland mean which is approximately given by

$$Q'(T) = 5.9T_* \qquad (2.80)$$

(Fleischer et al., 1992). With the grey dust opacity given in Eq.(2.79), the radiative force on the grains becomes

$$f_{\rm rad} = \frac{L_* \kappa_{\rm d} \rho_{\rm d}}{4\pi r^2 c} \qquad (2.81)$$

This force appears in the source term of the momentum equation for the dust. It is often assumed that the dust will transfer all the momentum due to radiation pressure directly to the grains and that gas and grains have the same velocity. In that case, the dust momentum equation is omitted and the radiative force is incorporated as a source term in the gas momentum equation. We will, in Chapter 3, point out that it is preferable to treat gas and dust as separate fluids. If gas and dust are assumed to be completely coupled, various important physical effects are suppressed.

TEMPERATURE STRATIFICATION

Instead of solving the energy equation and having to calculate cooling and heating rates, we simply assume that the gas temperature is given by the local radiative equilibrium temperature, $T_{\rm eq}$. This temperature is found through semi-analytically solving the radiative transfer, in a way similar to the one described by Lucy (1976) and Fleischer et al. (1992). We realize that simultaneously solving the full radiative transfer problem and the hydrodynamics would be superior to this approach. This, however, requires an enormous amount of computer time which we currently prefer to spend on a large time coverage of our computations.

The transfer equation, taking into account coherent, isotropic scattering in a spherical, static envelope around a spherical radiation source, is (Lucy, 1971)

$$\mu\frac{\partial I_\nu}{\partial r} + \frac{1-\mu^2}{r}\frac{\partial I_\nu}{\partial \mu} = -\kappa_\nu \rho(I_\nu - J_\nu) \qquad (2.82)$$

A modified version of the Eddington approximation that takes into account the curvature of the atmosphere is given by

$$J - 3K + \frac{1}{2}\mu_* F = 0 \qquad (2.83)$$

where $\mu_* = \sqrt{1-(R_*/r)^2}$. With this modified Eddington approximation the first two moments of the transfer equation, assuming a gray atmosphere, can be integrated to find

$$F(r) = (R_*/r)^2 \mathcal{F} \qquad (2.84)$$

$$J(r) = \mathcal{F}\left[W(r) + \frac{3}{4}\int_0^\infty \kappa_{\rm tot}\rho\left(\frac{R_*}{r}\right)^2 {\rm d}r\right] \qquad (2.85)$$

(Lucy, 1976), where $\pi\mathcal{F}$ is the integrated flux at R_*. Here, $\kappa_{\rm tot}$ is the total mass extinction coefficient of gas and dust, $\kappa_{\rm tot} = \kappa_{\rm g} + \kappa_{\rm d}$ and $W(r)$ is the geometrical dilution factor,

$$W(r) = \frac{1}{2}\left[1 - \left(1 - \left(\frac{R_*}{r}\right)^2\right)^{1/2}\right] \qquad (2.86)$$

If the atmosphere is in radiative equilibrium, we have $J = B$, where $B = (\sigma/\pi)T^4$ is the integrated Planck function. The integrated flux at the photosphere is $\sigma T_*^4 = \pi\mathcal{F}$. Combining this information, we find an expression for the equilibrium temperature in the envelope (Lucy, 1976; Fleischer et al., 1992)

$$T_{\rm eq}^4(r) = \frac{1}{2}T_*^4\left[2W(r) + \frac{3}{2}\tau_{\rm tot}\right] \qquad (2.87)$$

with the modified total optical depth

$$\tau_{\rm tot} = \int_0^\infty \kappa_{\rm tot}\rho\left(\frac{R_*}{r}\right)^2 {\rm d}r \qquad (2.88)$$

The total mass extinction coefficient, κ_{tot}, is the sum of the extinction coefficients of the gas and the dust. The latter was calculated in the previous paragraph, the gas extinction coefficient is assumed to be constant throughout the envelope and is adopted from Fleischer et al. (1992), $\kappa_g = 2.0 \times 10^{-4} \text{cm}^2\text{g}^{-1}$.

The calculation of the temperature profile is performed once every numerical time step, immediately before updating the equilibrium gas chemistry.

2.2.4 TWO FLUID HYDRODYNAMICS: GAS-GRAIN INTERACTION

Grains that are radiatively accelerated frequently collide with gas particles (direct radiation pressure on the gas is negligible). In these collisions momentum is transferred to the gas. The amount of momentum transferred in a single collision is proportional to the velocity difference between both, the *drift velocity* v_D. The rate of gas-grain collisions is proportional to the drift velocity as well, provided the drift velocity is higher than the thermal velocity. Hence, the *drag force* between gas and grain is often implemented in the form (Dominik, 1992)

$$f_{\text{drag}} = \Sigma_d n_g n_d m_g v_{\text{th}}^2 \left(\frac{64}{9\pi} \left(\frac{v_D}{v_{\text{th}}} \right)^2 + \left(\frac{v_D}{v_{\text{th}}} \right)^4 \right)^{1/2} \tag{2.89}$$

The drag force increases with increasing drift velocity. Therefore, there exists an equilibrium value $\bar{v}_D$ (Dominik, 1992). Two common ways to incorporate radiation pressure on dust and the subsequent transfer of momentum to the gas are based on assumptions about the drift velocity. First, in *single fluid* calculations it is assumed that $v_D = 0$. The momentum equation for the dust does not need to be calculated and the drag force in the gas momentum equation is simply replaced by the radiative force, Eq.(2.81). The second implementation assumes that grains always drift at their equilibrium drift velocity. This velocity can be calculated by equating the drag force and the radiative force. Since the relative velocity of the grains with respect to the gas is known, there is no need to solve the momentum equation of the grain. In order to calculate the velocity of the gas, its momentum equation is solved by replacing the drag force by the radiative force. We will refer to this method as *1.5 fluid hydrodynamics*, since it is in between single and two-fluid approaches. The assumptions made in single and 1.5 fluid hydrodynamics seem justified if equilibrium drift is reached rapidly and/or if the drift velocity is small compared to the gas velocity. One should realize however that, by replacing the drag force by the radiative force in the gas momentum equation, one in fact stipulates that the grains carry no mass. Also, in the single fluid approximation, the system misses a degree of freedom, namely the relative motion of the grains with respect to the gas. In the 1.5 fluid case, the grains can move independently of the gas, though not freely.

In two-fluid hydrodynamics, the full system with both the gas and the dust momentum equations is solved. When using an explicit method, using Eq.(2.89) for the drag force will enforce very small numerical time steps. As a consequence of the quadratic dependence on the drift velocity, the characteristic time scale of the drag force can be many orders of magnitude smaller than the time scales of the other forces (gravity, radiation pressure) and the dynamical time scale. This means that, in order to avoid
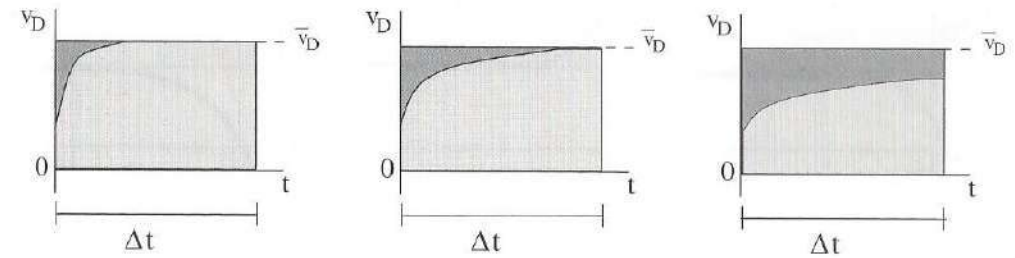

FIGURE 2.4: Evolution towards equilibrium drift within a single time step: because it may take some time to establish equilibrium, calculating the momentum transfer by simply multiplying the drag force (which is proportional to v_D^2) with Δt overestimates the momentum transfer. The difference between the exact calculation and the equilibrium calculation increases with the time required to establish equilibrium drift and is represented by the dark colour in the figures.

errors, the time step should be adjusted to that of the drag force, which may be many orders of magnitude smaller than the CFL time step. This is not what one wants, since taking small time steps will lead to inaccuracy (because then more steps are needed to cover the same simulation time, and in each step there is the risk of systematic errors). In order to be able to perform two-fluid hydrodynamics in an explicit calculation we will study the behaviour of the gas-grain system on small length and time scales, i.e. on a subgrid level. Doing so, we will essentially derive an alternative expression to Eq.(2.89) that is based on the same physics but is suitable for implementation in an explicit calculation.

To derive an expression for the drag force, we need to know the evolution of the drift velocity. The gas-grain system always evolves towards a state in which grains drift at the equilibrium speed, hence in which gas and grains undergo the same acceleration. Whether, or how rapidly, this state is reached depends on the time needed to establish the equilibrium relative to the dynamical time scale. If one assumes that equilibrium drift is always valid, the momentum transfer in a numerical time step can simply be calculated by using the equilibrium value of the drift velocity in Eq.(2.89) and multiplying the drag force by the time step. However, if, during a fraction of the step, the drift velocity is lower than the equilibrium value, assuming equilibrium drift when calculating the drag force overestimates the momentum transfer. This is illustrated in Fig. 2.4. Although the error for a single time step may be very small, the implications may be large for the time dependent calculation. Note that, when assuming equilibrium drift, one fixes the value of the drift velocity so that the gas and the dust velocities are no longer independent flow variables. Therefore, when calculating the momentum transfer assuming equilibrium drift, one is forced to do a 1.5-fluid calculation rather than a full two-fluid calculation. We will, hereafter, derive an expression for the evolution of the drift velocity. With this expression we can calculate the momentum transfer as the integral of the drag force over the numerical time step. No assumptions about the final drift velocity need to be made and the derived expression can be used in a full two-fluid calculation.

It is important to note that even if we find equilibrium drift in the two component calculation, this does not imply that it would have been justified to assume equilibrium drift a priori. This can be seen from Fig. 2.4. In both the first and the second panel
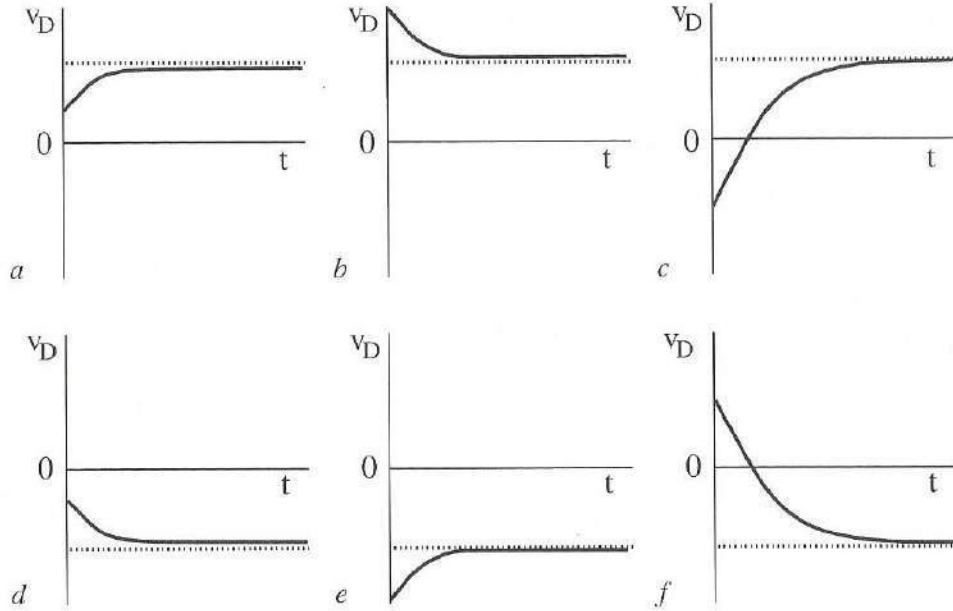
FIGURE 2.5: Evolution towards equilibrium drift for various initial drift velocities. Upper panels: $g_{D,tot} > 0 \rightarrow \bar{v}_D > 0$, lower panels: $g_{D,tot} < 0 \rightarrow \bar{v}_D < 0$

equilibrium drift is established within the duration of the numerical time step, Δt, i.e., in both cases the output of the hydrodynamics indicates equilibrium drift. Assuming equilibrium drift throughout the time step would however only slightly overestimate the momentum transfer in the first panel whereas in the second panel the difference between the exact integral of the drag force over the time step and equilibrium approximation would be much bigger.

AN ANALYTICAL EXPRESSION FOR THE MOMENTUM TRANSFER RATE

In this section we will derive an expression for the time evolution of the drift velocity. Using this expression we can calculate the rate at which momentum is transferred from grains to gas.

Fig. 2.5 shows the six possible cases for reaching equilibrium drift. Note that both the initial drift and the equilibrium value can be negative if the grains are less accelerated than the gas. We assume that the gas–grain interactions are completely inelastic. Furthermore, we assume that after a collision with a grain, a gas particle shares the acquired momentum with the surrounding gas instantaneously (thermalization). This is realistic, since the mean free path of gas–gas collisions is very small compared to the mean free path for gas–grain encounters. We will not take into account thermal motion because this enables us to derive an analytic expression for the drag force. This will result in a somewhat lower momentum transfer in the subsonic region. Farther out, the drift velocity of the grains will dominate the collision rate anyway.

First, consider the motion of an individual gas particle between two subsequent collisions with a grain:

$$v_g \rightarrow v_g + g_{g,tot}\delta t + \frac{n_d}{n_g}\frac{\Delta p}{m_g} \qquad (2.90)$$

Here, v_g is the velocity of the particle, after the previous collision, $g_{g,tot}$ is the total acceleration due to gravity and the pressure gradient (but not the drag force), δt is the time interval between two collisions. The last term represents the increase in the velocity as a result of the encounter with the grain, and the (instantaneous) redistribution of the momentum amongst the gas. Δp is the amount of momentum transferred in a single gas–grain collision,

$$\Delta p = \frac{m_g m_d}{m_g + m_d}u_D \qquad (2.91)$$

where u_D is the velocity of a grain with respect to the gas immediately before the collision, $m_{g,d}$ are the masses of a gas particle (i.e. the mean molecular weight) and the (average) grain mass. A similar equation for the dust grain is

$$v_d \rightarrow v_d + g_{d,tot}\delta t - \frac{\Delta p}{m_d} \qquad (2.92)$$

The drift velocity after a collision, v_D, can now be expressed in terms of the drift velocity immediately before the encounter, u_D, as follows:

$$v_D = \Omega u_D \qquad (2.93)$$

in which

$$\Omega = \frac{\rho_g m_d - \rho_d m_g}{\rho_g(m_g + m_d)} \qquad (2.94)$$

$$u_D = u_d - u_g = v_d - v_g + (g_{d,tot} - g_{g,tot})\delta t \qquad (2.95)$$

In the following, we will write $g_{D,tot}$ for the relative acceleration, $g_{d,tot} - g_{g,tot}$. The 'mean free travel time', δt, of a grain can be found by solving the quadratic equation for the mean free path, λ, of a grain

$$\lambda = v_D\delta t + \frac{1}{2}g_{D,tot}\delta t^2 \qquad (2.96)$$

Note that the mean free path can become negative if the initial drift velocity, v_D, and/or the relative acceleration $g_{D,tot}$ is negative. If grains are not significantly accelerated between two subsequent collisions with gas particles, i.e. if $v_D \gg g_{D,tot}\delta t$, Eq.(2.96) simply becomes

$$\lambda = v_D\delta t \qquad (2.97)$$

so that $\delta t = \lambda/v_D$. On the other hand, if the acceleration of a grain between two collisions is so large that its initial (drift) velocity is negligible, Eq.(2.96) reads

$$\lambda = \frac{1}{2}g_{D,tot}\delta t^2 \qquad (2.98)$$

and $\delta t = \sqrt{2\lambda/g_{\mathrm{D,tot}}}$. The boundary between the two regimes lies at the drift velocity for which $2v_{\mathrm{D}} = g_{\mathrm{D,tot}}\delta t$. With δt given by the solution of Eq.(2.96) we find that if

$$|v_{\mathrm{D}}| < \frac{1}{2}\sqrt{\lambda g_{\mathrm{D,tot}}} \qquad (2.99)$$

Eq.(2.98) can be used instead of Eq.(2.96). In the current context of dust forming stellar winds, the quantity Ω will always be nearly equal to unity[3], so that $\bar{v}_{\mathrm{D}} \gg (\lambda g_{\mathrm{D,tot}})^{1/2}/2$. Hence, the zone in velocity space where grain acceleration is significant is extremely narrow. If the drift velocity is zero at some time (see e.g. Fig. 2.5.c,f), it follows from Eq.(2.93), (2.95) and (2.98) that the drift velocity will be larger than $(\lambda g_{\mathrm{D,tot}})^{1/2}/2$ after a single collision unless $\Omega < 8^{-1/2}$. This implies that we can safely apply Eq.(2.97) for all values of v_{D}.

In the following we will present a method to derive an expression for the momentum transfer, which applies to all possible scenarios (see Fig. 2.5) to reach equilibrium drift. We limit ourselves to the derivation for the case $g_{\mathrm{D,tot}} > 0$ (Fig. 2.5.a,b,c), the derivation for negative acceleration is analogous.

Application of Eq.(2.97) and Eq.(2.95) in Eq.(2.93) gives rise directly to a recurrence relation for v_{D}:

$$v_{\mathrm{D}}(t_{i+1}) = \Omega u_{\mathrm{D}}(t_{i+1}) = \Omega\left(v_{\mathrm{D}}(t_i) + \frac{g_{\mathrm{D,tot}}\lambda}{v_{\mathrm{D}}(t_i)}\right) \qquad (2.100)$$

From this, and δt given by Eq.(2.97), a differential equation for the drift velocity as a function of time can be derived:

$$\frac{\Delta v_{\mathrm{D}}}{\Delta t} \simeq \frac{dv_{\mathrm{D}}}{dt} = \frac{\Omega - 1}{\lambda}v_{\mathrm{D}}^2 + \Omega g_{\mathrm{D,tot}} \qquad (2.101)$$

This equation can be easily solved for $t(v_{\mathrm{D}})$,

$$t(v_{\mathrm{D}}) = \frac{\lambda}{\sqrt{\Omega(\Omega-1)g\lambda}}$$
$$\left[\arctan\left(\frac{(\Omega-1)v_{\mathrm{D}}(t)}{\sqrt{\Omega(\Omega-1)g\lambda}}\right) - \arctan\left(\frac{(\Omega-1)v_{\mathrm{D}}(0)}{\sqrt{\Omega(\Omega-1)g\lambda}}\right)\right] \qquad (2.102)$$

where g stands for $g_{\mathrm{D,tot}}$.

First, consider the case where $v_{\mathrm{D}}(0) > 0$ (and $g > 0$). In this case the mean free path λ will always be positive. Because Ω is always smaller than unity and λ and g have equal signs this is rewritten as

$$t(v_{\mathrm{D}}) = \frac{\lambda}{\sqrt{\Omega(1-\Omega)g\lambda}}$$
$$\left[\mathrm{arctanh}\left(\frac{(1-\Omega)v_{\mathrm{D}}(t)}{\sqrt{\Omega(1-\Omega)g\lambda}}\right) - \mathrm{arctanh}\left(\frac{(1-\Omega)v_{\mathrm{D}}(0)}{\sqrt{\Omega(1-\Omega)g\lambda}}\right)\right] \qquad (2.103)$$

---
[3]E.g. for a typical dust to gas mass ratio $\rho_{\mathrm{d}}/\rho_{\mathrm{g}} = 1.0 \times 10^{-2}$ and for grains consisting of 10^{10} monomers ($m_{\mathrm{d}}/m_{\mathrm{g}} = 1.0 \times 10^{10}$) we find $\Omega \approx 1 - 10^{-10}$.

This expression can be simplified by realizing that from Eq.(2.100) it follows that the equilibrium drift velocity is given by

$$\bar{v}_{\mathrm{D}} = \left(\frac{\Omega}{1-\Omega}\lambda g\right)^{1/2} \qquad (2.104)$$

and that the equilibration time scale is

$$\tau_{\mathrm{eq}} = \frac{1}{\sqrt{\Omega(1-\Omega)g/\lambda}} \qquad (2.105)$$

so that

$$t(v_{\mathrm{D}}) = \tau_{\mathrm{eq}}\left[\mathrm{arctanh}\left(\frac{v_{\mathrm{D}}(t)}{\bar{v}_{\mathrm{D}}}\right) - \mathrm{arctanh}\left(\frac{v_{\mathrm{D}}(0)}{\bar{v}_{\mathrm{D}}}\right)\right] \qquad (2.106)$$

$$= \tau_{\mathrm{eq}}\,\mathrm{arctanh}\left(\frac{(v_{\mathrm{D}}(t) - v_{\mathrm{D}}(0))\bar{v}_{\mathrm{D}}}{\bar{v}_{\mathrm{D}}^2 - v_{\mathrm{D}}(t)v_{\mathrm{D}}(0)}\right) \qquad (2.107)$$

Note that addition of the arctanh terms causes the expression to be valid for initial values $v_{\mathrm{D}}(0) > \bar{v}_{\mathrm{D}}$ (see Fig. 2.5.b) as well. Inversion leads to an expression for the drift velocity as a function of time:

$$v_{\mathrm{D}}(t) = \bar{v}_{\mathrm{D}}\frac{v_{\mathrm{D}}(0) + \bar{v}_{\mathrm{D}}\Theta(t)}{\bar{v}_{\mathrm{D}} + v_{\mathrm{D}}(0)\Theta(t)} \qquad (2.108)$$

with

$$\Theta(t) = \tanh(t/\tau_{\mathrm{eq}}) \qquad (2.109)$$

The drag force (density) is the product of the number of gas–grain collisions per unit volume and time and the momentum transfer per collision. In Eq.(2.40), the amount of momentum transfer in a single collision was simply assumed to be $m_{\mathrm{g}}v_{\mathrm{D}}$, now we use the more accurate form for Δp which follows from Eqs.(2.91), (2.93), (2.97). With $\lambda = 1/\Sigma_{\mathrm{d}}n_{\mathrm{g}}$ we then find

$$f_{\mathrm{drag}} = \Sigma_{\mathrm{d}}\rho_{\mathrm{g}}\frac{n_{\mathrm{g}}n_{\mathrm{d}}}{n_{\mathrm{g}}-n_{\mathrm{d}}}|v_{\mathrm{D}}|v_{\mathrm{D}} \qquad (2.110)$$

The standard way to calculate the amount of momentum transfer per numerical time step is simply multiplying the drag force with the duration of the time step. Now that we have derived an expression for the drift velocity as a function of time we can calculate the momentum transfer more accurate, by integrating Eq.(2.110), assuming $n_{\mathrm{g,d}}, m_{\mathrm{g,d}}$ are constant:

$$\int_0^\tau f_{\mathrm{drag}}dt = \Sigma_{\mathrm{d}}\rho_{\mathrm{g}}\frac{n_{\mathrm{g}}n_{\mathrm{d}}}{n_{\mathrm{g}}-n_{\mathrm{d}}}\tau_{\mathrm{eq}}\bar{v}_{\mathrm{D}}^2$$
$$\left[\frac{\tau}{\tau_{\mathrm{eq}}} + \left(\frac{v_{\mathrm{D}}(0)}{\bar{v}_{\mathrm{D}}} - \frac{\bar{v}_{\mathrm{D}}}{v_{\mathrm{D}}(0)}\right)\left(\frac{v_{\mathrm{D}}(0)\tanh(\tau/\tau_{\mathrm{eq}})}{v_{\mathrm{D}}(0)\tanh(\tau/\tau_{\mathrm{eq}}) + \bar{v}_{\mathrm{D}}}\right)\right] \qquad (2.111)$$

If the initial drift velocity and the total acceleration have opposite sign ($v_D(0) < 0, g > 0$, see Fig. 2.5.c) the integral representing the total momentum transfer is split into two parts,

$$\int_0^\tau f_{\mathrm{drag}}\mathrm{d}t = \int_0^{t(v_D=0)} f_{\mathrm{drag}}\mathrm{d}t + \int_{t(v_D=0)}^\tau f_{\mathrm{drag}}\mathrm{d}t \qquad (2.112)$$

where $t(v_D = 0)$ follows from Eq.(2.102):

$$t(v_D = 0) = \frac{-\lambda}{\sqrt{\Omega(\Omega - 1)g\lambda}} \arctan\left(\frac{(\Omega - 1)v_D(0)}{\sqrt{\Omega(\Omega - 1)g\lambda}}\right) \qquad (2.113)$$

Note that the mean free path of a grain, λ, is negative as long as the drift velocity is negative. The second term in Eq.(2.112) is calculated as in the case $v_D(0) > 0$, simply taking $v_D(0) = 0$. In order to compute the first term, Eq.(2.102) is inverted. We find

$$v_D(t) = \bar{v}_D \frac{v_D(0) + \bar{v}_D \Theta'(t)}{\bar{v}_D - v_D(0)\Theta'(t)} \qquad (2.114)$$

in which

$$\Theta'(t) = \tan(t/\tau'_{\mathrm{eq}}) \qquad (2.115)$$

$$\bar{v}_D = \sqrt{\frac{\Omega}{\Omega - 1}\lambda g} \qquad (2.116)$$

$$\tau'_{\mathrm{eq}} = \frac{1}{\sqrt{\Omega(\Omega - 1)g/\lambda}} \qquad (2.117)$$

Inserting this into Eq.(2.110) and integrating over the interval $t = 0, t(v_D = 0)$, we obtain

$$\int_0^{t(v_D=0)} f_{\mathrm{drag}}\mathrm{d}t = -\Sigma_d\rho_g \frac{n_g n_d}{n_g - n_d}\tau'_{\mathrm{eq}}\bar{v}_D^2 \left[-\frac{v_D(0)}{\bar{v}_D} + \arctan\left(\frac{v_D(0)}{\bar{v}_D}\right)\right] \qquad (2.118)$$

Note that the minus sign accounts for the fact that the momentum transfer contains an integral over $|v_D|v_D$ rather than an integral over v_D^2. Finally, for the complete integral, Eq.(2.112), we find

$$\int_0^\tau f_{\mathrm{drag}}\mathrm{d}t = \Sigma_d\rho_g \frac{n_g n_d}{n_g - n_d}\tau_{\mathrm{eq}}\bar{v}_D^2$$
$$\left[\frac{\tau}{\tau_{\mathrm{eq}}} - \tanh\left(\frac{\tau}{\tau_{\mathrm{eq}}} + \arctan\left(\frac{v_D(0)}{\bar{v}_D}\right)\right) + \frac{v_D(0)}{\bar{v}_D}\right] \qquad (2.119)$$

As was to be expected Eq.(2.111) and Eq.(2.119) are equal if $v_D(0) = 0$.

Similar expressions for the total momentum transfer can be calculated in the case of negative total acceleration (see Fig. 2.5.d,e,f).

The above formulations for the momentum transfer, in which no assumptions about the value of the drift velocity or the completeness of momentum coupling have been made, can be used as source terms in the momentum equations.

2.2.5 CALCULATION OF THE EQUILIBRIUM DRIFT VELOCITY

We have used the terms equilibrium drift velocity and limiting velocity as equivalent. Here, we will show that both are indeed the same. We equate the acceleration of the gas and the dust, rather than equating the drag force and the radiation pressure of grains. In the latter case one implicitly assumes that grains do not have mass whereas the former leads to a general expression for the equilibrium drift velocity.

From the equation of motion of a gas element,

$$\frac{\mathrm{d}v_g}{\mathrm{d}t} = g_{g,\mathrm{tot}} + \frac{f_{\mathrm{drag}}}{\rho_g} \qquad (2.120)$$

and its counterpart for a grain,

$$\frac{\mathrm{d}v_d}{\mathrm{d}t} = g_{d,\mathrm{tot}} - \frac{f_{\mathrm{drag}}}{\rho_d} \qquad (2.121)$$

we find that grains and gas are equally accelerated, and hence the drift velocity has reached its equilibrium value, if

$$g_{D,\mathrm{tot}} = \frac{\rho_d + \rho_g}{\rho_d\rho_g}f_{\mathrm{drag}} \qquad (2.122)$$

With Eq.(2.110), the equilibrium drift velocity is

$$\bar{v}_D = \left(\frac{m_d(n_g - n_d)}{\rho_d + \rho_g}g_{D,\mathrm{tot}}\lambda\right)^{1/2} \qquad (2.123)$$

Thus, we have now derived an expression for the equilibrium drift velocity without having to assume complete momentum coupling. This expression is indeed the same as Eq.(2.104), which represents the limiting drift velocity.

2.2.6 STELLAR PULSATION

The fact that AGB stars are long-period variables (LPVs) with a pulsation period of a few hundred up to a thousand days influences the wind. Through stellar pulsation, the atmosphere can be levitated, and relatively cool and dense regions which facilitate dust nucleation and growth may arise. Stellar pulsation is not included in our calculations: the star is located outside our computational grid (the innermost grid point is taken to be at or close to the stellar photosphere). Hence, if we want to study the influence of the stellar pulsation on the wind we must incorporate it as an inner boundary condition. This is easy, since at the inner boundary we will have to prescribe the values of our flow variables in a few cells anyway (see next section). We simply prescribe a sinusoidal variation of the velocity, with a fixed period and amplitude.

2.3 INITIAL AND BOUNDARY CONDITIONS, TRANSIENT SOLUTIONS

Reasonable prescriptions for the flow variables at the start of the calculation and at the edges of the grid are a requirement for a realistic model calculation. Numerical

hydrodynamics is often applied to problems that are too complicated to solve analytically. Ideally, though, we would like to start our calculation from an analytic solution because we would like an initial profile that is as close as possible to a solution of our equations, in order to enable a smooth start of the calculation. If available, it may turn out convenient to start the numerical calculation from a solution of the stationary equations. Alternatively, the starting procedure may mimic the true onset of the wind, i.e. start with a hydrostatic solution, with low densities and zero velocity. The problem with the latter is that the densities cannot be taken arbitrarily low, since for extremely low densities hydrodynamics is not applicable at all. Another problem that arises in starting a numerical hydrodynamics calculation is the initial transient. These solutions are mathematically correct, but do not necessarily represent a realistic physical state. A solution in which the matter flows at superluminal speed does not violate the continuity equations if the density is low enough. Still, it is not a realistic solution for the AGB wind problem. The transient can behave so badly that the calculation gets stuck, e.g. very high concentrations of matter can lead to temperatures that are too high to calculate the chemical processes. In order to avoid transient solutions it is wise to take an initial profile that is close to an expected solution of the problem. The occurrence of transients, as long as they do not hinder the calculation, should then be no problem. One should however wait to interpret the results of the calculation until the transient has streamed off the grid. Another possibility is to 'unroll' the grid in the course of the calculation. This can be done by extending the grid with one cell, in radial direction, every time the density and velocity in the currently outermost cell have reached physically reasonable values. This way, no computer time is lost in calculating the passage of the transient.

The impact of the boundary conditions is often underestimated. It is necessary to prescribe the values of the flow variables in at least the first and the last cell of the grid. This is because with our finite difference scheme we can only consistently update the flow variables in a certain cell if we know the values in the neighbouring cells at the previous time step, see Eq. (2.2). The outermost and innermost cells for which we have to prescribe the values of the flow variables are called *ghost cells*. It can be necessary to have more than one ghost cell at each boundary, e.g. when the corrective flux terms involve higher derivatives, which are calculated using the second neighbours.

In the case of a spherically symmetric dust driven wind model, calculation of the outer boundary poses no problem but the inner boundary treatment is of great importance. We will choose our grid big enough so that, in the case of a stellar wind, the velocities at the outer boundary are supersonic. Hence, no information from outside the grid can flow in and we can simply use extrapolation to determine the value. The inner boundary, where the flow is subsonic, is more complicated. There, pressure waves can run both upstream and downstream and there is a mutual influence of the region that falls within the grid and the region that is not covered. There is no solution to this problem. The best thing to do is to make a reasonable choice for the values of the flow variables in the ghost cells. This prescription can be time-dependent, in order to mimic stellar pulsation in the form of a piston or to follow stellar evolution. Such a time dependent inner boundary is meant to influence the flow on the grid. Sometimes, as in the calculations in Chapter 3, one rather wants an inner boundary that influences the results as little as possible. Simply keeping the flow variables, or the associated

fluxes, constant is an option in that case. But, in a way, this also influences the flow on the grid, since such boundary conditions fix the rate at which mass and/or momentum flow in. In order to influence the flow on the grid as little as possible we suggest the following. At the inner boundary we do fix the density and velocity of the gas (dust is not present there), which essentially means that we fix the advective mass and momentum inflow. At the same time we do not suppress numerical viscosity, i.e. we do not use anti-diffusion and FCT/LCD. This means that, depending on the density and velocity gradients near the inner boundary (which are not fixed because these derivatives also depend on the flow variables within the grid), matter and momentum can diffuse in or out, in addition to the fixed advective fluxes. Hence, we have created a flexible inner boundary, for which we have fixed the values of the flow variables in the ghost cells but for which the total fluxes are also determined by the flow on the grid itself.

2.4   PERFORMING MODEL CALCULATIONS

We have provided an overview of the physical processes taken into account in our AGB wind code and have elucidated their implementation. Since the code is self–consistent, only six parameters have to be provided as input for a calculation. These are, the stellar mass (M_*), luminosity (L_*) and effective temperature (T_*), the carbon–to–oxygen abundance ratio ϵ_C/ϵ_O, the period of the piston (P) and its velocity amplitude (Δv). If stellar pulsation is not taken into account, the latter two parameters are omitted. For these parameters an initial hydrostatic state is calculated and thereafter the time dependent calculation can start. Alternatively, an externally prescribed initial profile, e.g. a solution of the stationary system, with its parameters can be read into the code.

Output generated during the calculation involves a wide variety of variables relevant to the flow. For example: velocities (for both gas and dust), densities, grain sizes, grain number densities, abundances of gas phase elements etc.

The main difference between our AGB wind code and codes from other authors is the fact that we allow for grain drift. In order to investigate the consequences of drift, we also need to be able to run our code in single fluid mode. This option was indeed built into the code. In single fluid mode the momentum due to radiation pressure on dust is completely and directly transferred to the gas. The momentum balance for the dust is not evaluated, the velocity of the dust is taken equal to the gas velocity.

When taking into account grain drift, there are two options. Firstly, full two fluid hydrodynamics, in which the momentum equations for both gas and dust are taken into account. The second mode is 1.5-fluid hydrodynamics, in which grains are assumed to drift at their equilibrium drift speed. The dust velocity is found by adding this drift velocity and the gas velocity, so that evaluation of the dust momentum equation is not necessary. Note that we have, in Section 2.2.5, derived an expression for the equilibrium drift velocity based on equal acceleration of gas and dust. With this expression, in contrast with previous expressions, grains are no longer implicitly assumed to be massless. In the next chapter, we will extensively discuss the difference between the three types of calculations.

TABLE 2.1: Stellar mass, temperature, luminosity and piston period for 20 single fluid models. The carbon-to-oxygen ratio ϵ_C/ϵ_O is 1.8 and the piston amplitude Δv is 2.0 km s^{-1} in all models. $\langle \dot{M} \rangle$ is the resulting time averaged mass loss rate, $\dot{M}_A$ is the mass loss rate according to Arndt et al.'s approximative equation. $\langle v_\infty \rangle$ is the average velocity at 15 R_* and $v_{\infty,A}$ is the predicted value for this velocity resulting from the approximative equation.

model		M_* [$M_\odot$]	T_* [10^3 K]	L_* [$10^4 L_\odot$]	P [days]	$\langle \log \dot{M} \rangle$ [$M_\odot$ y^{-1}]	$\log \dot{M}_A$ [$M_\odot$ y^{-1}]	$\langle v_\infty \rangle$ [km s^{-1}]	$v_{\infty,A}$ [km s^{-1}]
t1_1F		1.7236	2.500	1.3964	1412	-6.3305	-5.2670	16.84	25.15
t2_1F		1.6090	2.460	1.4289	1635	-6.0869	-5.1018	20.31	25.74
t3_1F		1.5226	2.438	1.4355	1788	-5.9183	-4.9931	22.42	26.10
t4_1F		1.4108	2.415	1.4421	1995	-5.6619	-4.8819	25.25	26.55
t5_1F		1.2807	2.427	1.3335	1979	-5.6001	-4.8381	25.59	26.46
t7_1F		1.1792	2.427	1.4191	2264	-5.2125	-4.6910	28.53	27.13
t8_1F		1.0719	2.477	1.4422	2318	-5.0404	-4.6446	27.96	27.32
t6_1F		0.9806	2.564	1.4521	2209	-4.9433	-4.6708	28.53	27.23
a_1F		1.0000	2.106	1.0000	650	-4.9218	-4.0851	31.34	23.93
b_1F	*	1.0000	2.317	1.0000	650	-4.6890	-4.4771	28.05	23.60
c_1F	*	1.0000	2.529	1.0000	650	-5.0780	-4.8363	27.35	23.29
d_1F	*	1.0000	2.741	1.0000	650	-5.6363	-5.1667	22.54	23.01
e_1F		1.0000	2.105	1.2000	650	-4.8109	-3.9526	31.75	24.41
f_1F	*	1.0000	2.316	1.2000	650	-4.5396	-4.3446	26.82	24.06
g_1F	*	1.0000	2.528	1.2000	650	-4.8115	-4.7041	28.01	23.75
h_1F	*	1.0000	2.740	1.2000	650	-5.2045	-5.0346	26.62	23.47
i_1F		1.0000	2.104	1.4000	650	-4.7301	-3.8402	32.93	24.81
j_1F	*	1.0000	2.315	1.4000	650	-4.4295	-4.2324	25.07	24.47
k_1F	*	1.0000	2.527	1.4000	650	-4.6010	-4.5920	28.45	24.15
l_1F	*	1.0000	2.738	1.4000	650	-5.1413	-4.9211	27.43	23.87

2.5 COMPARING WITH OTHER CODES

In the previous sections, we have given a description of our AGB wind hydrodynamics code. In the next chapters we study the influence of grain drift on the flow. This is done by performing the three kinds of calculations addressed in the previous section: single fluid calculations, two fluid calculations, and calculations in which equilibrium drift is imposed. However, before we can draw *any* conclusions from the differences between the calculations with and without drift, we should check whether the most basic version of the code (the code in single fluid mode) produces correct results. We do so by comparing our results with those from two other groups (Fleischer et al., 1992; Höfner & Dorfi, 1997). Note that our code is the first to combine self consistent (grain) chemistry with time dependent hydrodynamics allowing grain drift, so that no comparison of our code in two-fluid mode with previous results is possible.

The calculations by Fleischer et al. (1992) and Höfner & Dorfi (1997) are produced with codes that are comparable to our code in single fluid mode, the same physical processes are incorporated, but grain drift is not taken into account. In order to
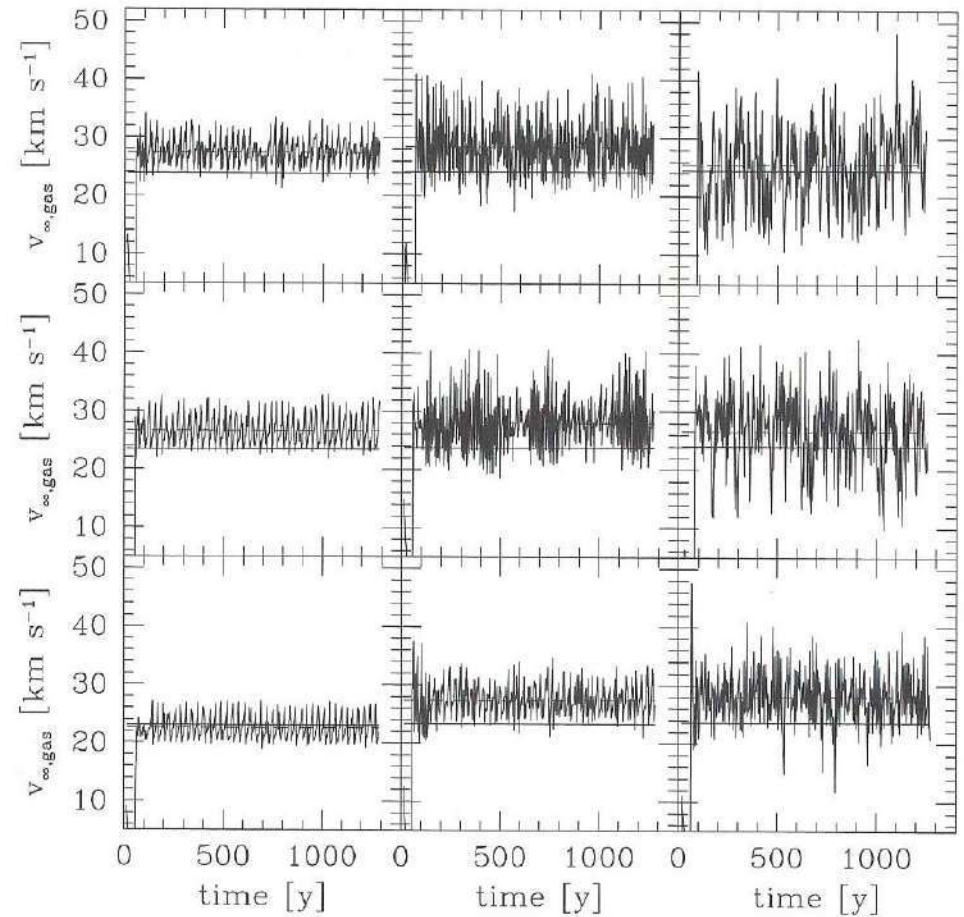
FIGURE 2.6: 'Terminal' velocity, or rather the velocity at 15 R_* of our single fluid models. Overplotted are the time averaged values of this velocity (dashed) and the velocity according to the Arndt approximation (full line).

compare their and our results, we make use of a relation, derived by Arndt et al. (1997), that relates the six parameters of the hydrodynamical AGB wind calculations to the resulting mass loss rate,

$$\log \dot{M}_{Arndt} = -4.95 - 9.45 \log \left(\frac{T[K]}{2600} \right) + 1.65 \log \left(\frac{L[L_\odot]}{1.0 \cdot 10^4} \right)$$
$$- 2.86 \log (M[M_\odot]) + 0.470 \log \left(\frac{\epsilon_C/\epsilon_O}{1.8} \right)$$
$$- 0.146 \log \left(\frac{P[d]}{650} \right) + 0.449 \log \left(\frac{\Delta v[\text{km s}^{-1}]}{2.0} \right) \quad (2.124)$$

T	2300	–	3000	K
L	5000	–	20000	$L_\odot$
M	0.6	–	2.0	$M_\odot$
ϵ_C/ϵ_O	1.3	–	2.2	
P	325	–	975	d
Δv	1.0	–	5.0	km s^{-1}

TABLE 2.2: The range of stellar parameters of the 48 models underlying Arndt et al.'s approximative equations.

model	$\dfrac{\langle \log \dot{M} \rangle - \log \dot{M}_A}{\langle \log \dot{M} \rangle}$	$\dfrac{\langle \log v_\infty \rangle - \log v_{\infty,A}}{\langle \log v_\infty \rangle}$
b_1F	4.519×10^{-2}	5.181×10^{-2}
c_1F	4.760×10^{-2}	4.857×10^{-2}
d_1F	8.331×10^{-2}	-6.625×10^{-3}
f_1F	4.296×10^{-2}	3.302×10^{-2}
g_1F	2.232×10^{-2}	4.951×10^{-2}
h_1F	3.264×10^{-2}	3.838×10^{-2}
j_1F	4.450×10^{-2}	7.519×10^{-3}
k_1F	1.956×10^{-3}	4.894×10^{-2}
l_1F	4.283×10^{-2}	4.198×10^{-2}

TABLE 2.3: Relative difference between the average mass loss rate and 'terminal' velocity from our models and those predicted by Arndt et al.'s approximative equations.

	$\log \dot{M}$	$\log v_\infty$
$\bar{e}_{FGS}$ [%]	2.4	2.3
$\bar{e}_{HD}$ [%]	5.0	3.3
$\bar{e}_{SID}$ [%]	4.0	3.5
r_{FGS}	0.954	0.956
r_{HD}	0.970	0.901
r_{SID}	0.961	0.355

TABLE 2.4: Average percentual difference and linear correlation coefficient between Arndt et al.'s approximations and the series of model calculations by Fleischer et al. (1992) (FGS), Höfner & Dorfi (1997) (HD) and our models (SID).

This relation was constructed as a fit to a grid of 48 dynamical models from Fleischer et al. (1992). In a similar way, Arndt et al. (1997) derived approximative equations for the velocity at the outer grid point (v_∞). The accuracy of the approximations was tested using a grid of 16 carbon-rich LPV dynamical models from Höfner & Dorfi (1997) and turned out to be good: the correlation coefficient between their sample and the approximation (Eq.(2.124)) is ≈ 0.97. Since both the results of Fleischer et al. and Höfner & Dorfi appear to be well correlated with the approximative equations, we can use these as a means to compare our and their results.

Table 2.1 gives an overview of the 20 single fluid calculations we have performed. Here, we will only consider the time averaged mass loss rate and outflow velocity. Other aspects of the models will be discussed in Chapter 4, where we will compare them with calculations including grain drift. Columns 2–4 of Table 2.1 give the stellar mass, temperature and luminosity and the period of the piston, which mimics stellar pulsation. The remaining input parameters, the carbon to oxygen abundance ratio and the amplitude of the piston were taken equal for all models: $\epsilon_C/\epsilon_O = 1.8$ and $\Delta v = 2.0$ km s^{-1}. Column 5 gives the time averaged mass loss rate at the outermost grid point

(which corresponds to 100 R_*). Note that time-averaging was necessary because the mass loss rate is not entirely constant as a function of time as a consequence of the stellar pulsation. The same is true for the outflow velocity (column 7). The outflow velocity as a function of time, its time averaged value, and the value according to the Arndt et al. models are plotted in Fig. 2.6. Because Fleischer et al. (1992) run their models out to only 15 R_*, we have, for the velocities given in Table 2.1, also determined the velocity at his distance. In columns 6 and 8 the mass loss rate and outflow velocity according to the Arndt approximation are given.

The range of stellar parameters of the 48 models on which Arndt et al. based their approximative equations is given in Table 2.2. One cannot expect a good correlation between mass loss rates and terminal velocities predicted by Arndt et al.'s equation and models with parameters outside the ranges given in Table 2.2. Thus, to get an indication for the reliability of our code, we only take into account the models with parameters in the ranges given in Table 2.2. These models are marked with an * in Table 2.1.

For those of our single fluid models with parameters within the range of validity of Arndt et al.'s approximations, the relative differences between the resulting mass loss rate and terminal velocity are listed in Table 2.3. Finally, to compare our model calculations with those by Fleischer et al. (1992) and Höfner & Dorfi (1997), we have calculated the average difference over all models (with parameters within the ranges listed in Table 2.2). Also linear correlation coefficients were calculated. For the model calculations by Fleischer et al. (1992) and Höfner & Dorfi (1997), these numbers were provided in Arndt et al.'s paper (1997). It turns out that the average relative differences between Arndt et al.'s approximations and our models are comparable to the differences with the Höfner & Dorfi (1997) models. For obvious reasons, the match between mass loss rate and velocity from the approximative equations and Fleischer's models is very good. Also the correlation between the mass loss rate resulting from our models and the approximations is strong and comparable to that of the Höfner & Dorfi models. The degree of correlation for the outflow velocity is not very high, however. This is mainly due to the models f_1F and j_1F. These models show a hint of a long term (few hundred year time scale) variability in the velocity at 15 R_*, see Fig. 2.6. Since the time-averaged 'terminal' velocity was determined by averaging over $\sim$ 1000 years, variability on this time scale hinders an accurate determination of the average velocity.

We conclude that our AGB wind code, in its basic (single fluid) form, agrees well enough with comparable codes to proceed with calculations including drift. These are the topic of the next two chapters.

3

ORIGIN OF QUASI-PERIODIC SHELLS IN DUST FORMING AGB WINDS

[1] We have combined time dependent hydrodynamics with a two-fluid model for dust driven AGB winds. Our calculations include self-consistent gas chemistry, grain formation and growth, and a new implementation of the viscous momentum transfer between grains and gas. This allows us to perform calculations in which no assumptions about the completeness of momentum coupling are made. We derive new expressions to treat time dependent and non-equilibrium drift in a hydrodynamics code. Using a stationary state calculation for IRC +10216 as initial model, the time dependent integration leads to a quasi-periodic mass loss in the case where dust drift is taken into account. The time scale of the variation is of the order of a few hundred years, which corresponds to the time scale needed to explain the shell structure of the envelope of IRC +10216 and other AGB and post-AGB stars, which has been a puzzle since its discovery. No such periodicity is observed in comparison models without drift between dust and gas.

3.1   INTRODUCTION

Dust driven winds are powered by a fascinating interplay of radiation, chemical reactions, stellar pulsations and dynamics. As soon as the envelope of a star on the Asymptotic Giant Branch (AGB) develops sites suitable for the formation of solid 'dust' (i.e. sites with a relatively high density and a low temperature) its dynamics will be dominated by radiation pressure. Dust grains are extremely sensitive to the stellar radiation and experience a large radiation pressure. The acquired momentum is partially transferred to the ambient gas by frequent collisions. The gas is then blown outward in a dense, slow wind that can reach high mass loss rates.

The detailed observations of (post) AGB objects and Planetary Nebulae (PN) that have become available during the last decade have shown that winds from late type stars are far from being smooth. The shell structures found around e.g. CRL 2688, the Egg Nebula, (Ney et al., 1975; Sahai et al., 1998), NGC 6543, the Cat's Eye Nebula, (Harrington & Borkowski, 1994) and the AGB star IRC +10216 (Mauron & Huggins, 1999, 2000), indicate that the outflow has quasi-periodic oscillations. The time scale for these oscillations is typically a few hundred years, i.e. too long to be a result of stellar pulsation, which has a period of a few hundred days, and too short to be due to

---

[1]The contents of this chapter overlap largely with Simis et al. (2001b)

thermal pulses, which occur once in ten thousand to hundred thousand years.

Stationary models, in which gas and dust move outward as a single fluid, do not suffice to explain the observations. Instead, time dependent two–fluid hydrodynamics, preferably including (grain) chemistry and radiative transfer, may help to explain the origin of these circumstellar structures.

Time dependent hydrodynamics has been used to study the influence of stellar pulsations on the outflow (Bowen, 1988; Fleischer et al., 1992). The coupled system of radiation hydrodynamics and time dependent dust formation was solved by Höfner et al. (1995).

Stationary calculations, focused on a realistic implementation of grain nucleation and growth, have been developed in the Berlin group, initially for carbon–rich objects (Gail et al., 1984; Gail & Sedlmayr, 1987) and more recently also for the more complicated case of silicates in circumstellar shells of M stars (Gail & Sedlmayr, 1999).

Two–fluid models, in which dust and gas are not necessarily co–moving, have been less well studied. Berruyer & Frisch (1983), Berruyer (1991) and MacGregor & Stencel (1992), pointed out that, for stationary and isothermal envelopes, the assumption of complete momentum coupling breaks down at large distances above the photosphere and for small grains. Self–consistent, but again stationary, two–fluid models, considering the grain size distribution, dust formation and the radiation field were developed by Krüger and co–workers (Krüger et al., 1994; Krüger & Sedlmayr, 1997).

The only studies in which time dependent hydrodynamics and two–fluid flow have been combined so far are the work of Mastrodemos et al. (1996) and that of the Potsdam group (Steffen et al., 1997; Steffen et al., 1998; Steffen & Schönberner, 2000).

In the next section, we will argue that time dependence and two–fluid flow are not just two interesting aspects of stellar outflow but that they have to be combined. It turns out that fully free two–fluid flow, i.e. in which no assumptions at all about the amount of momentum transfer between both phases are made, can only be achieved in time dependent calculations. In two–fluid flow, both phases are described by their own continuity and momentum equations. Momentum exchange occurs through viscous drag, i.e. through gas–grain collisions. The collision rate and the momentum exchange per collision depend on the velocity of grains relative to the gas. Hence, by fixing the drag force, one fixes the relative velocity and the system becomes degenerate.

In this paper we present our two–fluid time dependent hydrodynamics code. We have selfconsistently included equilibrium gas chemistry and grain nucleation and growth, see Section 3.3. In order not to make assumptions on the viscous coupling, we consider, in Section 3.3.4, the microphysics of gas–grain collisions. Results are given in Section 3.4.

3.2   GRAIN DRIFT AND MOMENTUM COUPLING

3.2.1   DEFINITIONS

The acceleration of dust grains, as a result of radiation pressure, leads to an increase in the gas–dust collision rate. The viscous drag force (the rate of momentum transfer from grains to gas due to these collisions) is proportional to the collision rate and to the relative velocity of grains with respect to the gas. This force is discussed in the

next section in more detail. The drag force provides a (momentum) coupling between the gaseous and the solid phase[2].

The gas–dust coupling was studied by e.g. Gilman (1972), who distinguished two types of coupling. Gas and grains are *position coupled* when the difference in their flow velocities, the drift velocity, is small compared to the gas velocity, i.e. when the grains move slowly through the gas. *Momentum coupling*, on the other hand, requires that the momentum acquired by the grains through radiation pressure is approximately equal to the momentum transferred from the grains to the gas by collisions. The situation in which both are exactly equal is called *full* or *complete* momentum coupling. Gilman (1972) stated that, if both forces are equal, grains drift at the *terminal* drift velocity. A less confusing term for the same situation was introduced by Dominik (1992): *equilibrium drift*. The idea is that since the drag force increases with increasing drift velocity, an equilibrium value can be found by equating the radiative acceleration of the grains and the deceleration due to momentum transfer to the gas. Note that, when calculating the equilibrium value of the drift velocity that way, i.e. assuming complete momentum coupling, one implicitly assumes that grains are massless. A physically correct way to calculate the equilibrium drift velocity is to demand gas and grains to have the same acceleration.

3.2.2   SINGLE AND MULTI–FLUID MODELS

Various groups have studied the validity of momentum coupling, with and without assuming equilibrium drift, in stationary and in time dependent calculations. Others have just applied a certain degree of momentum coupling in model calculations carried out to study other aspects of the wind. We will give a brief overview of the most important of these studies, resulting in the conclusion that prior to our attempt, full two–fluid hydrodynamics has been presented only twice. Because the meaning of terms like 'full' and 'complete' momentum coupling, 'terminal' and 'equilibrium' drift seem to be slightly different from author to author, we will first give our own definitions for three classes of models.

First, *single–fluid* models are those in which only the momentum equation of the gas component is solved. All momentum due to radiation pressure on grains is transferred fully and instantaneously to the gas. If, e.g., for the calculation of grain nucleation and growth rates, a value for the flow velocity of the dust component is needed, the dust is just assumed to have the same velocity as the gas: drift is assumed to be negligible. Hence, in terms of Gilman (1972), in single fluid models grains are both position and (completely) momentum coupled to the gas.

The second class is that of the *two–fluid* models. Here, again in terms of Gilman (1972), grains are not necessarily position and momentum coupled to the gas. Grains can drift at non–equilibrium drift velocities. Hence, grains and gas are neither forced to have equal velocity nor forced to have equal acceleration.

The third category of models represents what we will call *1.5–fluid* models. In these

---

[2]Another momentum coupling is due to the fact that momentum is removed from the gas phase when molecules condense on dust grains. The amount of momentum involved in this coupling is also taken into account in our numerical models but is many orders of magnitude smaller than the collisional coupling.

models, grains are assumed to drift at the equilibrium drift velocity with respect to the gas. No assumptions about position coupling are made. In other words, gas and grains are equally accelerated but do not necessarily have the same velocity. The equilibrium drift velocity is calculated by equating the drag force and the radiation pressure on the grains, see Dominik (1992), or, more accurately, by demanding gas and grains to be equally accelerated. Only the momentum equation of the gas is solved, the dust velocity is determined by simply adding the gas velocity and the equilibrium drift velocity.

3.2.3 STATIONARY MODELS

Although the above classification for modelling methods also applies to stationary models, extra care is needed there. When trying to do two–fluid stationary modelling one should realize that the condition of stationarity *itself* will also introduce momentum coupling. This can be understood as follows. Equilibrium drift is the state in which gas and grains are equally accelerated:

$$\frac{dv_{\mathrm{g}}}{dt} = \frac{dv_{\mathrm{d}}}{dt} \tag{3.1}$$

The derivative in this equation is a total derivative. Imposing stationarity, the temporal contribution to this total derivative vanishes by definition, and Eq.(3.1) reduces to

$$v_{\mathrm{g}}\frac{\partial v_{\mathrm{g}}}{\partial r} = v_{\mathrm{d}}\frac{\partial v_{\mathrm{d}}}{\partial r} \tag{3.2}$$

The difference between both sides of Eq.(3.2) can be small, especially in the outer layers of the envelope, where the velocities reach a more or less constant value. Therefore, the occurrence of equilibrium drift in a stationary outflow may be partially due to the condition of stationarity itself. For this reason, one should be very careful when checking the validity of momentum coupling against stationary calculations. Moreover, in order to make a calculation fully self–consistent, no assumptions on momentum coupling should be made. Hence, for fully self–consistent modelling, time dependent calculations are to be preferred.

3.2.4 OVERVIEW OF PREVIOUS MODELLING

Examples of single fluid calculations are naturally found in studies in which drift and momentum coupling are not the topic of research, e.g. the work of Dorfi & Höfner (1991) and Fleischer et al. (1995). Both perform time dependent hydrodynamics, assuming that the influence of drift on the aspect of the flow under consideration, dust formation and nonlinear effects due to dust opacity, is negligible.

The completeness of momentum coupling is investigated by Berruyer & Frisch (1983) and by Krüger et al. (1994). The former first find a (stationary) wind solution under the assumption of complete momentum coupling, noticing that this assumption causes the two–fluid character to be lost. Next, in order to check the validity of their supposition, they find a stationary solution for the system, including the grain momentum equation. Both calculations give very similar results near the photosphere, from which it is concluded that momentum coupling is complete there. Far away from the stellar surface ($\gtrsim 1000R_*$), the results are different so that momentum coupling is said

to be invalid there. We too, find that non–equilibrium drift arises far away from the photosphere (see Section 3.4). We would like to remark, however, that it may not be sufficient to verify the validity of complete momentum coupling by comparing with stationary calculations, see Section 3.2.3.

Krüger et al. (1994) undertook a similar study, which is the most realistic stationary two–fluid calculation up to now. It treats the coupled system of hydrodynamics and thermodynamics, but also involves chemistry and dust formation (simplified by the assumption of instantaneous grain formation). Krüger et al. conclude that momentum coupling can be assumed to be complete and therefore disagree with Berruyer & Frisch (1983). We think this may be due to the fact that Krüger et al. run their calculation out to about ten stellar radii, whereas Berruyer & Frisch compute outwards to several thousand stellar radii.

According to MacGregor & Stencel (1992), who use a simple model for grain growth in a stationary, isothermal atmosphere, the assumption of complete momentum coupling appears to break down for grain sizes smaller than about 5×10^{-6} cm.

Prior to our attempt, time dependent two–fluid hydrodynamics was presented by Mastrodemos et al. (1996). They conclude that fluctuations on the time scale of the variability periods of Miras and LPV (Long Period Variables), 200-2000 days, can not persist in the wind. Since they do not calculate grain nucleation and growth self–consistently but instead assume that grains grow instantaneously and have a fixed size, the extreme non–linear coupling between shell dynamics, chemistry and radiative transfer (cf. Sedlmayr & Winters (1997)) is not present. Our calculations however indicate that this chemo–dynamical coupling is a main ingredient to the occurrence of variability in the wind.

Steffen and co–workers (Steffen et al., 1997; Steffen et al., 1998; Steffen & Schönberner, 2000) have a more or less similar approach: their models are based on time dependent, two–fluid radiation hydrodynamics and grains have a fixed size. Main emphasis is on the long term variations of stellar parameters ($L_*(t)$, $\dot{M}(t)$), due to the thermal pulses, which are included as a time dependent inner boundary. It turns out that these large–amplitude variability at the inner boundary is not damped in the envelope and remains visible in the outflow as a pronounced shell.

The calculations presented in this paper aim at combining time dependent hydrodynamics with a two–fluid model and are suitable for calculating the stellar wind from the subsonic photosphere to the supersonic outer layers at large distances. We will not take stellar pulsation into account because we want to find out if the envelope itself possesses characteristic time scales. The main goal of this work is to get insight in the physical processes underlying the observed time dependent structures around AGB stars. We do not aim at exactly reproducing certain observational results and hence will not adjust the stellar parameters in order to provide a better fit.

3.3 MODELLING METHOD

3.3.1 BASIC EQUATIONS

The basic equations for the time dependent description of a stellar wind in spherical coordinates and symmetry, are the continuity equations,

$$\frac{\partial \rho_{g,d}}{\partial t} + \frac{1}{r^2}\frac{\partial}{\partial r}(r^2 \rho_{g,d} v_{g,d}) = s_{cond,g,d} \tag{3.3}$$

and the momentum equations,

$$\frac{\partial}{\partial t}(\rho_g v_g) + \frac{1}{r^2}\frac{\partial}{\partial r}(r^2 \rho_g v_g^2) =$$
$$- \frac{\partial P}{\partial r} + f_{drag,g} - f_{grav,g} + v_g s_{cond,g} \tag{3.4}$$

$$\frac{\partial}{\partial t}(\rho_d v_d) + \frac{1}{r^2}\frac{\partial}{\partial r}(r^2 \rho_d v_d^2) =$$
$$f_{rad} + f_{drag,d} - f_{grav,d} - v_g s_{cond,g} \tag{3.5}$$

These equations form a system in which both gas and dust are described by their own set of hydrodynamics equations (two–fluid hydrodynamics). The equations are coupled via the source terms. The source term in Eq.(3.3) represents the condensation of dust from the gas, including nucleation and growth. Since mass is conserved we have

$$s_{cond,g} = -s_{cond,d} \tag{3.6}$$

The gas condensation source term is negative due to nucleation and/or growth of grains. Atoms and molecules that condense onto grains take away momentum from the gas. This is accounted for in the $v_g s_{cond,g}$ source terms in the momentum equations.

The momentum equations also couple via the viscous drag force of radiatively accelerated dust grains on the gas. Since no momentum is lost, we have

$$f_{drag,g} = -f_{drag,d} \tag{3.7}$$

The drag force is proportional to the rate of gas–grain collisions and the momentum exchange per collision and is therefore of the form

$$f_{drag} = \Sigma_d n_g n_d m_g |v_D| v_D \tag{3.8}$$

where Σ_d is the collisional cross section of a dust grain and v_D is the drift velocity of the grains with respect to the gas.

We assume a grey dust opacity and take the extinction cross section of the grains equal to the geometrical cross section. Then the radiative force is simply

$$f_{rad} = \frac{L_* \Sigma_d n_d}{4\pi r^2 c} \tag{3.9}$$

Radiation pressure on gas molecules is negligible in the circumstellar environment of AGB stars. In order to determine the temperature structure of the envelope, a balance

equation for the energy can be added. We do not involve the energy structure in the time dependent calculation. Also, we do not solve radiation transport. Instead, we assume that, throughout the envelope, the temperature stratification is determined by radiation equilibrium of the gas. This assumption is justified as long as the envelope is optically thin to the cooling radiation emitted by the dust. The inclusion of an energy equation poses no problems, if one wants to spend the computer time.

The model is completed with the equation of state for ideal gases.

3.3.2 GAS CHEMISTRY

Our hydrodynamics code contains an equilibrium chemistry module (Dominik, 1992) which includes H, H_2, C, C_2, C_2H, C_2H_2 and CO, and hence is suitable for modelling C stars.

Oxygen has completely associated with carbon to form CO. Due to the high bond energy of the CO molecule (11.1 eV), this molecule is the first to form. In absence of dissociating UV radiation, CO–formation is irreversible. Hence if $\epsilon_C > \epsilon_O$ at the time of CO formation, all oxygen will be captured in CO and carbon will be available for the formation of molecules and dust. Given the total number density of H and C atoms in the gas phase, the dissociation equilibrium calculation is carried out in each numerical time step to give the densities of the molecules mentioned. Therefore, bookkeeping of the H and C number densities is needed. This requires two additional continuity equations of the form of Eq.(3.3).

3.3.3 GRAIN NUCLEATION AND GROWTH

Once the abundances of the gas molecules are known, the nucleation and growth of dust grains can be calculated. We use the moment method (Gail et al., 1984; Gail & Sedlmayr, 1988), in conservation form (Dorfi & Höfner, 1991). The resulting nucleation and growth rates are used to calculate the source terms of Eq.(3.3) and the additional continuity equations for hydrogen and carbon. The moment equations provide the evolution in time of the zeroth to third moment of the grain size distribution function. Hence, amongst others, the number density and the average grain size are known as a function of time. We could, in principle, calculate the full grain size spectrum, using the moment method, but we limit ourselves to the use of average grain sizes. The main advantage of this is that we can apply two–fluid, instead of multi–fluid hydrodynamics, which is obviously computationally cheaper.

3.3.4 VISCOUS GAS–GRAIN MOMENTUM COUPLING

In the absence of grain drift, gas and dust particles will collide frequently due to the thermal motion of the gas, but no net momentum transfer from one state to the other will take place since the collisions are random. If grains are radiatively accelerated with respect to the gas, both the thermal motion and the acceleration give rise to gas–grain encounters, resulting in a net momentum transfer from grains to gas. The resulting viscous drag force is described in e.g. Schaaf (1963).

In the hydrodynamical regime, the time scale on which individual gas–grain collisions occur is many orders of magnitude smaller than the dynamical time scale. Hence,

in order to calculate the momentum transfer from grains to gas, one needs to sum over many collisional events. The strong dependence of the momentum source term on the (drift) velocity, via the drag force (Eq.(3.8)), enables rapid changes in the velocities. When applying an explicit numerical difference scheme, as we do, it will therefore be necessary to take small numerical time steps. Taking small, and hence more, time steps involves the risk of losing accuracy however. In our case, the drag force makes the system so stiff that this would lead to unacceptably small numerical time steps: a reduction of a factor thousand or more, compared to the Courant time step is not unusual. To avoid having to take such small steps we perform a kind of subgrid calculation for the drift velocity by studying the microdynamics of the gas–grain system. Doing so, we derive an expression for the temporal evolution of the drift velocity during one numerical time step. This expression is then used to calculate an accurate value of the momentum transfer, i.e. the integrated drag force, in one numerical time step. This way, the momentum transfer rate is determined without making assumptions about the value of the drift velocity at the end of the numerical time step. Hence, if the momentum transfer is determined in this manner a full two-fluid calculation can be done. Details of the derivation are given in Section 2.2.4.

Another way to go around the problem of course would be to assume that the grains always drift at their equilibrium drift velocity and to perform a '1.5 fluid' calculation. It turns out, however, to be difficult to determine whether or not the assumption of equilibrium drift is justified, c.f. Section 3.2.3. For a discussion about the comparison of two–fluid and '1.5 fluid' calculations see Section 2.2.4

3.4   NUMERICAL CALCULATIONS

3.4.1   NUMERICAL METHOD

The continuity and momentum equations are solved using an explicit scheme. A hydrodynamics code was specially written for this purpose. It uses centered differencing and a two–step, predictor–corrector scheme, applying Flux Corrected Transport (FCT) (Boris, 1976). Second order accuracy is achieved for the single fluid and momentum coupled ('1.5 fluid') calculations. In the two fluid computation we applied, whenever needed, Local Curvature Diminishing (LCD) (Icke, 1991), at the risk of introducing first order behaviour.

3.4.2   INITIAL AND BOUNDARY CONDITIONS, GRID

As an initial model for the calculation, a stationary profile for IRC +10216, kindly provided by J.M. Winters (Winters et al., 1994), was used, see Fig. 3.1.

Stellar parameters of this model are: $M_* = 0.7 M_\odot$, $L_* = 2.4 \cdot 10^4 L_\odot$, $T_* = 2010K$ and a carbon to oxygen ratio $\epsilon_C/\epsilon_O = 1.40$. The corresponding stellar radius is $R_* = 9.20 \cdot 10^{13}$cm, $R_{max} = 200 R_*$. The mass loss rate for the initial model is $\dot{M} = 8 \cdot 10^{-5} M_\odot yr^{-1}$. In order to compare our calculations with observations, we extend the computational grid to 1287 R_*. Because no initial data is known for the grid extension, we simply set the initial values for $r > 200 R_*$ of all flow variables equal to their value
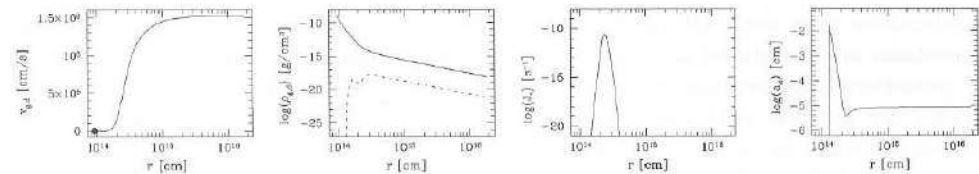
FIGURE 3.1: Velocity (no drift), gas and dust density, nucleation rate and average grain radius for the initial profile.

at $r = 200 R_*$. As a consequence of this, a transient solution will have to move out of the grid before the physically correct solution can settle.

Grid cells are not equally spaced, since a high resolution is desirable in the subsonic area but not necessary in the outer envelope. The grid cells are distributed according to:

$$\frac{r[n] - r[n-1]}{r[1] - r[0]} = q^{n-1/n_{max}-1} \tag{3.10}$$

The number of cells in the grid, n_{max}, used here is 737 and the size ratio q between the innermost and the outermost cell is 318.

One of the most important aspects of a numerical hydrodynamics calculation is the treatment of the inner boundary. Since the (long time averaged) mass fluxes through the inner and the outer boundary must be equal, setting the inner boundary essentially means fixing the mass loss rate. We have, in our calculations, fixed the density and velocity in the innermost grid cells, so that the *advective* mass and momentum fluxes (i.e. the first order derivatives of the flow variables) through the inner boundary are constant. Note that the temperature was constant as a function of time as well so that also the pressure will be fixed. In reality, however, velocity and density will vary with time. To account for a variable inflow of mass into the envelope, we permit also *diffusive* inflow of mass. This flow depends upon second order derivatives near the inner boundary and therefore models quite realistically the cause of matter inflow into the envelope. At the inner boundary, the main driving term of the wind is not yet active and the velocities are very small because newly formed small grains, which are very sensitive to radiation pressure, are formed farther out. Therefore, the oscillations of the envelope are clearly not caused by the implementation of the inner boundary.

To model the diffusive flux at the inner boundary, we could have introduced a separate diffusion term. There is no need to do so, however, since our numerical scheme involves the calculation of a diffusion term already. This diffusion term (*numerical viscosity*) is part of our finite difference scheme and it is locally (i.e. at extrema) required to stabilize the centered differencing method. Whenever numerical viscosity is not strictly needed to stabilize the numerical scheme it will be cancelled by an anti-diffusion term (Boris, 1976). A detailed description of this method is beyond the scope of this paper, for details the reader is referred to Icke (1991). We want to allow for diffusion at the inner boundary. Instead of adding explicitly a diffusion term we can simply somewhat reduce the anti-diffusion at the inner boundary. That way, not all of the numerical diffusion is cancelled and effectively a diffusive flux is created at the inner boundary.

Although important for the AGB evolution, no stellar pulsations or time dependent

luminosities were used. Often, in hydrodynamical simulations of late type stars, stellar pulsations are introduced as a time dependent inner boundary condition. In the absence of pulsations, the average grain near the inner boundary will be large. Since larger grains are less efficiently accelerated by the radiative force than smaller ones, the stationary inner boundary condition will lead to small velocities in the lower envelope. As a result of the inefficient radiative force on large grains, these grains will also tend to drift at high or even non–equilibrium drift speeds. To avoid this unwanted behaviour, equilibrium drift is imposed in the first 2.8 R_*, also in the two–fluid calculation.

3.4.3 CALCULATIONS

In order to determine the effect of grain drift on the outflow, we perform three types of calculation. First, we solve the full two–fluid system including gas chemistry, grain formation and growth and the continuity and momentum equation for both gas and grains. The viscous momentum transfer during each numerical time step is calculated by integration of f_{drag} over this time step as was presented in Section 3.3.4. Division by the duration of the time step gives an expression for f_{drag} that can be inserted in the momentum equations, Eqs.(3.4,3.5). When solving, the left hand side of these equations is multiplied by the time step again, so that indeed the correct amount of momentum is transferred.

Next, a 1.5–fluid calculation is performed. Here, the drag force is calculated by assuming equilibrium drift in Eq.(3.8). The dust velocity is taken to be the sum of the gas velocity and equilibrium drift velocity, according to Eq.(2.123). The momentum equation of the dust is not solved.

Finally, we also perform a single fluid calculation. Here too, only the gas momentum equation is solved. The drag force exerted on the gas is taken to be equal to the radiation force on the grains. Now, the velocity of the grains is simply set equal to the gas velocity. From the 1.5 and single fluid calculations, we expect to learn about the influence of (non–equilibrium) drift on the flow, when comparing them to the two fluid calculation.

All three models were evolved 10^6 numerical time steps, which amounts to $9.71 \cdot 10^{10}$, $1.67 \cdot 10^{11}$ or $3.14 \cdot 10^{11}$ seconds, depending on the model.

3.4.4 RESULTS

Fig. 3.2 shows the mass loss rate at $R = 100$, 500 and 1000 R_* as a function of time for the three calculations. The first 150 years of output in the 500 R_* plot and the first 800 years in the 1000 R_* plot show the passing of the transient solution. This is a result of extending the grid from 200 R_* in the initial profile to 1287 R_* in the calculation, the flow needs some time to reach the additional grid points.

Both the 1.5 and the two–fluid model show quasi–periodic oscillations. From plots which cover a longer time interval (not shown here) we infer that the variations in the mass loss rate in the single fluid calculation behave quasi–periodically as well, on a time scale of a few thousand years. An immediate conclusion from this is, that the presence of grain drift is important for variations of the mass loss rate.
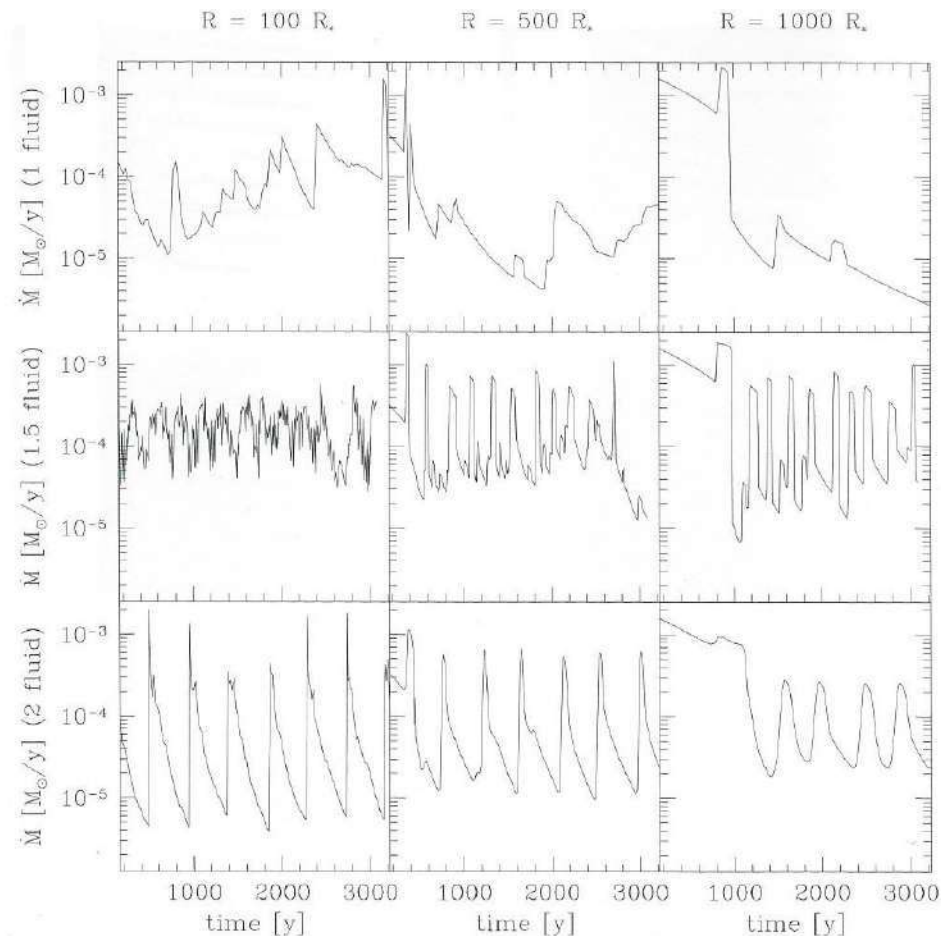
FIGURE 3.2: From top to bottom: Mass loss rates for single fluid (no drift, gas and grain have equal velocity, 'position coupling'), 1.5–fluid (equilibrium drift, gas and grains have equal acceleration, 'momentum coupling') and two–fluid (no assumptions on drift, no coupling imposed) calculations, for R = 100, 500 and 1000 R_*. Note that the first 150 years of output in the 500 R_* plot and the first 800 years in the 1000 R_* plot show the passing of the transient solution due to the extension for the calculational grid w.r.t. the initial model.

The time between two peaks in the mass loss is approximately 200 to 350 years for the 1.5–fluid model, and about 400 years for the two–fluid model. Both numbers lie nicely in the range of the separation of 200–800 years between the shells that Mauron & Huggins (1999) observed in IRC +10216.

In all three calculations we see that the short time variations that are present at 100 R_*, have disappeared far away from the star. Mauron & Huggins (2000) note that this "wide range of shell spacing, corresponding to time scales as short as 40 yr (close to the star) and as long as 800 yr", should be accounted for in a consistent model. This poses
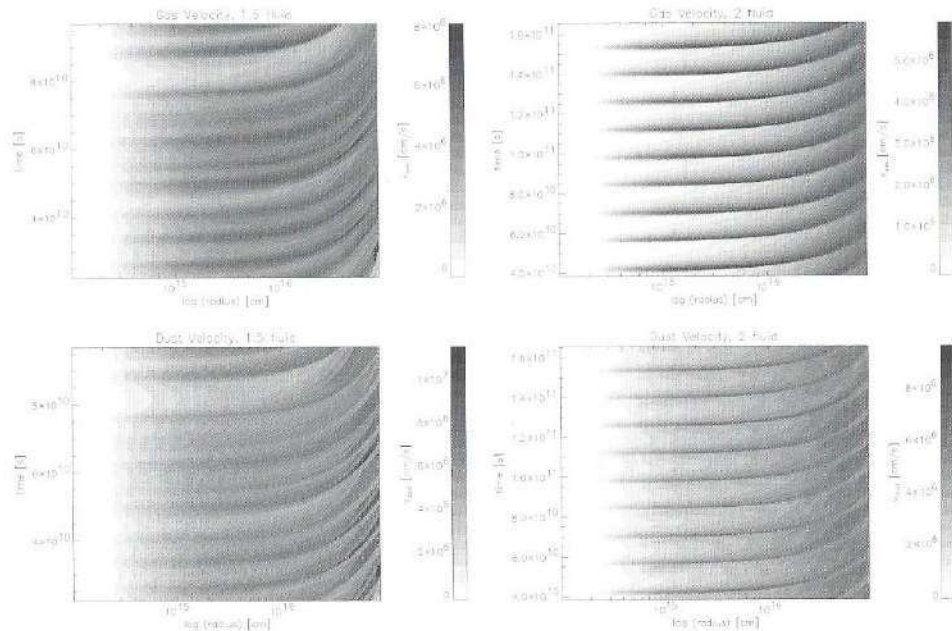
FIGURE 3.3: Gas and dust velocities as a function of radius and time for the 1.5 and the two–fluid model.

FIGURE 3.4: Gas and dust densities as a function of radius and time for the 1.5 and the two–fluid model.

no problems, since the disappearance of the smaller scale structures is simply due to dispersion and hence will appear in any flow in which perturbations do not propagate with exactly the same speed.

The fact that the two–fluid calculation shows less variations on short times scales than the 1.5–fluid model may be due to the more first order character of the former (as a result of the LCD term, see Section 3.4.1). We shall see that in the two–fluid calculation, in large parts of the envelope, grains move at their equilibrium drift velocity.

The time averaged mass loss rate, estimated from Fig. 3.2, lies around $\dot{M} = 1 \cdot 10^{-4} M_\odot \mathrm{yr}^{-1}$. The fact that this is somewhat higher than the mass loss rate of the initial model indicates that indeed the diffusive flux at the inner boundary has contributed, see Section 3.4.2. Our limited implementation of the radiative force (we use a grey dust opacity and take the extinction cross section of the grains equal to the geometrical cross section) causes the velocities in our calculation to be higher than the velocities in the initial model. Using a lower value for the stellar luminosity (e.g. using the core mass–luminosity relation) has proven to immediately lower the outflow velocity and hence the mass loss rate.

Figures 3.3 and 3.4 show, for the 1.5 and the two–fluid model, the gas and dust velocities and densities, as a function of radius and time. Throughout the whole grid, the fluctuations occurring in the two–fluid calculation are more regular that those in the 1.5–fluid model. The velocities of gas and dust in the momentum coupled calculation reach values that are up to 25% higher than in the two–fluid calculation. In the latter, matter is less accelerated than in the former, especially for radii larger than about
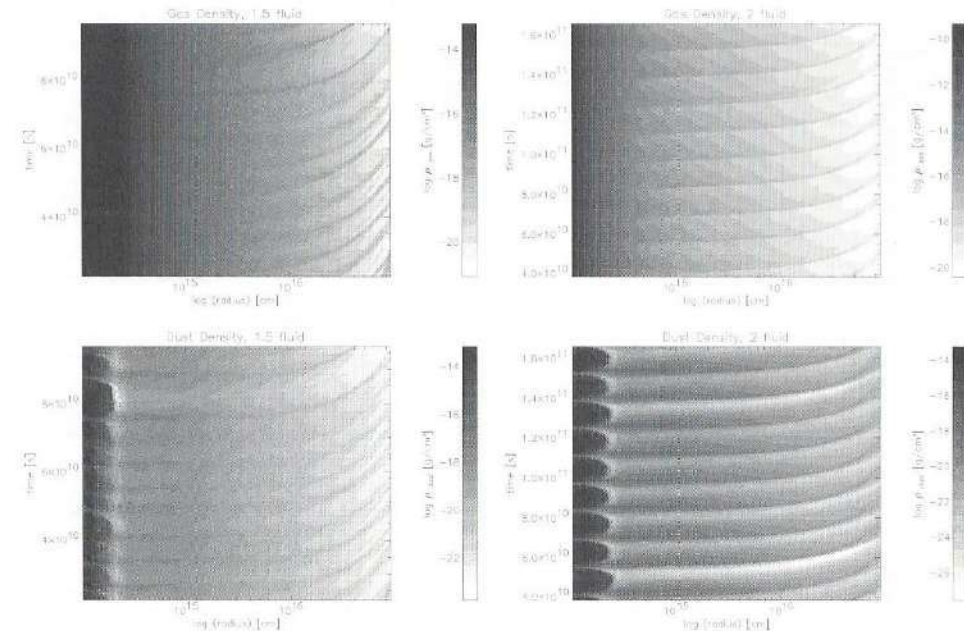
$2 \cdot 10^{16}$ cm. Probably, this is a result of non–equilibrium drift, which starts to appear around this radius (see Fig. 3.6). Non–equilibrium drift occurs when the time needed by a grain to reach its equilibrium drift velocity is long compared to the dynamical time scale. During a period of non–equilibrium drift, the gas is not being maximally accelerated and both gas and dust velocities will be lower than in a phase of equilibrium drift.

The gas density structure (Fig. 3.4) for the 1.5–fluid and the two–fluid calculation look similar. The main difference is that short time scale variations are present in the lower regions of the former, whereas large scale effects dominate the latter. The density structure plots for the dust show another difference: the perturbations in the 1.5–fluid flow appear as local increments of the density but in the two component flow the variations rather look like dips in the average profile. Maximum outflow density for gas and grains are in phase in the two–fluid model though, the 'dust pulse' is significantly broader than but centered around the maximum in the gas outflow. This is not just the case in the upper parts of the envelope, where non–equilibrium drift is present, but also for smaller radii.

In Figs. 3.5 and 3.6 we plot a series of snapshots, displaying the evolution of various flow variables during one instability cycle for the 1.5 and the two–fluid model. For the 1.5–fluid calculation the drift velocity is, by definition, always equal to its equilibrium value, which shows a time dependent behaviour. In the two–fluid flow we find that the drift velocity, out to approximately 10^{16} cm, equals the equilibrium value. At larger radii, small deviations from equilibrium drift are detected.
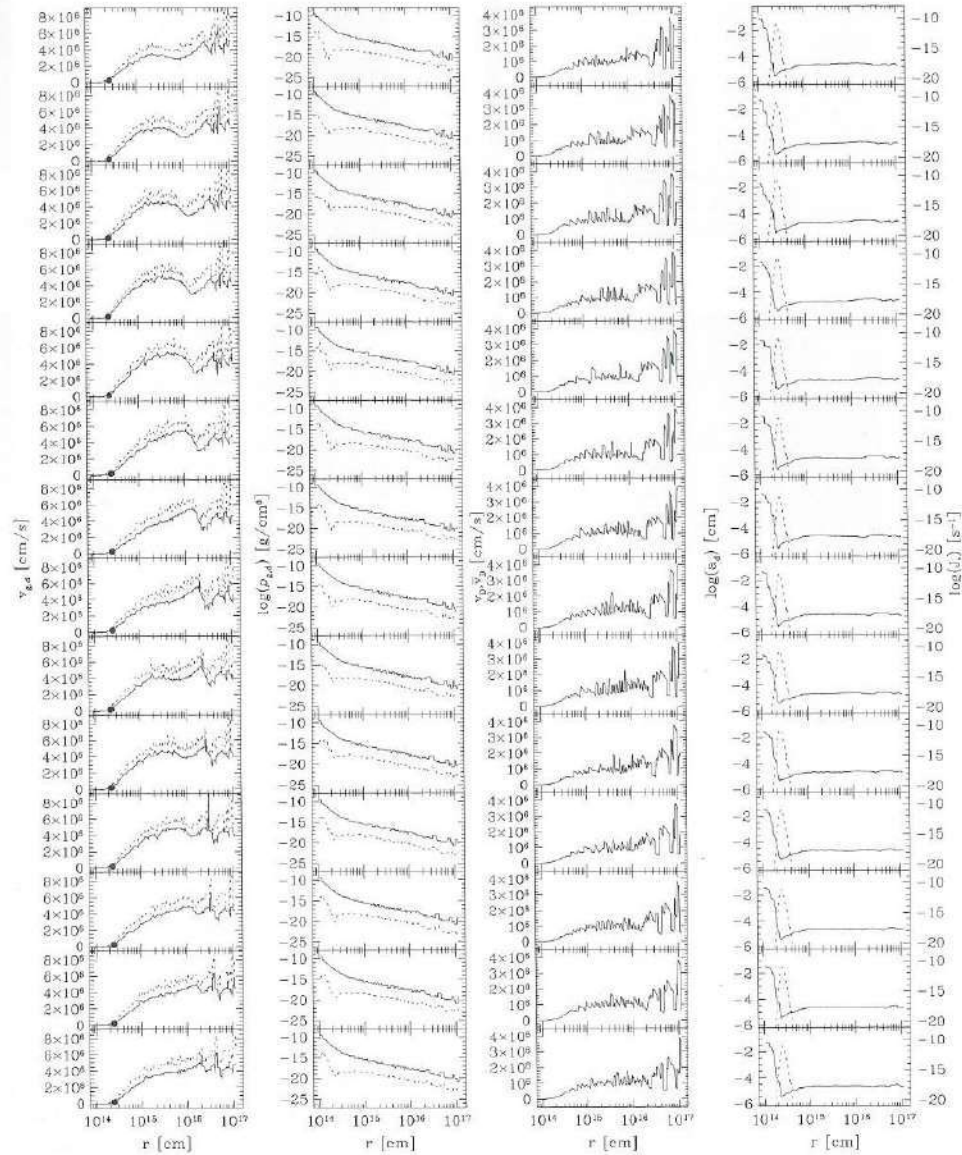
FIGURE 3.5: 1.5–fluid model. First column: gas and dust velocity (dashed line). The dot denotes the location of the critical point. Second column: gas and dust density (dashed line). Third column: drift velocity. Fourth column: average grain radius and grain nucleation rate (dashed line). The frames show (from top to bottom) the flow profile at 0, 30, 56, 81, 105, 132, 164, 197, 225, 252, 280, 310, 352 and 404 years after the first frame.
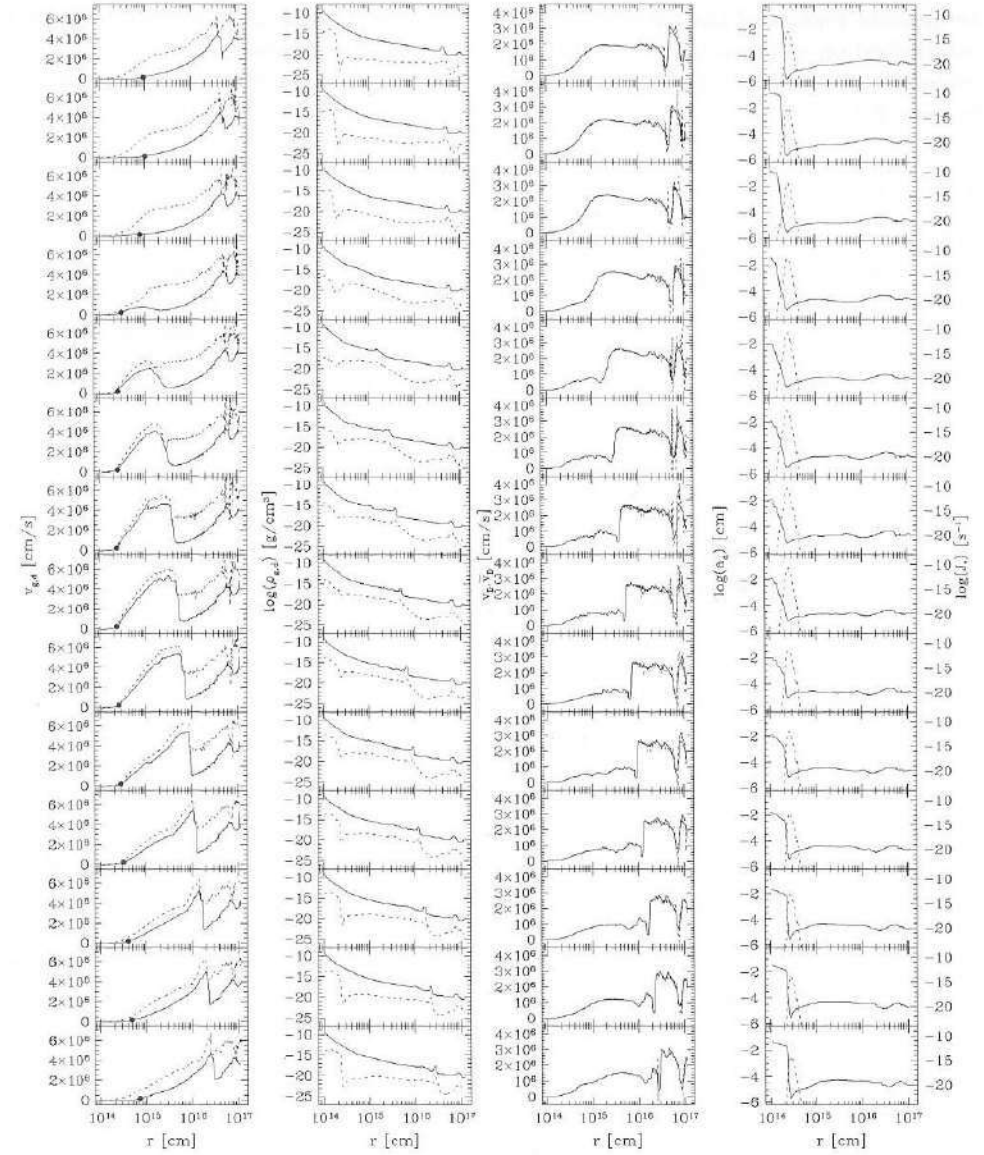
FIGURE 3.6: Two–fluid model. First column: gas and dust velocity (dashed line). The dot denotes the location of the critical point. Second column: gas and dust density (dashed line). Third column: drift velocity (dashed line) and equilibrium drift velocity (full line). Fourth column: average grain radius and grain nucleation rate (dashed line). The frames show (from top to bottom) the flow profile at 0, 32, 63, 93, 116, 131, 144, 156, 170, 189, 214, 245, 284 and 330 years after the first frame.

We want to stress that the fact that we see equilibrium drift in the lower and intermediate regions of the two component model *only* implies that equilibrium drift is established on a time scale shorter than the dynamical time scale. It does *not* however exclude the possibility that non–equilibrium drift occurs on shorter time scales, see Section 2.2.4.

3.4.5 THE ORIGIN OF THE MASS LOSS VARIABILITY

To investigate what causes the variability we will step through the frames of Fig. 3.6 for the two–fluid calculation. Thereafter, we will discuss the differences with the 1.5 fluid model. The mass loss rate of a stellar wind is determined in the subsonic region (see e.g. Lamers & Cassinelli (1999)), therefore in the following, when investigating the mechanism underlying the variability, we focus on this region, unless explicitly mentioned.

In Fig. 3.6 (frames 1–3) we see that the onset of the mass loss variability is the situation in which the dust has a velocity that is significantly higher than the gas velocity. This means that the residence time of a grain in the parts of the envelope where grains can grow is relatively short so that the average grain size is small. The smaller the grain, the more efficient radiation pressure will be, since small grains have a large surface to mass ratio and since we have assumed that the grain extinction cross section equals the geometrical cross section. Hence, radiative acceleration of grains is efficient and the velocity of the small grains increases further. Because position coupling is not imposed, the gas velocity can stay low and the drift velocity increases. We refer to this phase as the 'slow phase' of the variability cycle, because of the low gas velocity. Because the average grain radius is small, the grain acceleration becomes more efficient, the dust velocity grows, grains become smaller, and so forth. On their way out, the small grains concentrate in a narrowing shell, since the decrease of the average grain radius in time coincides with an increase of their velocity.

The smaller the grains, the longer their mean free path. As a consequence of the increasing drift velocity, this does not necessarily lead to a longer time interval between two subsequent collisions of a dust grain with gas molecules. Also due to the increasing drift velocity, the amount of momentum transfer from dust to gas per collision becomes larger. Hence, there exists a certain critical value of the drift velocity for which the momentum transfer from grains to gas becomes efficient. This sudden increase of the drag force leads to an immediate acceleration of the gas (frame 4). This results in an increase of the gas density and hence a further increase of drag force, since the mean free path for gas-dust collisions becomes shorter.

The transfer of momentum from grains to gas is now very efficient, so that both gas and grains move out with high velocities (frames 5–8). The normal, Parker–type, stellar wind profile is now visible. We refer to this phase as the 'fast phase' (frame 5–9). During this phase, the drift velocity is relatively small, so that the residence time of the grains in the region suitable for effective grain growth is relatively long. Hence, the grains tend to be large during the fast phase.

Because the transition from the phase of high drift and low gas velocities to the phase of low drift and high gas velocities took place very rapidly, a shock has formed and the gas develops a shell. Though not very clear from the figure, a rarefaction wave

moves in the opposite direction, at the same time. This leads to a gradual decrease of the gas density, and therefore of the number densities of the condensible species, below the sonic point. Although the density decrease is not so large, the impact on the drag force is considerable. This is because it is affected by the decreasing density in two ways. First, the decrease in the density directly leads to a decrease in the rate of gas-grain collisions. Second, it leads to a decrease in the average grain size. This also results in a longer mean free path and hence a lower drag force.

So, the passing of the rarefaction wave is immediately visible in the decrease of the average grain radius (frames 9–14). This illustrates the enormous sensitivity of the dust chemical processes to the densities.

Moreover, the rarefaction wave has triggered the slow phase again. This brings us back to the situation in the first frame.

Crucial in the process of shell formation as described above are the two 'turn–around' points. At the end of the slow phase, the drag force suddenly becomes effective because of its quadratic dependence on the drift velocity. This marks the onset of the fast phase. The sudden increase of the momentum transfer rate leads to the development of a shock. The rarefaction wave that arises simultaneously eventually triggers the end of the fast phase and the start of the next slow phase. A schematic representation of the variability mechanism is given in Fig. 1.5.

In the absence of grain drift, changes in the effectiveness of the drag force would be absent. The behaviour of the system during the slow phase is dominated by the existence of drift. This immediately explains why variability in the mass loss rate in a single fluid system is less well regulated (see Fig. 3.2). The immediate reaction of the nucleation and growth of grains to the density is also crucial for the variability mechanism.

When comparing Fig. 3.6 and Fig. 3.5, the absence of the slow phase in the variability cycle in the latter strikes the eye. This can be attributed to the imposed equilibrium drift in the 1.5–fluid flow. In the two–fluid system the drift velocity is directly influenced by the dynamics. In the 1.5–fluid model, however, the (equilibrium) drift velocity is only indirectly determined by the dynamics, namely via the (number) densities and the grain size. The fact that the variability character is still observed in this calculation is a consequence of the fact that the drift velocity, although not actively, does change as a function of time, in combination with the extreme sensitivity of the nucleation rate to the density and of the dynamics, via the drag force, on the grain size, and density. The sensitivity of the system is well visible in Fig. 3.5: any variation of the densities, grain size and nucleation rate is hardly visible (also because they are plotted logarithmically, ranging over many orders of magnitude) but the resulting variations in the velocity field are clearly present.

3.4.6 COMPARISON WITH OBSERVATIONS

To enable a qualitative comparison of our results with recent observations of IRC +10216 (Mauron & Huggins 1999; 2000), we have produced Fig. 3.7. The left frame is adapted from Mauron & Huggins (1999) (their Fig. 3). It shows the composite $B + V$ image of IRC +10216, with an average radial profile subtracted to enhance the contrast. We compare this image with the dust column density as a function of
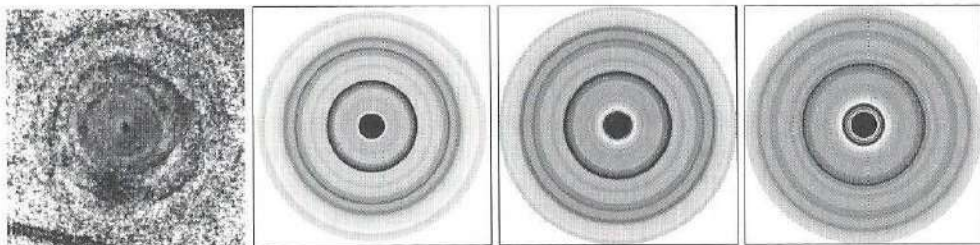
FIGURE 3.7: Upper left frame: Composite $B + V$ image of IRC +10216, with an average radial profile subtracted to enhance the contrast (adapted from Mauron & Huggins (1999)). Note that a few patches in the image are residuals of the removal of the brightest background objects, and these should be ignored. Other frames: series of snapshots of our 1.5–fluid calculation. Plotted is the dust column density, also with an average radial profile subtracted. The average radial profiles are calculated for each snaphot separately, hence the slight difference in colour from plot to plot. The theoretical profiles are shown for ages 44, 118 and 211 years with respect to the first frame in Fig. 3.5. The size of our computational grid corresponds with the field of view of the observational image ($131'' \times 131''$) and a distance of 120 pc.

radius for a number of snapshots in our calculation. The size of our computational grid (extended to 1287 R_*) corresponds with the field of view of the observational image ($131'' \times 131''$) and a distance of 120 pc. We have also subtracted an average radial density profile to enhance the contrast. Comparing dust column density to the observed intensity makes sense, since in the optically thin limit, the observed intensity, due to illumination by the interstellar radiation field is proportional to the column density along any line of sight (Mauron & Huggins, 2000). We used the results of the 1.5–fluid computation to produce Fig. 3.7 because there the short time scale structures are visible, whereas they are suppressed in the two–fluid model because the latter isn't always second order accurate. Note that the fact that in our calculated images all shells appear to be perfectly round is simply due to our assumption of spherical symmetry. The two dimensional plots were produced by simply rotating the spherically symmetric profile. In view of the fact that our calculations indicate that the chemical–dynamic system that regulates the behaviour of the envelope is extremely stiff and reacts violently to all kinds of changes, we think that it is rather unlikely that the observed circumstellar shells are indeed complete. It is intriguing to see that this idea is supported by the recent observations by Mauron & Huggins (2000), which show that most shells, although they may extend over much larger angles at lower levels, are prominent over about 45°.

As was mentioned before, Fig. 3.7 only offers a qualitative comparison with the observations. It can, however be used to establish that the spacing of the shells, small scale structure inside, large scale structure outside, is similar in the observations and calculations. This, is not surprising however, since merging of shells of various widths is due to dispersion, as was mentioned in Section 3.4.4.

3.4.7 THE TIME SCALE OF MASS LOSS VARIATIONS

The characteristic time scale of the variability corresponds to *the time needed by the rarefaction wave to cross the region between the sonic point and the innermost point of*

the nucleation zone. The width of this region is a few times 10^{14} to 10^{15} cm, depending on the phase. The velocity of the rarefaction wave equals the gas velocity minus the local sound velocity and is typically a few times 10^4 to 10^5 cm s^{-1}, depending also on the phase of the variability. The resulting time scale is roughly 50 to 500 years, which indeed corresponds to the time separation between two maxima in the mass loss rate in our calculation.

3.4.8 DISCUSSION

We found that the fact that the average grain size reacts strongly to the density structure is an essential ingredient for the formation of variability in the outflow. This explains why Mastrodemos et al. (1996) and Steffen & Schönberner (2000), who also performed time dependent, two–fluid computations, but did not take into account self consistent grain growth, did not encounter mass loss variations in the outflow.

Also, grain drift appears to be essential for variations in the mass loss rate. If grains can drift with respect to the gas, they can form regions of higher (or lower) density and/or size independently from the gas.

Periodic variability in the mass loss rate occurs in both the 1.5–fluid and the two–fluid calculations, because grains are allowed to drift in both cases. Both calculations give somewhat different results, though. Probably, assuming equilibrium drift a priori, as was done in the 1.5–fluid computation, influences the results, even if the grains in the two–fluid model turn out to drift at the equilibrium drift velocity as well. There are two reasons for this. First, the fact that equilibrium drift has established itself at the end of a numerical time step, does not mean that there has been equilibrium always during this specific time step. Hence, integration of the drag force over the time step provides a better value of the momentum transfer than multiplication of the drag force with the duration of the time step, c.f. Section 2.2.4. Second, the value of the equilibrium drift velocity in the 1.5–fluid calculation is indirectly determined by the dynamics, whereas in the two–fluid case there is a direct influence. Also, the fact that the 1.5-fluid calculation is second order accurate, but in the two-fluid calculation this level of accuracy is not always achieved, will lead to differences in the results.

We have not taken into account radiative transfer to solve the energy structure in the envelope. Also, we used a grey absorption coefficient in the radiative force and we did not calculate the grain temperature. These are severe limitations of the model. However, we believe that they do not influence the general conclusion that dynamics and chemistry together can lead to time dependent structures. It is more likely that taking into account the temperature structure determined by the optical properties of the grain population will make the variability even more pronounced. This is inferred from previous calculations by Fleischer et al. (1992) in which the interaction between atmospheric dynamics and radiative transfer was solved, imposing a time dependent inner boundary. Recently, Winters et al. (2000) performed similar calculations, also without the piston at the inner boundary. Their results also indicate that the coupling between the sensitive grain chemistry and the dynamics can lead to variability in the wind.

The role of the inner boundary in calculations as presented here is extremely important. It is possible to generate wind variability using a time dependent inner boundary.

We did not do this: the inner boundary that we have used was created to have as little influence on the results as possible. It consists of a fixed advective flux which can be modified by a diffusion term. The diffusive contribution to the flux is proportional to the gradients of the flow variables near the inner boundary, i.e. it is not externally prescribed. This is a realistic approach, since the inner boundary is located in the subsonic regime, where communication with lower layers is still possible. In this respect a completely fixed inner boundary would be less realistic.

We have referred to the quasi–periodic structure in our models as 'shells'. In order to prove that the structure is truly created in the form of spherical shells one should perform three dimensional hydrodynamics. Higher dimensionality will be a topic of future research.

Shell structure is observed around only a small number of Post–AGB objects and PNe. It is possible that the majority of objects doesn't have shells. A stationary wind can definitely exist if for some reason the equilibrium drift velocity is relatively low. This can be the case if the luminosity of the star is low. This will limit the mutual motion of both fluids and hence the value of the gas to dust density ratio so that the outflow will remain more smooth.

3.5   CONCLUSION

Our calculations suggest that the sensitive interplay of grain nucleation and dynamics, in particular grain drift, leads to quasi–periodic winds on the AGB. The characteristic time scale for the variability corresponds to the crossing of the subsonic nucleation zone by the rarefaction wave. This time scale also matches recent observations of IRC +10216.

More generally, we would like to stress that two–fluid hydrodynamics is important in order to reach self–consistency of the modelling method since the validity of the assumption of equilibrium drift is hard to check. *If* equilibrium drift is applied, it should be calculated by demanding the grains and the gas to be equally accelerated, rather than by equating the drag force and the radiation pressure on grains, because grains do have mass.

Observations also imply that gas and grains may not be spatially coupled (Sylvester et al., 1999) and that variations in the gas to dust ratio in the outflow may arise (Omont et al., 1999).

4

MASS LOSS VARIABILITY ON THE AGB

4.1   INTRODUCTION

[1] In the previous chapter, we have shown that grain drift is important for explaining the shell structures observed around a number of post-AGB objects and young Planetary Nebulae. In the current chapter we investigate under which circumstances these shells can form. We perform a number of model calculations for AGB stars with various stellar parameters. All calculations are performed once with and once without grain drift. Comparison of both classes of models leads to the conclusion that in some cases the neglect of drift seems justified on the basis of single fluid calculations but turns out to be a serious omission when grain drift is taken into account. The winds calculated assuming single fluid flow are, throughout parameter space, fairly stationary. When taking drift into account, a wide range of outflow types is produced with the same parameters. Depending mainly on the stellar effective temperature, luminosity and mass, the outflow is a stationary wind with a high mass loss rate; a wind with quasi periodic mass loss rate changes; or an outflow in which only the grains are driven out. Smooth winds are produced in objects with relatively low M_*, low T_* and high L_*. Mass loss variability, on a time scale of the order of 100 years, occurs when the star has high M_*, high T_*, and low L_*. This dependence on stellar parameters suggests that the formation of shells can be considered as a transient phase in the evolution along the AGB. This idea is supported by e.g. the fact that observed shell structures are located in the outermost regions of the circumstellar nebula.

The number of reported observations of shell structure around PNe is rapidly increasing. After the first indication of 'spherical bubbles' around NGC 6543 (Harrington & Borkowski, 1994), the presence of shells has been confirmed for, amongst others, AFGL 2688 (Sahai et al., 1998), IRAS 17150-3224 (Kwok et al., 1998), IRAS 17441-2411 (Su et al., 1998) and NGC 6543 (Balick et al., 2001). Images of shells around a post-AGB object were first obtained by Mauron & Huggins (1999; 2000). Recently, indications of mass loss variability, which underlie the formation of shells, were found in AGB stars (Marengo et al., 2001).

The notion that the outflow from late type stars is not necessarily stationary did not just come from high resolution observations that became possible during the 1990s. Simultaneously, advanced computer codes, that solve the equations of hydrodynamics in the circumstellar envelope were developed.

---

[1]The contents of this chapter overlap largely with Simis (2001)

Dynamical models by Fleischer et al. (1995) revealed a nonlinear effect due to the dust opacity, the exterior κ-mechanism. This effect arises as a result of backwarming after the formation of dust, by which pressure driven waves are initiated. These, subsequently, provide the density enhancements that are needed for the next dust formation and growth cycle. This leads to a pulsating outflow, with a period of the order of a few hundred days. Independent calculations by Höfner et al. (1995) have confirmed this mechanism. Although the variability in the calculations by Fleischer et al. (1995) and Höfner et al. (1995) seems to be very different from the mass loss variabilities we have encountered in the previous chapter, they too suggest that winds from late type stars may not be smooth at all as a result of a nonlinear interaction between grain physics and dynamics.

A few years earlier, Morris (1992) (cf. Deguchi (1997)) for the first time suggested an instability as a result of the presence of grain drift. Using linear stability analysis it was shown that this instability might give rise to inhomogeneities observed in the circumstellar environments of mass losing stars. Further investigations of this idea, with time dependent hydrodynamics calculations by Mastrodemos et al. (1996), however, lead to the conclusion that the instabilities cannot persist. From our calculations, see Chapter 3, is has become clear that drift *can* cause mass loss modulations and the formation of structure in the envelope. The main difference between our calculations and those by Mastrodemos et al. (1996) is that they give only a heuristic description of the inner 5-10 R_* and the dust formation, growth and evaporation processes in that region, whereas we include these consistently in our models.

Mass loss variability on a time scale of the order of ten to hundred years is also found in a few calculations by Winters et al. (2000). These are self consistent hydrodynamics calculations, of the same type as ours, though with a more advanced treatment of the radiative structure of the envelope, but assuming single fluid flow. We, too, find indications for variability on these time scales in our single fluid models, but the amplitude in the mass loss rate is very small compared to what is found in models with drift, see Section 4.3.2.

Apart from the mechanism suggested in Chapter 3, explanations for the occurrence of mass loss modulations on hundred year time scales are given by Soker (2000) and Garcia-Segura et al. (2001). Both relate the formation of concentric shells to the presence of a solar like magnetic activity cycle. Soker (2000) suggests that the enhanced magnetic activity at the cycle maximum results in an increase of magnetic cool spots. At the location of these spots the scale height will drop, which causes an increase in the dust formation and hence an increase in the mass loss rate. There are some specific requirements to make this mechanism work: the AGB star needs a companion which deposits angular momentum into the envelope. The mass of the companion has to be $\sim 0.3 M_\odot$ and the orbital separation has to be between 5 and 30 AU. Soker (2000) uses these constraints to explain that not all PNe show shell structure. If AGB stars possess a magnetic cycle, and if the period of this cycle is of the order of a few hundred years, this mechanism may indeed explain mass loss variability and the formation of shells. However, our self-consistent dynamical calculations and those performed by others previously indicate that the envelopes of AGB stars are highly self-regulating systems, with internal instabilities and characteristic time scales. Therefore, in order to judge the effectiveness of a mechanism like that proposed by Soker (2000), it has to be incorporated in a dynamical calculation.

Garcia-Segura et al. (2001) propose an active role of the magnetic field. A cyclic polarity inversion of the surface magnetic field of the AGB star leads to modulations of the magnetic pressure, which directly produce the density fluctuations. These results are produced using hydrodynamical calculations. Since the dynamical influence of the dust component was not taken into account in these calculations, we think that here, too, the effectiveness of the mechanism is not yet entirely convincing. Garcia-Segura et al. (2001) argue that shells formed by magnetic pressure waves persist longer than the shells that are generated without magnetic pressure in the wind. However, most cases of concentric shells are observed around young PNe or even younger objects. The only exception is Hubble 5, but in that case the shells were only detected around the waist of the bipolar object, so that they are probably shielded by a disk (Mellema, priv. comm.). Hence, even if shells produced by a mechanism as proposed in Chapter 3 would fade in due time, this would not be in contradiction with the observations.

4.2 MODELLING METHOD

4.2.1 HYDRODYNAMICS CODE

The calculations presented in this chapter were performed with our special purpose numerical hydrodynamics code. This second order, explicit, Eulerian, FCT/LCD code, in spherical coordinates is suitable for calculating the flow around AGB stars. The nucleation, growth and evaporation of grains is consistently incorporated in the calculation. Gas and dust can be considered as two separate fluids. In the previous chapter, we have demonstrated that the sensitive chemical structure of the envelope, in combination with two fluid flow, gives rise to a very nonlinear system, in which the mass loss rate shows time dependent variability. The time scale of this variability is of the order of that associated with the shells observed around a number of post-AGB objects and PNe.

The calculations for IRC +10216, presented in the previous chapter, were performed with a somewhat limited version of the hydrodynamics code which was described in Chapter 2. E.g., we did not consider grain evaporation. In the current version of the code we do include this effect. This results in a dust free zone near the inner boundary and consequently in somewhat lower outflow velocities, which are in better agreement with the observed values. Thermal grain evaporation is incorporated in the moment method (Gail et al., 1984; Gail & Sedlmayr, 1988) for the calculation of the grain populations according to the prescription by Gauger et al. (1990).

In the calculations presented here, we no longer assume the cross section for the interception of stellar light by the grains to be equal to the geometrical cross section. Also, the temperature stratification is no longer fixed. Instead, we calculate the temperature by assuming radiative equilibrium, using a method similar to that described by Lucy (1976) and Fleischer et al. (1992). For details, see Section 2.2.3.

Finally, we introduce a piston inner boundary condition. In doing so, we mimic the stellar pulsation. In Chapter 3, we did not take this into account, because we wanted to focus on the time dependent behaviour which arises in the circumstellar envelope in the absence of external dynamical input. Without this, however, a high luminosity and low stellar temperature and mass were required to drive the wind.

Since in reality AGB stars are known to be Long Period Variables (LPVs) and the stellar pulsation is an important factor in the dust driven wind, we take them into account in the following. An interesting question is whether stellar pulsation is able to suppress the quasi-periodic mass loss variations like those present in our calculations for IRC +10216. This turns out not to be the case. A detailed description of our inner boundary condition, including the piston, is given in Section 2.2.6 and Section 2.3.

A full description of the hydrodynamics code, as well as comparisons with results produced with similar codes, can be found in Chapter 2.

4.2.2   GRID OF MODELS

We have computed twenty models, in two sets. Each model is characterized by six parameters: the current mass (M_*), luminosity (L_*), and effective temperature (T_*) of the star, the carbon to oxygen abundance ratio (ϵ_C/ϵ_O), the period of the stellar pulsation (P), and its amplitude (Δv). With these parameters a hydrostatic state is calculated (c.f. Section 2.4), which serves as an initial model for the time dependent calculation.

To study the influence of the parameters T_* and L_*, we did 12 calculations with luminosity varying between $1.0 \cdot 10^4$ and $1.4 \cdot 10^4 L_\odot$ and effective temperatures in the range 2106 to 2741 K. All other input parameters were kept constant: $M_* = 1.0 M_\odot, \epsilon_C/\epsilon_O = 1.8, P = 650$ days and $\Delta v = 2.0$ km s^{-1}. The parameters for the remaining models were retrieved from theoretical evolutionary tracks on the AGB, kindly provided by Vassiliadis & Wood (1993). From their track for a star with a main sequence mass of 3.5 times solar and with solar abundances, we have chosen 8 models, representing states during the final two thermal pulse cycles. We have used the effective temperature, the luminosity and the current mass of these models to create hydrostatic initial profiles as input for our hydrodynamics calculations. The carbon abundance was assumed to be equal in all models, $\epsilon_C/\epsilon_O = 1.8$, and the amplitude of the piston as well, $\Delta v = 2.0$ km s^{-1}. The period of the stellar pulsation was calculated by Vassiliadis & Wood (1993) using the period-mass-radius relation and we have adopted the same values. Figure 4.1 shows the distribution of the 8 models based on the Vassiliadis & Wood tracks. A complete overview of our 20 models is given in Table 4.1. Therein we also listed the gravitational acceleration at the stellar surface,

$$g(R_*) = \frac{GM_*}{R_*^2} \propto \frac{T_*^4 M_*}{L_*} \qquad (4.1)$$

For models with equal carbon to oxygen abundance and piston period and amplitude, this quantity can be used as a measure for the power of the wind and hence the mass loss rate. The importance of the effective temperature relative to the luminosity and the mass in $g(R_*)$ is comparable to what was found by Arndt et al. (1997) in their approximate expression for the mass loss rate (c.f. Section 2.5). Alternatively, the density scale height $\mathcal{H}(R_*)$ can be used as an indication for the power of the wind:

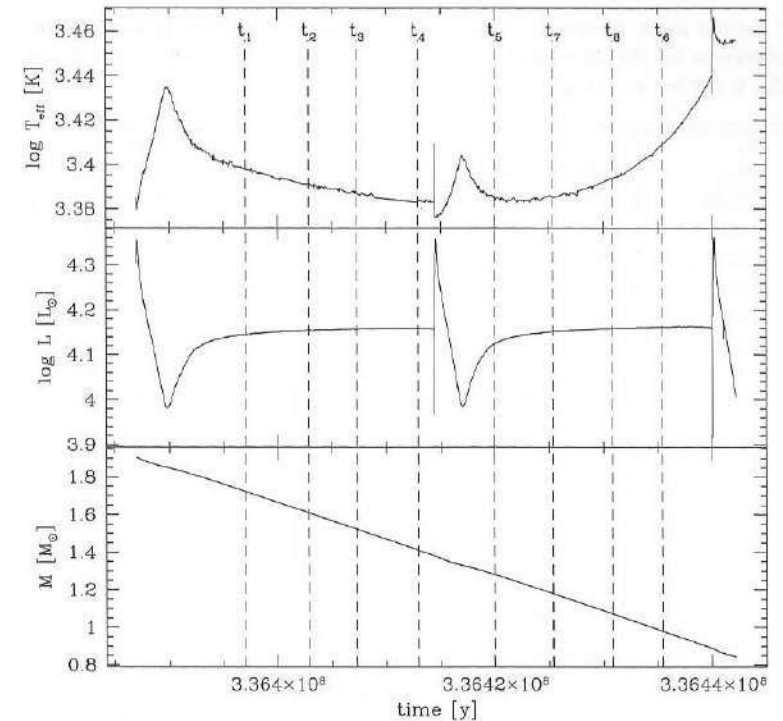$$\mathcal{H}(R_*) = \frac{\mathcal{R}_g T_*}{\mu g(R_*)} \qquad (4.2)$$

FIGURE 4.1: Theoretical tracks for the effective temperature, luminosity and stellar mass (Vassiliadis & Wood, 1993). Indicated with vertical lines are the parameter sets that we have used to calculate initial profiles for our hydrodynamical model calculations

Although this choice reduces the dependency on the temperature with one factor T_*, it will turn out to be a very useful quantity when comparing the mass loss behaviour of the various model calculations.

4.2.3   CALCULATIONS

A hydrostatic initial state is calculated for each of the models with the parameters of Table 4.1. The dynamical calculations are performed on a grid running from R_* out to 50 R_*. Grid cells are not equally spaced, since a high resolution is desirable in the subsonic area but not necessary in the outer envelope. The grid cells are distributed according to:

$$\frac{r[n] - r[n-1]}{r[1] - r[0]} = q^{n-1/n_{max}-1} \qquad (4.3)$$

The number of cells in the grid, n_{max}, used here is 500 and the size ratio q between the innermost and the outermost cell is 100.

Note that the grid used in these calculations is considerably smaller than in the calculations in Chapter 3 (where we had $R_{max} > 1000 R_*$). A consequence of this is that if shell structure forms, it will show relatively strong high frequency components. This is simply due to the fact that in this case we look for shell structure at 50 R_*,

TABLE 4.1: Stellar mass, temperature, luminosity, piston period, density scale height and gravitational acelleration for the 20 models. The carbon-to-oxygen ratio ϵ_C/ϵ_O is 1.8 and the piston amplitude Δv is 2.0 km s^{-1} in all models.

model	M_* $[M_\odot]$	T_* $[10^3$ K]	L_* $[10^4 L_\odot]$	P [days]	$\mathcal{H}(R_*)$ $[10^{12}$ cm]	$g(R_*)$ [cm s^{-2}]
t1	1.7236	2.500	1.3964	1412	1.350	$1.184\ 10^{-1}$
t2	1.6090	2.460	1.4289	1635	1.553	$1.013\ 10^{-1}$
t3	1.5226	2.438	1.4355	1788	1.694	$9.204\ 10^{-2}$
t4	1.4108	2.415	1.4421	1995	1.890	$8.174\ 10^{-2}$
t5	1.2807	2.427	1.3335	1979	1.896	$8.185\ 10^{-2}$
t7	1.1792	2.427	1.4191	2264	2.192	$7.082\ 10^{-2}$
t8	1.0719	2.477	1.4422	2318	2.305	$6.872\ 10^{-2}$
t6	0.9806	2.564	1.4521	2209	2.287	$7.169\ 10^{-2}$
a	1.0000	2.106	1.0000	650	2.788	$4.832\ 10^{-2}$
b	1.0000	2.317	1.0000	650	2.093	$7.079\ 10^{-2}$
c	1.0000	2.529	1.0000	650	1.610	$1.005\ 10^{-1}$
d	1.0000	2.741	1.0000	650	1.264	$1.386\ 10^{-1}$
e	1.0000	2.105	1.2000	650	3.350	$4.019\ 10^{-2}$
f	1.0000	2.316	1.2000	650	2.515	$5.889\ 10^{-2}$
g	1.0000	2.528	1.2000	650	1.934	$8.360\ 10^{-2}$
h	1.0000	2.740	1.2000	650	1.519	$1.154\ 10^{-1}$
i	1.0000	2.104	1.4000	650	3.914	$3.438\ 10^{-2}$
j	1.0000	2.315	1.4000	650	2.938	$5.039\ 10^{-2}$
k	1.0000	2.527	1.4000	650	2.259	$7.154\ 10^{-2}$
l	1.0000	2.738	1.4000	650	1.776	$9.860\ 10^{-2}$

whereas in Chapter 3 we focused on the regions at 100, 500 and 1000 R_*. At these large distances small scale structures have merged.

For the models based on the Vassiliadis & Wood (1993) parameters, we carried out single and two fluid calculations, i.e. calculations without and with fully free grain drift, see Section 3.2.2. The calculations a through l were performed once in single fluid mode and once in 1.5 fluid mode, i.e. assuming equilibrium drift.

Initially, all calculations are started without grain drift. Once the lower regions of the envelope are shaken by the stellar pulsation, grain drift is switched on for the 1.5 fluid and two fluid models. The stellar pulsation increases the scale height and hence facilitates the formation of dust and the onset of the dust driven wind. We shall see that when grain drift is taken into account, a wind is produced less easily. Hence, shaking the inner envelope is needed to start the wind in these cases. Note that this is quite realistic: during its evolution on the AGB the star will pulsate long before the stellar parameters have reached values for which a wind can be driven by radiation pressure on grains.

4.3   VARIATIONS IN MASS LOSS VARIABILITY

4.3.1   RESULTS

Figures 4.2–4.6 show the mass loss rate as a function of time through a sphere located at 50 R_* for our 20 models. The results for the calculations with and without drift

are plotted for each of these. The influence of drift is immediately clear: whereas the mass loss rate is fairly stationary in the single fluid calculations, large mass loss modulations occur in some of the models in which drift is incorporated. In Section 4.3.4 we investigate more closely the fact that drift turns out to be very important for the flow, whereas based on single fluid calculations it often seems negligible.

Based on Figs. 4.2–4.6, three types of flows are distinguished for the drift-models. First, there are the 'stationary flows', e.g. models a, b, e, f, i, j, and k. In these models, the mass loss rate as a function of time is rather constant. Some small scale modulations occur, but similar variability is present in the single fluid models. Hence, the variability in these winds seems to be mostly due to the stellar pulsation. The second class of flows are the models with clear mass loss modulations, occurring on a time scale of the order of 100 years: c, g, h, l, $t4$, $t5$, $t6$, $t7$, and $t8$. We will refer to this kind of variability as 'drift-driven mass loss modulations'. Finally, in some of the models the wind did not, or hardly, get started: d, $t1$, $t2$ and $t3$. We refer to them as 'non-winds'. Because it seems possible that for these models the dust can escape but the gas cannot, we sometimes call outflows of this type 'pure dust winds'. These results confirm the ideas of Salpeter (1974a), who realized that in case of a low luminosity and a high stellar mass grains could decouple from the gas.

There is a rather big spread in the time coverage of the various calculations, as can be seen from Figs. 4.2–4.6. The calculations which resulted in a stationary flow (models a, b, e, f, i, j, and k) covered approximately a thousand years. Some of the models with dust driven mass loss modulations ended after a few hundred years and the non-wind calculations generally stopped after a hundred years. The short time coverage of the latter is can be explained as follows. The poor coupling of gas and dust results in a flow pattern in which the gas is falling back onto the photosphere, while the grains escape at high velocities. Since the inner boundary of this version of the code is not suitable for accretion, the calculation stops as soon as the gas reaches negative velocities at the innermost gridpoint. Moreover, the huge velocity of the grains leads to very small numerical time steps, because the CFL condition (see Sect. 2.1.1) limits the flow to one cell per numerical time step. Therefore, if the velocity of the grains is e.g. a factor ten larger in the non-wind calculations than in the stationary wind models, the average numerical time step in the former is a factor ten smaller than in the latter. Hence, calculating the same number of of numerical time steps leads to a much lower time coverage for the non-wind calculations than for the stationary wind models. This argument also explains why the time coverage of the calculations with the modulated winds is lower than that of the stationary outflows. They too have on average larger dust velocities, and hence smaller time steps.

In Figs. 4.7–4.12, we have plotted a series of snapshots for two models of each class. In the first column, the velocities of gas (solid line) and dust (dashed line) are plotted. The second column shows the gas (solid) and dust densities (dashed). In the third column, the temperature is plotted with the solid line. The dashed line shows the amount of collisions with other grains that a grain at this radial position would have, based on the current grain number density and grain size profile. This variable will be discussed in 4.3.2. Finally, the fourth column shows the average grain size (solid line) and the nucleation rate (dashed).

The frames in the figures representing the non-wind models (Figs. 4.7- 4.8) are the
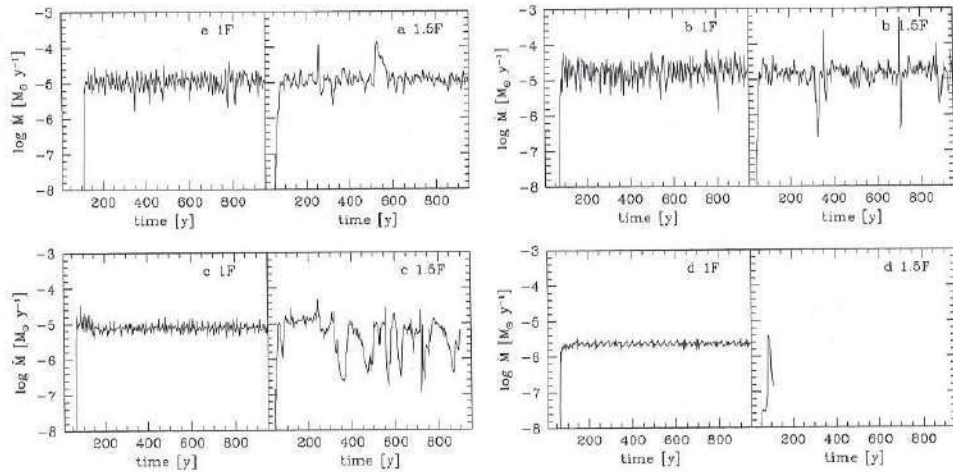
FIGURE 4.2: Mass loss rate versus time with (right frames) and without (left frames) drift, for models a–d
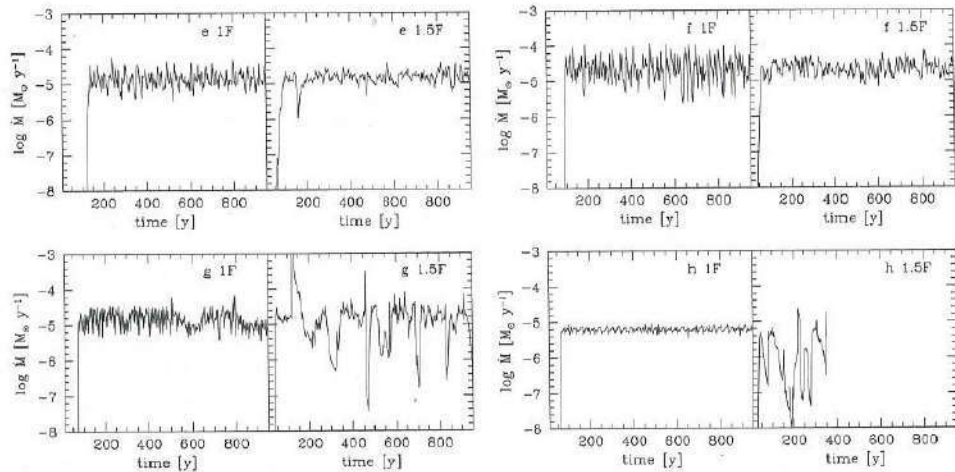

FIGURE 4.3: Mass loss rate versus time with (right frames) and without (left frames) drift, for models e–h

last frames before the calculation stopped. They show a rapid and enormous increase of the dust velocity, the gas velocity remains small or even becomes negative. For the modulated wind models, Figs. 4.9- 4.10, the frames are selected to cover approximately one variability cycle. In the case of the stationary winds, Figs. 4.11- 4.12 , no variability cycle is present, and the frames were selected to cover roughly the same time span as in the case of the modulated wind. It is immediately clear from these figures that in the envelopes with the smoothest winds, the drift velocity is relatively small, the density is high and the grains are, on average, large.

The gravitational acceleration $g(R_*)$ turns out to be a good measure for the character of the wind. For the models $a - l$, which all have equal pulsation period P, there is a
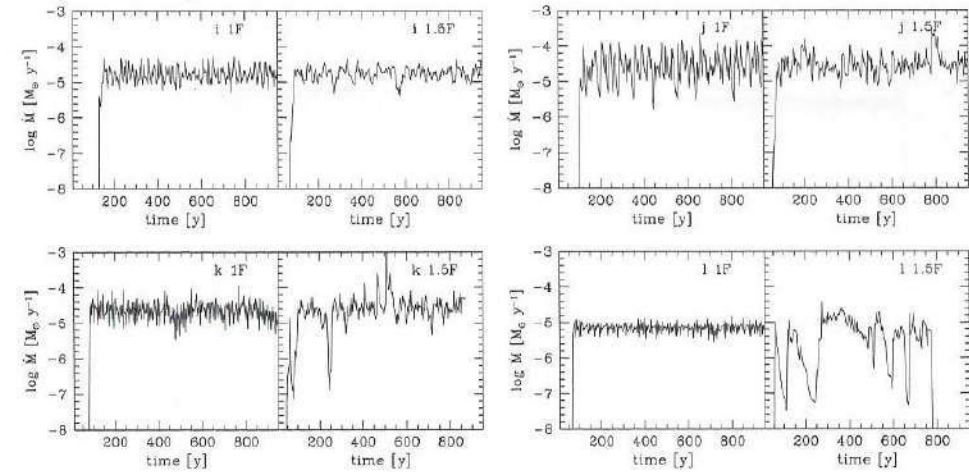
FIGURE 4.4: Mass loss rate versus time with (right frames) and without (left frames) drift, for models i–l
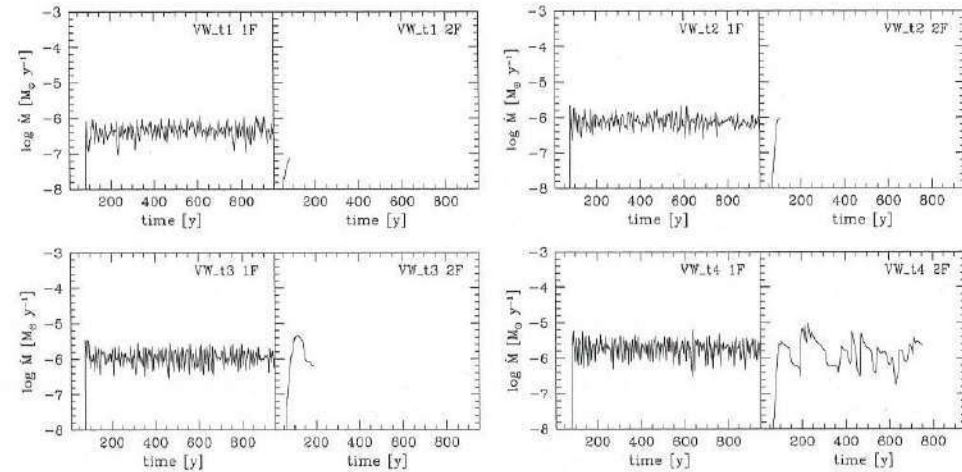

FIGURE 4.5: Mass loss rate versus time with (right frames) and without (left frames) drift, for models t1–t4

clear trend: we find that roughly for $g(R_*) \lesssim 7 \cdot 10^{-2}$ cm s^{-2} the wind is stationary and the average mass loss rate of the drift model is approximately equal to the mass loss rate in the single fluid model. For $7 \cdot 10^{-2} \lesssim g(R_*) \lesssim 1.2 \cdot 10^{-1}$ cm s^{-2}, mass loss modulations are found and the average mass loss rate is lower when drift is taken into account. For larger values of $g(R_*)$ the wind did not get started or stopped after the transient solution had passed. Also for the models based on the Vassiliadis & Wood tracks we see that high values of $g(R_*)$ indicate difficulties in driving the wind, whereas lower values correspond with a modulated outflow. The fact that for these models the mass loss rate as a function of time contains less variability on time scales of a few years is caused by the longer period of the piston.
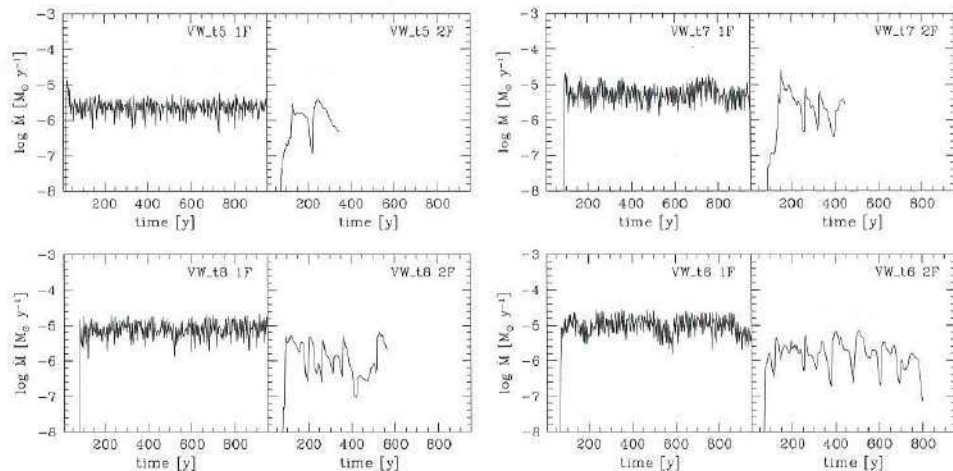
FIGURE 4.6: Mass loss rate versus time with (right frames) and without (left frames) drift, for models t5–t6

4.3.2 VARIABILITY BEHAVIOUR AS A FUNCTION OF STELLAR PARAMETERS

The mass loss rate of an AGB star increases along the AGB. Our calculations show that the mass loss not just becomes stronger but also more stationary with increasing luminosity, and decreasing effective temperature and stellar mass. This can be explained as follows.

The time scale of the variability is the crossing time of the rarefaction wave of the dust forming part of the subsonic region (see Chapter 3). The width of this shell is determined by the local density scale height. Consider an envelope of a star with a relatively high luminosity, a low effective temperature and a low mass and consequently a large density scale height (a 'late' AGB star). We compare the variability behaviour of this object and a second object which is more massive and has a low luminosity and a high effective temperature (an 'early' AGB star). Hence, the density scale height of the second object is smaller than that of the first.

In the envelope with the large scale height, $\mathcal{H}(R_*)$, the density gradient is less steep than in the envelope with the small scale height. Also, the temperature is lower in the first case. Therefore, dust formation is more efficient and starts closer to the stellar surface, in the first case. Consequently, in the subsonic region, the radiative force on the grains, which drives the wind, is strongest. The stronger the force, and the lower the radius at which it becomes effective, the more the sonic point of the wind is shifted to the star. Hence, the dust forming part of the subsonic region is relatively small when the density scale height is high. Thus, the variability period is short for objects with a large density scale height and longer when the density scale height is smaller.

The amplitude of the variability decreases with increasing $\mathcal{H}(R_*)$ as well. If the scale height is large, the density gradient is small and the density in the subsonic region remains high. In a high density environment, grains are efficiently decelerated. This limits the maximum drift velocity. The transfer of momentum from grains to gas becomes efficient already for relatively low values of the drift velocity. The minimum
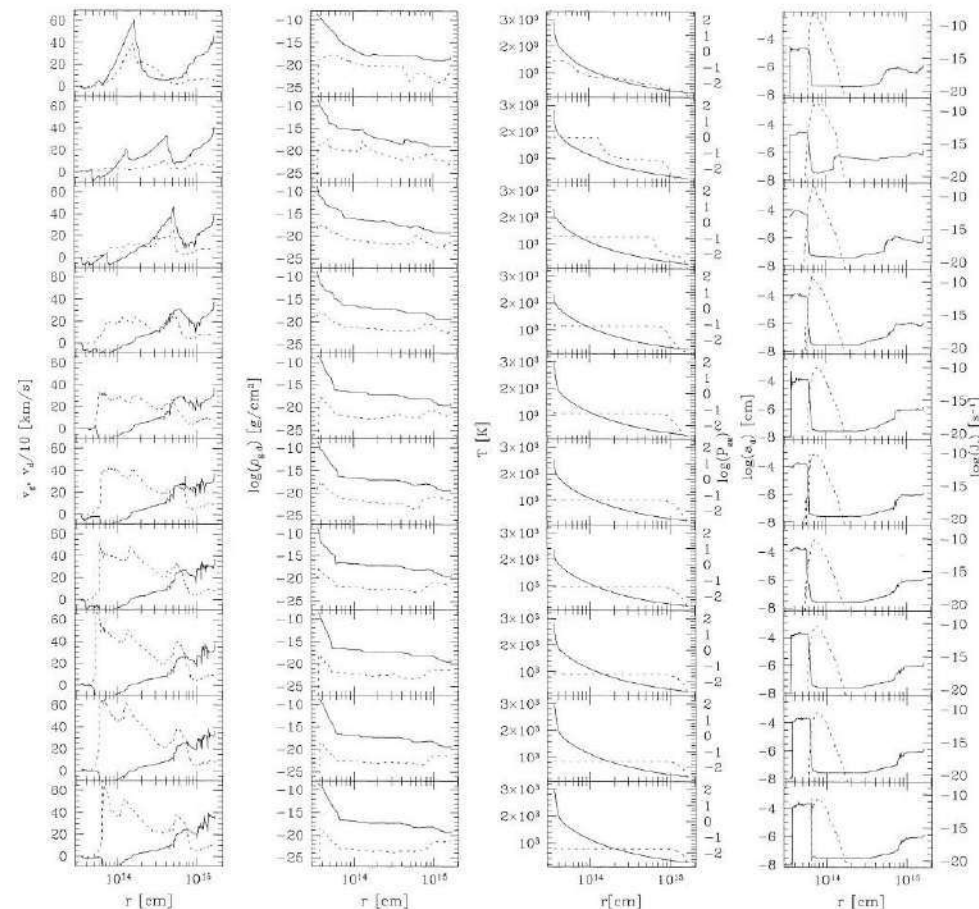

FIGURE 4.7: Model d, at time is 98.92, 102.1, 104.8, 106.7, 107.5, 108.1, 108.6, 108.9, 109.2, 109.6 year. First column: gas (solid line) and dust (dashed line) velocity. Second column: gas (solid) and dust (dashed) density. Third column, temperature (solid). The dashed line shows the amount of collisions with other grains that a grain at this radial position would have, based on the current grain number density and grain size profile. Fourth column: the average grain size (solid line) and the nucleation rate (dashed).

value of the mass loss rate reached during a variability cycle therefore is higher than it would have been in the case of an envelope with a smaller scale height and hence a lower density of gas.

The variability behaviour for four envelopes with different values of $\mathcal{H}(R_*)$ is schematically represented in Fig. 4.13. We label these schemes a (full line), b (dotted line), c (dashed line), and d (dashed–doted line). We have deliberately used names already used in our grid of calculations: here too, the period and amplitude of the variability increase from model a to c. We shall see that also scheme d, in which the mass loss rate becomes very low because not enough momentum is transfered to the gas, fits in this sequence.
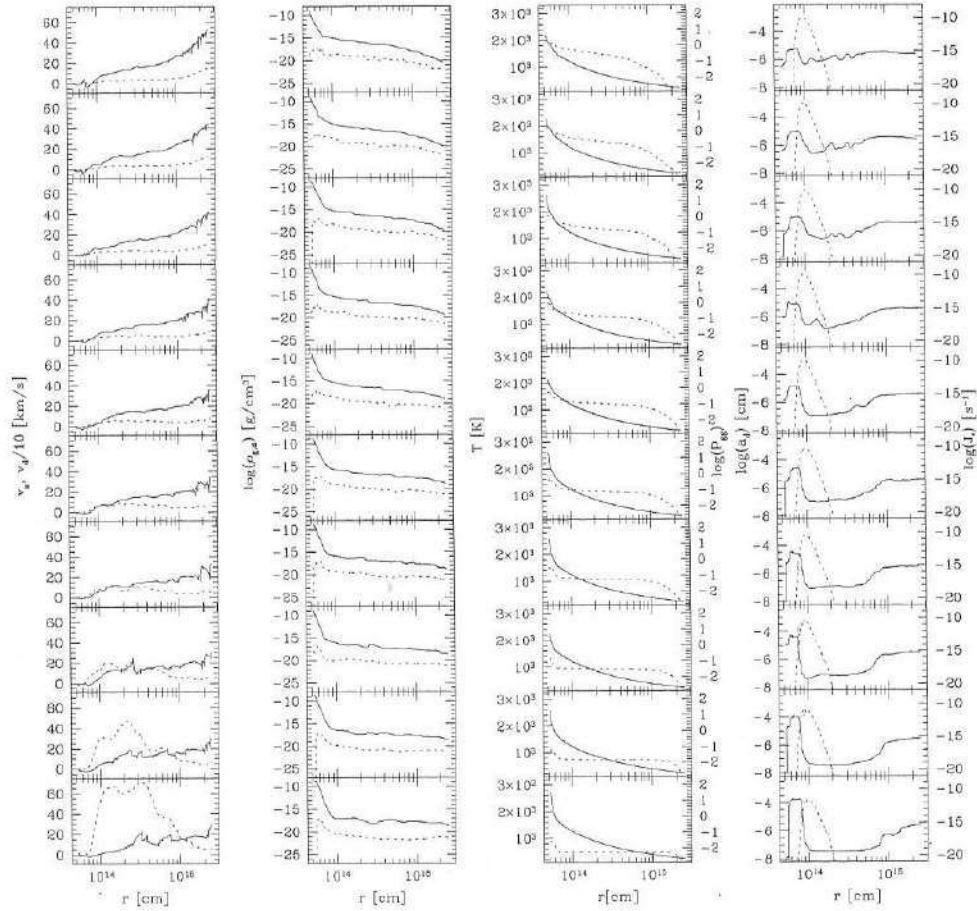
FIGURE 4.8: Model t2, at time is 71.2, 74.3, 77.5, 80.7, 83.8, 87.0, 90.2, 93.4, 96.5, 99.7 year. For identification of the plots: see Fig. 4.7

FIGURE 4.9: Model l, at time is 595, 608, 621, 633, 641, 644, 645, 647, 660, 673 year. For identification of the plots: see Fig. 4.7

First, we consider scheme c in Fig. 4.13, which represents an envelope in which the mass loss rate is modulated, on a time scale of the order of 100 years. The behaviour sketched in this scheme is found in our model calculations c, g, h, l, $t4$, $t5$, $t6$, $t7$, and $t8$. For models l and $t7$ we plotted a variability cycle in Fig. 4.9 and Fig. 4.10. We make a one-to-one correspondence between the frames in this variability cycle and the variability phases of scheme c. The phase in scheme c, labelled with $c1$, corresponds to frames 4, 5 and 6 of model $t7$ in Fig. 4.10: the velocity of the grains and hence the drift velocity are increasing, at the same time, the average grain size is decreasing. Smaller grains are efficiently accelerated by radiation pressure and hence move faster. Fast grains stay relatively briefly in the region where grain growth takes place and therefore remain small. The runaway process of smaller and faster grains is stopped as soon as the drag force becomes efficient. This happens at $c2$ in Fig. 4.13 and in frame 7 of model $t7$ in Fig. 4.10. The gas now is efficiently accelerated and a shock develops. At the same time the rarefaction wave starts to move in the direction of the star. The
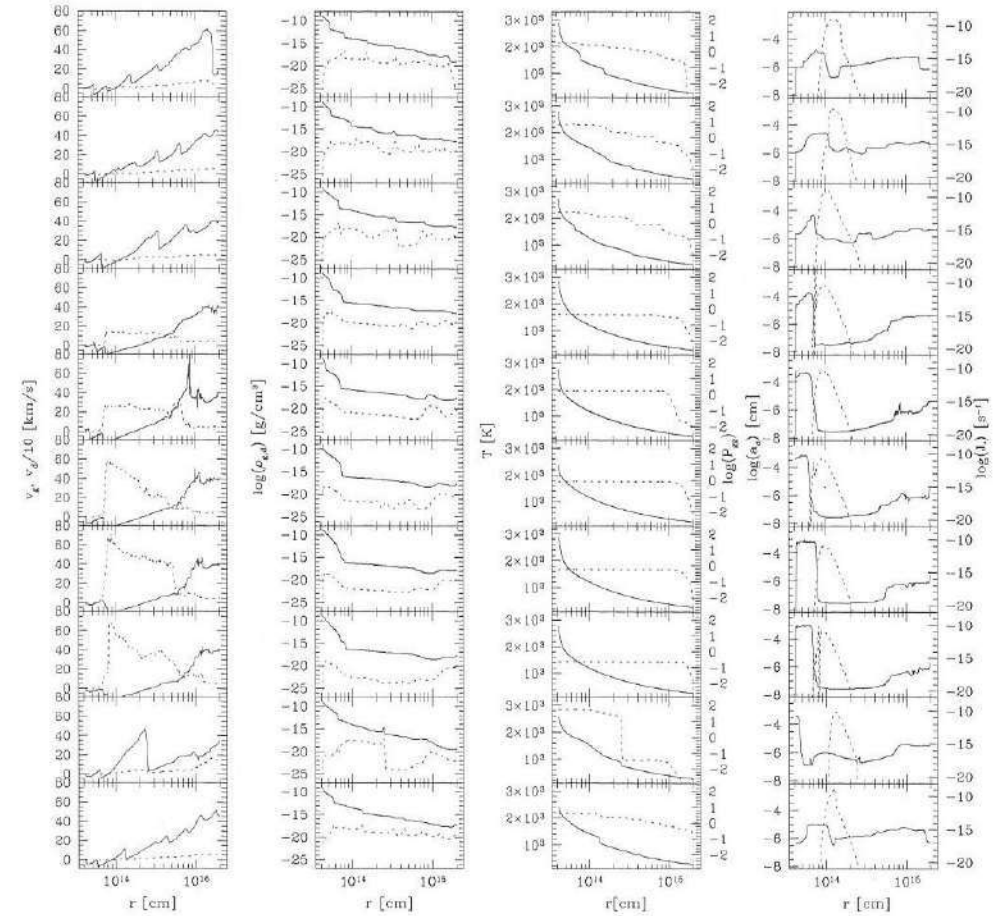
drift velocity gradually decreases, so that the residence time of the grains in the region of effective growth increases. Hence, the average dust grain becomes larger while it moves slower. We are now in phase $c3$ in Fig. 4.13, which corresponds to frames 8-10 and 1 in model $t7$ in Fig. 4.10. At this time the rarefaction wave is still crossing the subsonic region. Doing so, it counterbalances the density increase due to the revival of the outflow. Finally, approximately at the time when the rarefaction has crossed the subsonic, dust forming region, the gas density actually starts to decrease. Through the very sensitive coupling of the grain chemistry, this immediately results in a decrease of the average grain size. This instant is represented as $c4$ in Fig. 4.13 and corresponds to frame 2 and 3 in model $t7$ in Fig. 4.10. Once again, the runaway process of smaller and faster grains starts.

The variability behaviour for the schemes a and b is exactly the same as for curve c, but the amplitude and period of the modulation are smaller. If the density scale height of the envelope is big enough, the period and amplitude of the mass loss modulation
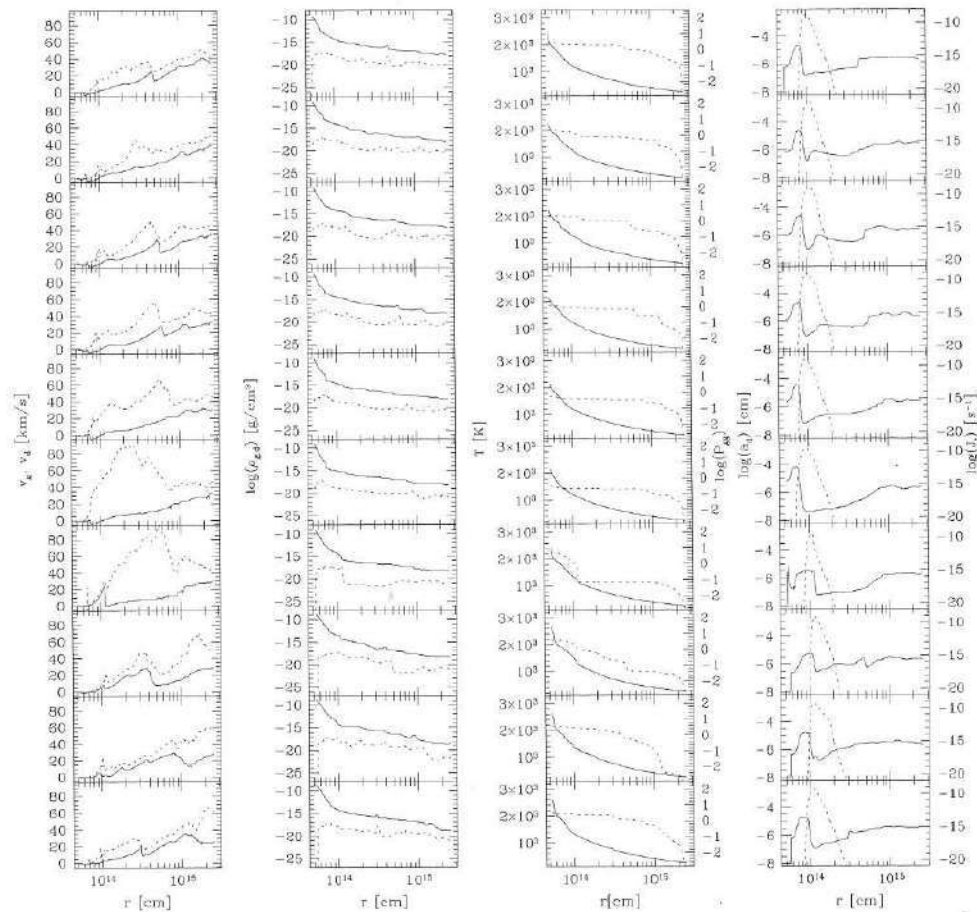
FIGURE 4.10: Model t7, at time is 265, 271, 277, 284, 290, 296, 303, 306,312, 318 year. For identification of the plots: see Fig. 4.7

FIGURE 4.11: Model e, at time is 549, 555, 562, 568, 574, 581, 587, 593, 600, 606 year. For identification of the plots: see Fig. 4.7

drops to values comparable to the period and amplitude of those that are due to the stellar pulsation. It is then no longer possible to discriminate between the two modes of variability. This is presumably the case for the models in our grid that we have characterized earlier as 'stationary': models a, b, e, f, i, j, and k. The 'hiccups' in the mass loss that appear in some of these models, see Figs. 4.2–4.6, can now be explained as well: they are due to some kind of beating between the stellar pulsation and the drift-driven mass loss variability, which now occur on approximately the same time scale.

Above, we have explained that in an envelope with a high density scale height, the limited drift velocity reduces the period and the amplitude of the drift-driven variability. Similarly, in an envelope with a very low density scale height (caused by e.g. a high effective temperature, a high stellar mass or a low luminosity) the few grains that form are barely decelerated. This leads to very large values of the variability period and amplitude of the mass loss rate. In the (hypothetical) limit
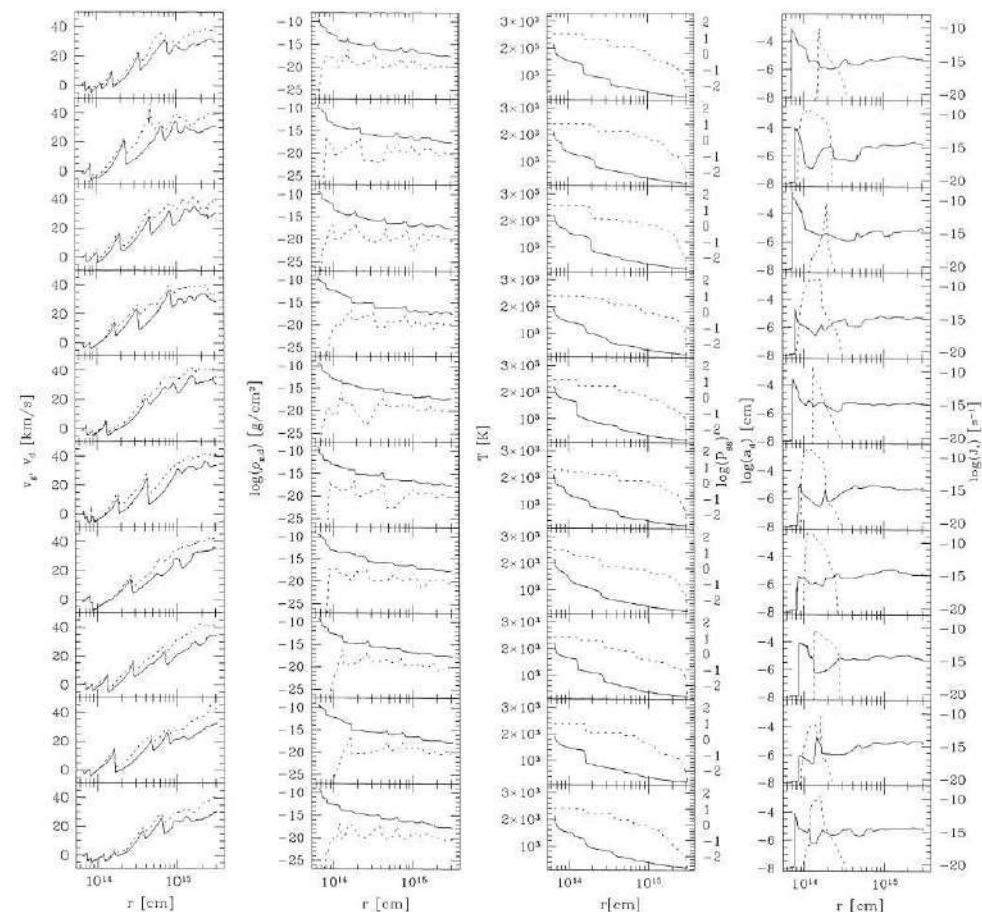
of unlimited grain drift, this results in extremely small, ever-accelerating grains that escape without dragging the gas along. This is probably what made it impossible to complete our model calculations d, $t1$, $t2$ and $t3$.

In reality, the drift velocity cannot be unlimited because either grain–grain collisions or sputtering will eventually destroy them. This increases the total grain-surface and consequently increases the momentum transfer rate from grains to gas particles. Hence, even in a very low density environment, the runaway process of smaller and faster grains eventually stops. Presumably, an equilibrium state is reached: small dust grains flow out at high but constant velocity. The depleted gas may flow out in a very dilute wind or may even stay behind and eventually fall back onto the star. Whether or not this scenario works cannot be checked with our current version of the hydrodynamics code.

We have explained why some AGB models, calculated taking into account grain drift, show mass loss variability on a time scale of the order of 100 years, and some do not. A careful look at Figs. 4.2–4.6 shows that in some of the calculations in which
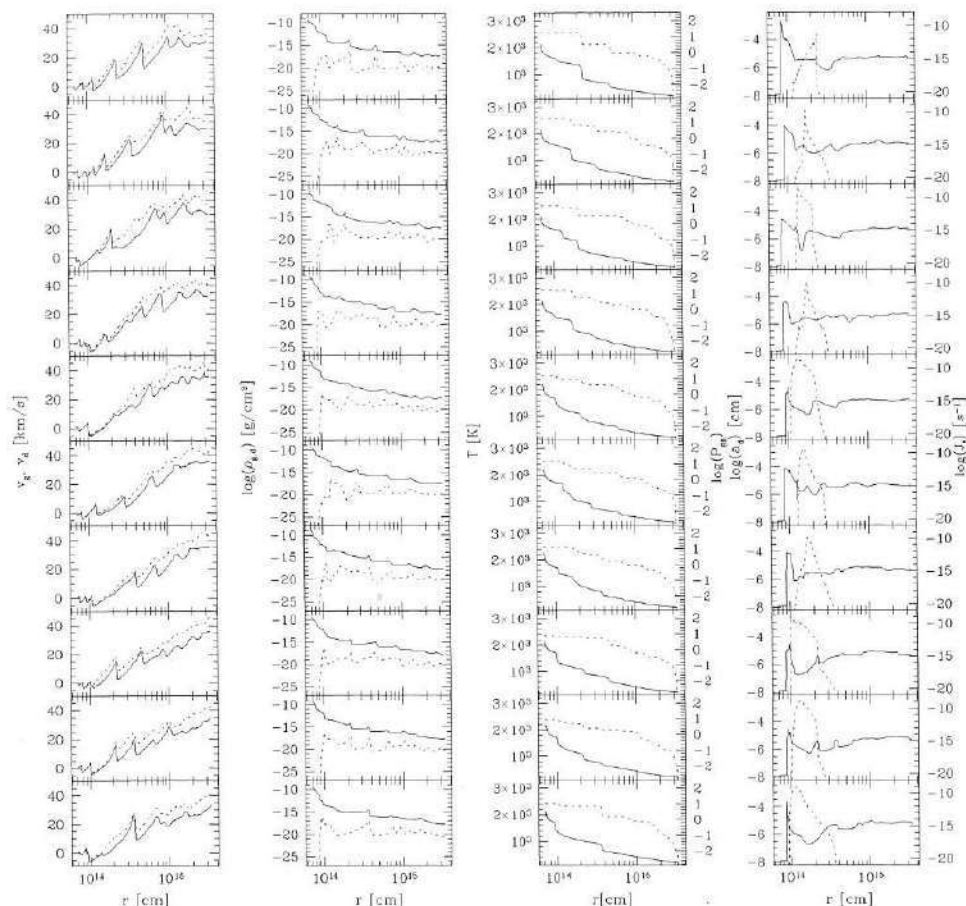
FIGURE 4.12: Model i, at time is 835, 841, 848, 854, 860, 867, 873, 879, 886, 892 year. For identification of the plots: see Fig. 4.7

drift was not taken into account (g, k, $t7$ and $t8$), mass loss modulations on roughly the same time scale but with a much smaller amplitudes are present. Their origin can be explained as follows. The shocks that develop in the models with drift, at the time the drift velocity suddenly starts to decrease, do not develop in the single fluid case. Still, shocks with a different origin, e.g. as a result of the stellar pulsation, are definitely present in the envelope. These shocks, too, give rise to rarefaction waves, which need a certain amount of time to cross the subsonic region. Doing so, it influences the local density and thus the grain nucleation and growth rates in the same way as it did for the models with drift. In this case, the changing density does not influence the drift velocity and the momentum transfer rate. Therefore, variations of the mass loss rate on similar time scales as the drift-driven mass loss modulations can occur in the absence of drift. The amplitude of these variations is limited, though. Maybe this also explains the variability in the mass loss rate in the calculations by Winters et al. (2000).
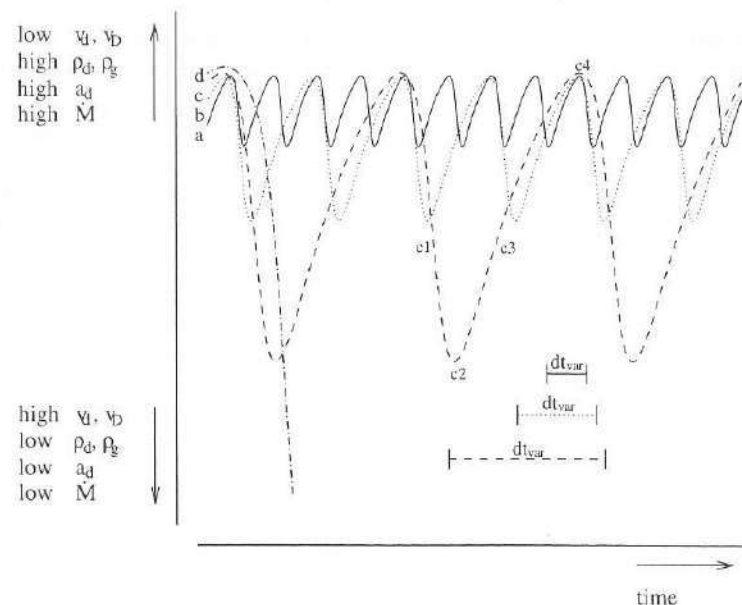
FIGURE 4.13: Schematic representation of the variability behaviour of circumstellar envelopes with various density scale heights: a (full line)=very high scale height, b (dotted line)=high scale height, c (dashed line)=low scale height and d (dashed-dotted line) = lowest scale height. For details, see Section 4.3.2.

Summarizing: we have provided an explanation for the differences in the variability behaviour between 'late' AGB objects (high L_*, low T_* and M_*) and the 'early' (low L_*, high T_* and M_*). The critical quantity is the density scale height in the subsonic region. If this is large, the density gradient is small so that dust forms efficiently and the momentum due to radiation pressure is easily transferred to the gas. Therefore, the drift velocity remains small and the mass loss rate stays high. The smaller the density scale height, the steeper the density gradient. A steeper density gradient involves less massive dust formation, hence a lower driving force for the wind. Therefore, the subsonic region extends to larger radii, which in turn brings about a larger time scale for the mass loss modulations. The amplitude of the modulations is large because the momentum transfer does not become effective until the drift velocities are high, and the mass loss rate is low.

4.3.3   IMPLICATIONS FOR THE MASS LOSS HISTORY OF AN AGB STAR

By using the terms 'early' and 'late' AGB stars for the objects with and without considerable drift-driven mass loss variability, we have suggested that mass loss variability is a phase in the evolution on the AGB. In the current section we advance several observations that support this suggestion. First, however, we elaborate a bit more on this phase.

The number of calculations that we have carried out is not sufficient to determine in detail the mass loss behaviour from the early AGB phase until its end. What we have

seen, though, are indications that there exists a trend: the higher the density scale height at the bottom of the envelope, the more stationary the outflow is. The decrease of the temperature and mass, and the increase of the luminosity and consequently the density scale height of stars during their AGB evolution are well established facts. Therefore, we infer that an AGB star starts its dust driven mass loss history with a modulated wind and a low mass loss rate. The variability period and the amplitude of the mass loss rate decrease in the course of time, so that the wind becomes rather stationary as its mass loss rate increases. The sudden increase of the temperature that occurs at the time the star is leaving the AGB involves a drop of the density scale height. This may lead to another brief period of modulated mass loss, or even to an outflow in which insufficient momentum is transferred to the gas, so that only the grains escape.

To illustrate the long term variations in the mass loss variability, we have constructed Fig. 4.14. In it, we have plotted, for six objects with different main-sequence mass (but all with solar metalicity), the density scale height as a function of time. To do so, we made use of the evolutionary tracks provided by Vassiliadis and Wood (1993) once more. As expected, we see that the density scale height globally increases as a function of time. Note that this is not a monotonic function of time: on shorter time scales, $\mathcal{H}(R_*)$ rapidly goes down after each thermal pulse. The horizontal lines in Fig. 4.14 mark the various stability regimes. The calculations in which the mass loss rate was fairly stationary, have a scale height between the dashed lines in the figure. The dotted lines mark envelopes with scale heights for which an outflow with drift driven variability was found. Envelopes with a scale height between the full lines have a very weak wind, or maybe a pure dust wind.

From the stability regimes, we now indeed see that during its evolution, the mass loss of an AGB star becomes gradually more and more stationary. The impact of a thermal pulse on the envelope is strong enough to temporarily alter the character of the outflow: a smooth outflow may turn into a variable wind for a while, immediately after a thermal pulse has gone off. When, and how long, the AGB star has a wind with drift driven variability depends on the mass of the star on the main sequence.

We want to stress that we do not intend to claim that we have, with our model calculations, fixed *the* variability strip for drift driven variability on the AGB. With Fig. 4.14 we just want to indicate that it can exist. In order to actually define such a regime, we should have, in the first place, carried out many more calculations, with a much wider variation in the stellar parameters. Second, we should have used evolutionary tracks which are consistent with our calculations. This is not the case for the tracks provided by Vassiliadis & Wood (1993). The mass loss rates following from our calculations are not in agreement with the mass loss laws they have applied to calculate the AGB evolution. The only solution to this is to perform self-consistent calculations which cover the complete evolution on the AGB.

Furthermore, note that the density scale height is only useful as a very global indicator for the variability behaviour. It does not depend on the chemical composition of the envelope and it is not influenced by the stellar pulsations, which in reality is definitely the case. The fact that $\mathcal{H}(R_*)$ cannot be an excellent indicator for the stability type is also obvious from Fig. 4.14, in which the variability regimes overlap. Finally, we should even refrain from using the term 'variability regime', since we have demonstrated in the previous section that there exists a continuous spectrum of variability types.
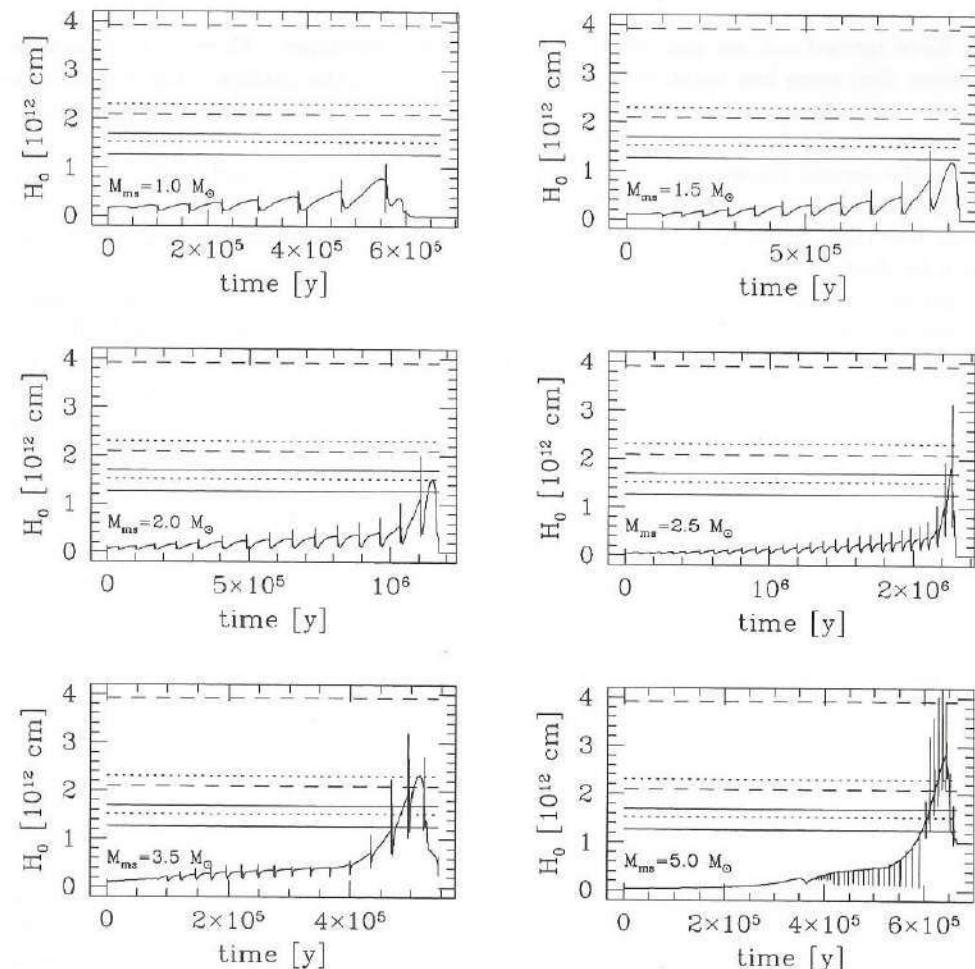

FIGURE 4.14: The 'variability strip' for AGB stars, in terms of the density scale height at the bottom of the circumstellar envelope. The region between the dashed lines marks values of the density scale height for which a 'stationary' or 'smooth' wind was found. For density scale heights between the dotted lines, outflows characterized by drift-driven mass loss variability were found. Full lines limit the scale heights of model calculations which ended as 'non-winds'. The curves represent the evolution of the density scale height as a function of time for a certain initial (main-sequence) mass according to the Vassiliadis & Wood (1993) evolutionary tracks.

One could infer from the results presented here that the lower limit of the variability strip gives the lowest possible value of the mass loss rate. With Figs. 4.2–4.6, this would lead to the conclusion that the lower mass loss limit for AGB winds is roughly 10^{-7} $M_\odot$ y^{-1}. This is not the case, lower mass loss rates have been observed on the AGB. This is not in contradiction with our results, for two reasons. Firstly because, as was mentioned above, we do not claim that we have, with our calculations, fixed the location of the instability strip. E.g. a change in the adopted optical properties of the grains might shift the variability regime to higher of lower mass loss rates. Note that

we have carried out our calculations in carbon rich envelopes. There is no reason to assume that mass loss variability does not take place in the outflows that originate in oxygen rich circumstellar environments. But it is not possible to predict which mass loss rates should be associated with a quasi-periodical outflow in that case.

In the second place, our calculations relate to dust driven winds only. It is very likely that, on the very early AGB, pulsations are driving an outflow with a very low mass loss rate. Although not driven by radiation pressure on grains, these winds may even be dusty.

Although care should be taken when interpreting our results, various observational results support the idea that modulated mass loss is indeed a phase on the AGB.

First, there is the fact that in all cases in which shell structure was observed around post-AGB objects or PNe, the shells were the outermost part of the nebula. Hence, the modulated outflow must have taken place before the smooth and dense final wind phase started.

The silicates of which the dust around oxygen rich AGB stars consists come in two different forms: crystalline and amorphous. With the Short Wavelength Spectrometer, on board of the ISO satellite, it became possible to study the mineralogy of AGB stars. One of the results revealed by the SWS spectra was the fact that crystalline silicates are predominantly present around objects with a high mass loss rate, and that amorphous silicate dust is found near objects where it is low (Waters & Molster, 1999). There are various explanations for these observations. Tielens et al. (1998); cf. Waters & Molster (1999), suggest that for low mass loss rates Fe adsorbs on Mg-rich crystalline silicates, which thereby change into Fe-rich amorphous silicates. Kemper et al. (2001) show that, due to a temperature difference between amorphous and crystalline silicates, the circumstellar envelope can contain up to 40% of crystalline silicates, before its presence starts to show up in the spectra. The calculations presented in this chapter support two other explanations for the absence of crystals in low mass loss rate outflows.

The first explanation is based on the fact that amorphous grains are better absorbers than crystalline grains. The better the absorptivity of a grain, the more effectively it is accelerated. Hence, the role of the absorptivity due to the lattice structure is comparable to the role of the grain size discussed in Sect. 4.3.2. We have seen that in high mass loss rate outflows, the scale height is relatively high. This allows the formation of grains rather close to the star, and hence at rather high temperatures. High temperature condensates are more likely to have a crystalline structure than low temperature condensates. This is because it takes a certain amount of energy for the atoms to arrange themselves in the ordered lattice structure. Our calculations show that when the mass loss rate is high, the drift velocity of the grains is relatively low. This is beneficial for the crystallization of the grains, since it causes them to stay long enough in the high temperature regions to order their lattices. The fact that crystals have a rather poor absorptivity and hence are not very efficiently accelerated facilitates further crystallization. Due to grain-grain collisions, the crystalline dust could become amorphous again, but in the outflows with high mass loss rates this is not very likely, as we will show below.

Grains that form in the envelope of an object with a low mass loss rate tend to have a high drift velocity, see Chapter 3. These grains have an amorphous structure at formation, because they form relatively far away from the star and hence they are

low temperature condensates. It is very well possible that the outflow in this case is driven by stellar pulsation, and not by radiation pressure on grains, because they are not yet present in the subsonic regions. Because of their high drift velocity, the grains move away from the star very fast. Therefore, their residence time in the highest temperature regions close to the stellar surface is short. This means that there is no chance that they can crystallize. This could have happened if they had stayed closer to the star a bit longer: crystallization can take place if amorphous grains are heated and cool down slowly.

We have seen that when the mass loss rate is low, it is very likely to be modulated as well. For these conditions, the average drift velocity is large and so is the variation in the drift. This means that grain–grain collisions will take place. In these collisions any crystalline dust present could be turned into amorphous dust as the grain partly melts due to the collision (Sylvester et al., 1999).

In order to destroy dust in grain-grain collisions, the probability for a grain to encounter another grain on an outward directed ray has to be one or bigger. This probability, as a function of the radial position of the grain, and based on the current density and average grain size profiles is given by

$$P_{gg}(r) = \int_r^\infty n_d(r')\pi \langle a_d(r')^2 \rangle \, dr' = \int_r^\infty \sigma_0 K_2(r') dr' \tag{4.4}$$

In the second part we used the second moment of the grain size distribution, and σ_0 is the hypothetical surface of a monomer, see Section 2.2.2. Note that in practice we cannot integrate out to infinity but only out to the end of our computational grid, which is located at $50\,R_*$. Therefore, the collision-probability of grains near the outer boundary is found to be considerably lower than for grains at smaller radii. Moreover, even for a grain located at the innermost grid point, the calculated probability is only the probability that a collision takes place within $50\,R_*$. The probability is plotted in the third column of Figs. 4.7-4.12. We see that it is not very likely that the grains in the outflows with the lowest mass loss rates (non-winds, Figs. 4.7-4.8) collide with other grain on their way out. This is a consequence of the low number density of grains, under these circumstances. Hence, we can conclude that grain destruction through collisions between grains probably does not occur within the first $50\,R_*$ from the star.

In the envelopes with quasi-stationary outflow and a high mass loss rate (Figs. 4.11-4.12), the probability for grain-grain collisions is high but the drift velocity is low and rather constant. This implies that the collisions take place but are rather harmless and amorphization is not likely.

This is different for the winds with mass loss modulations and an intermediate mass loss rate, Figs. 4.9-4.10. There, the drift velocity is high enough to ensure collisions at tens of kilometers per second. In these cases, the amount of collisions that a grain undergoes on its way out following from Eq. (4.4) is lower limit to the true amount. This is because the modulation alternatingly produces fast shells of low density and slow shells of high density. Hence, grain-grain collisions in winds with modulated mass loss may lead to the amorphization of the dust that became crystalline at formation.

Consequently, it seems that during most of its lifetime on the AGB, a star produces amorphous grains in its envelope. Crystalline dust only forms and survives during the final stages of the AGB, when the mass loss rate is high and the drift velocity is low.

Marengo et al. (2001) presented the first indications for recent mass loss variability on a time scale of the order of 100 years in the circumstellar envelopes of AGB objects. The variability is inferred from the absence of hot dust and occurs for two thirds of the non-Mira stars and for one third of the Miras in their sample. This difference is interesting, and could not be explained by the authors. Our models now do allow an explanation for the fact that variability occurs more often in the non-Mira stars (Semi-Regular variables) since they are in an earlier phase of their AGB evolution than the Miras. Hence, the Non-Miras are indeed more likely to have a variable wind than the Miras.

Finally, there is the peculiarity in the abundance of several post-AGB (e.g. HR 4049, HD 52961 (Waelkens et al., 1991) and HD 44179, the central star of the Red Rectangle nebula) objects. Their atmospheres are metal-depleted. An explanation for this could be that all metals are incorporated in grains that have escaped form the star, whereas the depleted gas re-accreted (Venn & Lambert, 1990). This would fit nicely into the evolutionary sequence for stability on the AGB that we have proposed in the previous section. As a result of the sudden increase in the temperature, the density scale height at the bottom of the envelope rapidly decreases at the very end of the AGB phase. This enables once more a variable wind, or even a situation in which the gas is hardly accelerated by the grains anymore. For the actual re-accretion it is probably necessary that the decoupling of gas and grains occurs within an accretion disk (Waters et al., 1992). All of the post-AGB stars that show the abundance peculiarity turn out to be binaries and hence have disks (Van Winckel et al., 1995). Note that not all post-AGB objects show the depletion pattern, hence it seems likely that indeed a binary-disk is required for the depletion to take place.

A similar abundance pattern is found for the class of the λ Bootis stars, these objects have disks too (Venn & Lambert, 1990). For them, the firsts two-fluid hydrodynamics calculations, performed with the code presented in this thesis in a slightly adapted form for viscous disks, are hopeful: in a dilute gas with small grains the dust escapes and the gas is accreted (Kamp & Simis, 2001).

4.3.4 THE UNNOTICED IMPORTANCE OF GRAIN DRIFT

In Chapter 3, we have made a plea for the incorporation of grain drift. With the model calculations in the current chapter, we have even stronger arguments indicating the importance of drift. It turns out that *for some sets of stellar parameters (T_*, L_*, M_*) the justification of the neglect of grain drift is a direct consequence of the assumption of negligible drift itself*. In other words: when single fluid flow is imposed and when the (hypothetical) equilibrium drift is calculated, its value is small compared to the gas velocity. This seems to justify the neglect of drift. When, however, a calculation is done for a model with the same stellar parameters but *with* drift, the drift velocity may turn out to be not negligible at all. This can be explained as follows. In the case of the single fluid calculation, the amount of momentum transfer from grains to gas is always high, hence the mass loss rate and the density remain high. The higher the density, the lower the drift velocity, as is obvious from Eq. (2.123).

This is illustrated in Figs. 4.15-4.17. There, we compare the time-averaged gas velocity, drift velocity and gas density for calculations with and without drift. We use the
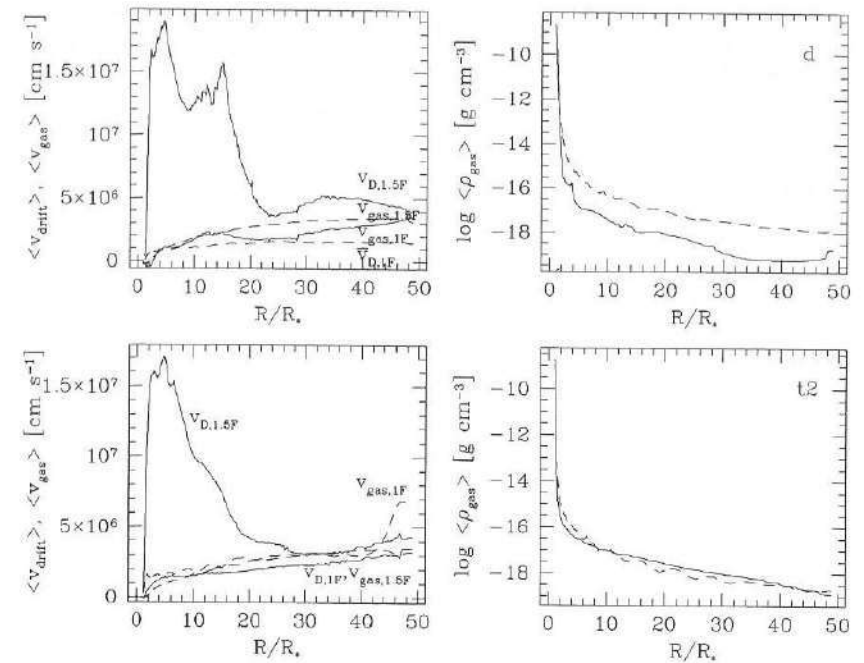
FIGURE 4.15: Left frames: time averaged gas velocity and drift velocity profiles for model d (upper row) and model t2 (lower row). Right frames: time averaged density profiles for model d and model t2. The full lines represent the calculations with drift, and the dashed lines the calculations without drift. The averaged profiles are calculated by averaging all the frames between the first and the last frame shown in Fig. 4.7-4.8 for these models. Especially in the lower regions of the envelope, where the actual wind driving takes place, the drift velocity is large in the models with drift, but negligible in the models without drift. The density at these radii is higher for the models without drift than for the models with drift.

calculations for which we have plotted a variability cycle in Figs. 4.7-4.12 and take the time average over the sequences plotted there. From these figures it becomes very clear that indeed the assumption of negligible grain drift seems to justify itself. Especially for the 'non-winds' in models d and $t2$ and the winds with drift-driven mass loss modulation, l and $t7$, the (hypothetical) equilibrium drift velocity in the single fluid calculation is much lower than the drift velocity in the calculation with drift. This would justify the neglect of the drift. It is important to realize, however, that in the case of single fluid calculations, the dust always transfers the maximum amount of momentum to the gas. Hence, the density in the subsonic regions is relatively high. This is visible in the figures as well: in the subsonic region, i.e. for small radii, the density is higher if drift is not taken into account than if drift is assumed to be present. So, establishing that the neglect of grain drift is legitimate, because the (hypothetical) equilibrium drift velocity in a single fluid calculation is small is not a fair judgement. Assuming drift to be unimportant is only justified if the drift velocity remains small in a calculation in which it *is* taken into account. This is the case for e.g. the models e and i, as is apparent form Fig. 4.17.
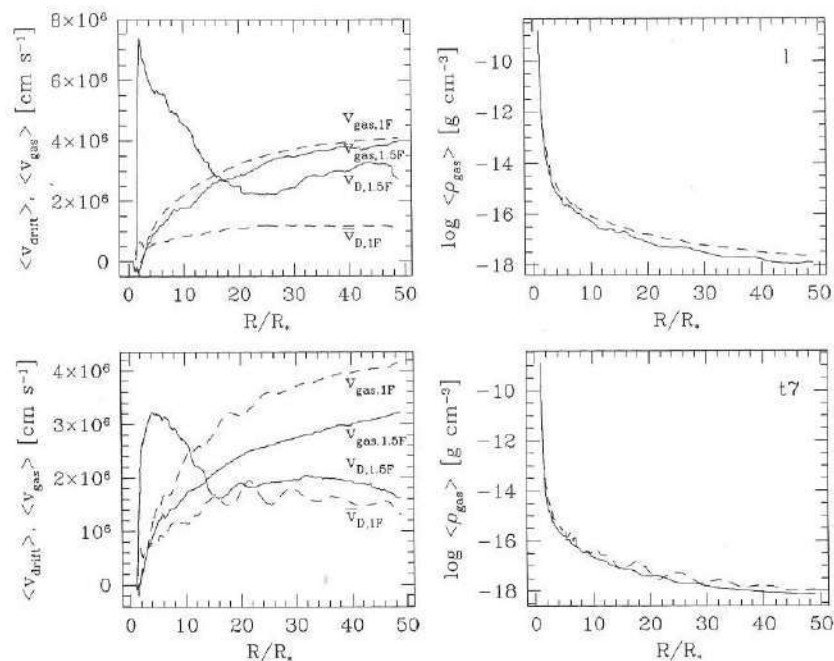
FIGURE 4.16: Left frames: time averaged gas velocity and drift velocity profiles for model l (upper row) and model t7 (lower row). Right frames: time averaged density profiles for model l and model t7. The full lines represent the calculations with drift, and the dashed lines the calculations without drift. The averaged profiles are calculated by averaging all the frames between the first and the last frame shown in Fig. 4.9-4.10 for these models. Especially in the lower regions of the envelope, where the actual wind driving takes place, the drift velocity is large in the models with drift, but negligible in the models without drift. The density at these radii is higher for the models without drift than for the models with drift.

4.4   DISCUSSION AND CONCLUSIONS

In the present and previous chapters, we have demonstrated the existence of disjunct phases in the variability cycle of dust driven AGB winds. High mass loss rates occur when the drift velocity is low and the and density is high. On the other hand, the mass loss rate is low if the drift velocity is large and the density is low. Both phases are not stable. This is due to the fact that smaller grains are more efficiently accelerated by the radiation pressure than the big ones. Small grains therefore stay relatively briefly in the region in which grain growth is most efficient. Larger grains are less efficiently accelerated and therefore have the opportunity to become even larger. The drift velocity of the grains in the small phase cannot increase without limit. The drag force is proportional to the square of the drift velocity and will therefore become relevant quite abruptly. As soon as this happens the average grain size starts to increase and the high mass loss phase is reached. The value of the drift velocity for which the process of smaller and faster grains is interrupted, the maximum possible drift velocity, depends on the stellar parameters. The more luminous, the cooler and the lighter the
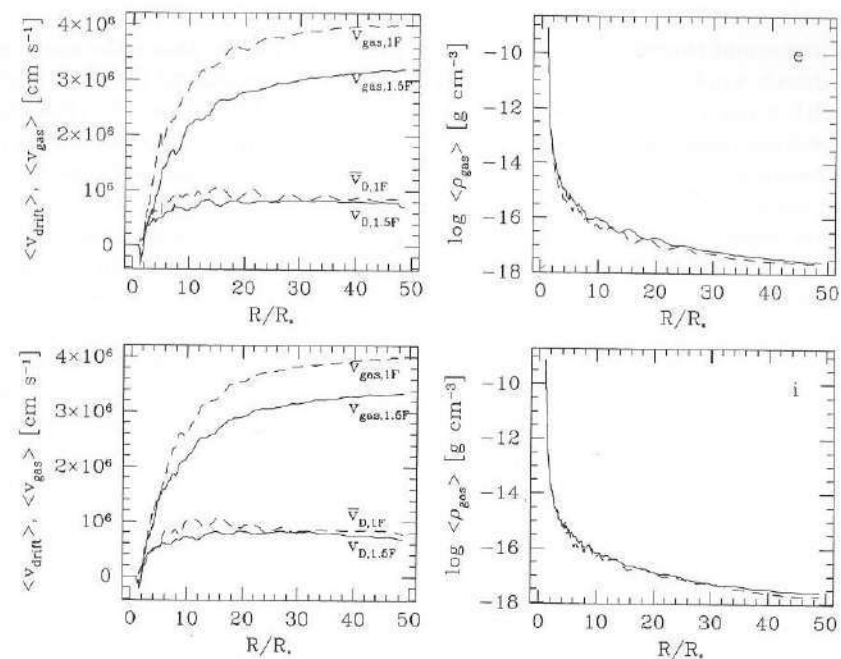

FIGURE 4.17: Left frames: time averaged gas velocity and drift velocity profiles for model e (upper row) and model i (lower row). Right frames: time averaged density profiles for model e and model i. The full lines represent the calculations with drift, and the dashed lines the calculations without drift. The averaged profiles are calculated by averaging all the frames between the first and the last frame shown in Fig. 4.11-4.12 for these models. For both models, the drift velocity is small compared to the gas velocity, also for the calculations in which drift is fully taken into account. This means that for the stellar parameters underlying these calculations, the neglect of drift would not have been a great omission.

star, the lower the maximum drift velocity and the smaller the variability amplitude and period. The sudden increase of the drag force is not only responsible for the end of the phase of low mass loss and high drift, it also leads to the transition back to this phase, after the mass loss has been high and the drift has been low. The sudden increase of the drag force drives a shock wave and a rarefaction wave. The latter needs some time to cross the subsonic region. Doing so, it gradually causes a decrease of the density there and hence inhibits further growth of the dust grains.

Since the variability behaviour depends on parameters such as the stellar mass, temperature and luminosity, it changes while the star moves up the AGB. Initially, the mass loss rate is low, thereafter the mass loss rate is variable on time scales of the order of a few hundred years. As the time scale and the amplitude of the mass loss modulations decrease, the mass loss rate increases. Observations seem to confirm this.

We mentioned the fact that the maximum drift velocity depends, through the density scale height, on the stellar parameters. There are other processes limiting the drift velocity as well. When the drift velocity is large, and highly variable, grain–grain collisions take place and can destroy grains. We did not take this into account in

our calculations. The large values for the drift velocities that we find in some of our calculations could therefore be unrealistic. Very little is known about the speed grains in dust driven winds can reach, however. Hoyle & Wickramasinghe (1962) report that grains with a size of 10^{-5} cm can reach velocities up to 1000 km sec^{-1}. Observations do not provide much information about drift or dust velocities. This is because of the limited resolution (e.g. ISO could resolve 150 km sec^{-1}) and also because the exact chemical composition of the grains is most often unknown.

Another aspect of our hydrodynamics code that allows for improvement is the inner boundary. Although perfectly suitable for wind solutions, the current implementation of the inner boundary cannot deal with accreting gas. Modification is necessary in order to find out what happens if the momentum transfer rate is really low, when grains drift at high speed through the low density environment. Does the dust really escape, leaving behind the depleted gas? And if so, does this phase of completely decoupled flow last long enough to explain the low abundance of metals observed in post-AGB objects such as HR 4049, HD 52961 and the central star of the Red Rectangle nebula, HD 44179 (Mathis & Lamers, 1992; Waters et al., 1992; Van Winckel et al., 1995; Waelkens et al., 1996)?

We have, in this chapter, drawn conclusions about the long term evolution of stars on the AGB. We did this on the basis of calculations that did not even cover a complete thermal pulse cycle, in combination with previous knowledge about the long term evolution of the stellar mass, temperature and luminosity. One of our conclusions was that the AGB wind can be variable, with a low average mass loss rate, for a significant period of time. This, of course, will influence its evolution. In order to make more accurate models of the evolution on the AGB, it is therefore necessary to perform calculations that cover at least a number of thermal pulse cycles.

ACKNOWLEDGEMENTS

REFERENCES

Andersen, H. C.: 1844, *The Ugly Duckling*

Arndt, T. U., Fleischer, A. J., & Sedlmayr, E.: 1997, *A&A* 327, 614

Balick, B., Preston, H. L., & Icke, V.: 1987, *AJ* 94, 1641

Balick, B., Wilson, J., & Hajian, A.: 2001, *AJ* 121, 354

Berruyer, N.: 1991, *A&A* 249, 181

Berruyer, N. & Frisch, N.: 1983, *A&A* 126, 269

Bhatnagar, P. L., Gross, E. P., & Krook, M.: 1954, *Phys. Rev.* 94, 511

Book, D. L., Boris, J. P., & Hain, K.: 1975, *J. Comp. Phys.* 18, 248

Boris, J. P.: 1976, *NRL Mem. Rep.* 3237

Boris, J. P. & Book, D. L.: 1973, *J. Comp. Phys.* 11, 38

Boris, J. P. & Book, D. L.: 1976, *J. Comp. Phys.* 20, 397

Bowen, G. H.: 1988, *ApJ* 329, 299

Buonanno, R., Corsi, C. E., Buzzoni, A., Cacciari, C., Ferraro, F. R., & Fusi Pecci, F.: 1994, *A&A* 290, 69

Carle, E.: 1969, *The Very Hungry Caterpillar*

Cherchneff, I., Barker, J. R., & Tielens, A.: 1992, *ApJ* 401, 269

Cherchneff, I. & Cau, P.: 1999, in *Asymptotic Giant Branch Stars/ T. Le Bertre, A. Lèbre and C. Waelkens (ed.)*, pp 252–259

Colella, P. & Puckett, E. G.: 1997, *Modern Numerical Methods for Fluid Flow*

Courant, R., Friedrichs, K. O., & Lewy, H.: 1928, *Math. Ann.* 100, 32

Deguchi, S.: 1997, in *IAU Symp. 180: Planetary Nebulae*, Vol. 180, pp 151+

Dominik, C.: 1992, *Ph.D. thesis*, Technischen Universität Berlin

Dominik, C., Gail, H.-P., & Sedlmayr, E.: 1989, *A&A* 223, 227

Dorfi, E. A.: 1998, in *Computational Methods for Astrophysical Fluid Flow, Saas-Fee Advanced Cource 27*, pp 263–341

Dorfi, E. A. & Höfner, S.: 1991, *A&A* 248, 105

Draine, B. D. & Salpeter, E. E.: 1977, *J. Chem. Phys* 67, 2230

Eulderink, F.: 1993, *Ph.D. thesis*, Sterrewacht Leiden

Feder, J., Russell, K. C., Lothe, J., & Pound, G. M.: 1966, *Advances in Physics* 15, 111

Fleischer, A. J., Gauger, A., & Sedlmayr, E.: 1992, *A&A* 266, 321

Fleischer, A. J., Gauger, A., & Sedlmayr, E.: 1995, *A&A* 297, 543

Fullerton, A. W.: 1997, in *Stellar Atmospheres: Theory and Observations; EADN Astrophysics School IX, Brussels, Belgium, 10 – 19 September 1996 / J.P. de Greve et al. (ed.)*, pp 187–237

Gail, H.-P., Keller, R., & Sedlmayr, E.: 1984, *A&A* 133, 320

Gail, H.-P. & Sedlmayr, E.: 1987, *A&A* 171, 197

Gail, H.-P. & Sedlmayr, E.: 1988, *A&A* 206, 153

Gail, H.-P. & Sedlmayr, E.: 1999, *A&A* 347, 594

Garcia-Segura, G., Lopez, J. A., & Franco, J.: 2001, *ApJL* submitted

Gauger, A., Gail, H.-P., & Sedlmayr, E.: 1990, *A&A* 235, 345

Gilman, R. C.: 1972, *ApJ* 178, 423

Glassgold, A. E.: 1996, *Annu. Rev. Astron. Astrophys.* 34, 241

Groenewegen, M. A. T.: 1993, *Ph.D. thesis*, Sterrenkundig Instituut "Anton Pannekoek"

Hackwell, J. A.: 1972, *A&A* 21, 239

Harrington, J. P. & Borkowski, K. J.: 1994, in *Bull. American Astron. Soc.*, Vol. 26, pp 1469+

Harten, A., Hyman, J. M., & Lax, P. D.: 1976, *Commun. Pure Appl. Math.* 29, 297

Höfner, S. & Dorfi, E. A.: 1997, *A&A* 319, 648

Höfner, S., Feuchtinger, M. U., & Dorfi, E. A.: 1995, *A&A* 297, 815

Hoyle, F. & Wickramasinghe, N. C.: 1962, *MNRAS* 124, 417

Icke, V.: 1988, *A&A* 202, 177

Icke, V.: 1991, *A&A* 251, 369

Kamp, I. & Simis, Y. J. W.: 2001, *in preparation*

Kemper, F., Waters, L. B. F. M., de Koter, A., & Tielens, A. G. G. M.: 2001, *A&A* 369, 132

Krüger, D., Gauger, A., & Sedlmayr, E.: 1994, *A&A* 290, 573

Krüger, D. & Sedlmayr, E.: 1997, *A&A* 321, 557

Kwok, S.: 1975, *ApJ* 198, 583

Kwok, S., Su, K. Y. L., & Hrivnak, B. J.: 1998, *ApJ* 501, L117

Lamers, H. J. G. L. M.: 1997, in *Stellar Atmospheres: Theory and Observations; EADN Astrophysics School IX, Brussels, Belgium, 10 – 19 September 1996 / J.P. de Greve et al. (ed.)*, pp 69–88

Lamers, H. J. G. L. M. & Cassinelli, J. P.: 1999, *Introduction to stellar winds*, Cambridge University Press

Laney, C. B.: 1998, *Computational Gasdynamics*, Cambridge University Press, Cambridge

LeVeque, R.: 1998, in *Computational Methods for Astrophysical Fluid Flow, Saas-Fee Advanced Cource 27*, pp 1–159

Liu, T.-P.: 1979, *Comm. Math. Physics.* 68, 141

Lucy, L. B.: 1971, *ApJ* 163, 95

Lucy, L. B.: 1976, *ApJ* 205, 482

MacGregor, K. B.: 1998, in *Cyclical Variability in Stellar Winds; proceedings of the ESO workshop, Garching, Germany, 14 – 17 October 1997 / L. Kaper, A.W. Fullerton (ed.)*, pp 3–15

MacGregor, K. B. & Stencel, R. E.: 1992, *ApJ* 397, 644

Marengo, M., Ivezić, Z., & Knapp, G. R.: 2001, *MNRAS* accepted

Mastrodemos, N., Morris, M., & Castor, J.: 1996, *ApJ* 468, 851

Mathis, J. S. & Lamers, H. J. G. L. M.: 1992, *A&A* 259, L39

Mauron, N. & Huggins, P. J.: 1999, *A&A* 349, 203

Mauron, N. & Huggins, P. J.: 2000, *A&A* 359, 707

Morris, M.: 1992, in *Mass Loss on the AGB and Beyond / H. Schwarz. (ed.)*, pp 60–72

Ney, E. P. & Allen, D. A.: 1969, *ApJL* 155, L193

Ney, E. P., Merrill, K. M., Becklin, E. E., Neugebauer, G., & Wynn-Williams, C. G.: 1975, *ApJL* 198, L129

Omont, A., Ganesh, S., Alard, C., Blommaert, J. A. D. L., Caillaud, B., Copet, E., Fouqueacute;, P., Gilmore, G., Ojha, D., Schultheis, M., Simon, G., Bertou, X., Borsenberger, J., Epchtein, N., Glass, I., Guglielmo, F., Groenewegen, M. A. T., Habing, H. J., Kimeswenger, S., Morris, M., Price, S. D., Robin, A., Unavane, M., & Wyse, R.: 1999, *A&A* 348, 755

Parker, E. N.: 1958, *ApJ* 128, 664

Roe, P. L.: 1991, *J. Comp. Phys.* 43, 357

Sackmann, I.-J., Boothroyd, A. I., & Kraemer, K. E.: 1993, *ApJ* 418, 457+

Sahai, R., Trauger, J. T., Watson, A. M., Stapelfeldt, K. R., Hester, J. J., Burrows, C. J., Ballister, G. E., Clarke, J. T., Crisp, D., Evans, R. W., Gallagher, J. S., I., Griffiths, R. E., Hoessel, J. G., Holtzman, J. A., Mould, J. R., Scowen, P. A., & Westphal, J. A.: 1998, *ApJ* 493, 301+

Salpeter, E. E.: 1974a, *ApJ* 193, 585

Salpeter, E. E.: 1974b, *ApJ* 193, 579

Schaaf, S. A.: 1963, in *Handbuch der Physik, volume VIII/2*, pp 591–625, Springer Verlag, Berlin, Göttingen, Heidelberg

Schöier, F. L.: 2000, *Ph.D. thesis*, Stockholm Observatory

Sedlmayr, E. & Winters, J.-M.: 1997, in *Stellar Atmospheres: Theory and Observations; EADN Astrophysics School IX, Brussels, Belgium, 10 – 19 September 1996 / J.P. de Greve et al. (ed.)*, pp 89–131

Simis, Y. J. W.: 2001, *A&A* submitted

Simis, Y. J. W., Dominik, C., & Icke, V.: 2001a, *A&A* submitted

Simis, Y. J. W., Icke, V., & Dominik, C.: 2001b, *A&A* 371, 205

Slyz, A. & Prendergast, K. H.: 1999, *A&A Suppl. Ser.* 139, 199

Soker, N.: 2000, *ApJ* 540, 436

Steffen, M. & Schönberner, D.: 2000, *A&A* 357, 180

Steffen, M., Szczerba, R., Men'shchikov, A., & Schönberner, D.: 1997, *A&A Suppl. Ser.* 126, 39

Steffen, M., Szczerba, R., & Schönberner, D.: 1998, *A&A* 337, 149

Su, K. Y. L., Volk, K., Kwok, S., & Hrivnak, B. J.: 1998, *ApJ* 508, 744

Sylvester, R. J., Kemper, F., Barlow, M. J., de Jong, T., Waters, L. B. F. M., Tielens, A. G. G. M., & Omont, A.: 1999, *A&A* 352, 587

Tielens, A. G. G. M., Waters, L. B. F. M., Molster, F. J., & Justtanont, K.: 1998, *Astrophys. Sp. Sc.* 255, 415

Van Leer, B.: 1984, *SIAM J. Scient. Statist. Computat.* 5, 1

Van Winckel, H., Waelkens, C., & Waters, L. B. F. M.: 1995, *A&A* 293, L25

Vassiliadis, E. & Wood, P. R.: 1993, *ApJ* 413, 641

Venn, K. A. & Lambert, D. L.: 1990, *ApJ* 363, 234

von Neumann, J. & Richtmyer, R. D.: 1950, *J. Appl. Phys.* 21, 232

Waelkens, C., Van Winckel, H., Bogaert, E., & Trams, N. R.: 1991, *A&A* 251, 495

Waelkens, C., Van Winckel, H., Waters, L. B. F. M., & Bakker, E. J.: 1996, *A&A* 314, L17

Waters, L. B. F. M. & Molster, F. J.: 1999, in *Asymptotic Giant Branch Stars/ T. Le Bertre, A. Lèbre and C. Waelkens (ed.)*, pp 209–219

Waters, L. B. F. M., Trams, N. R., & Waelkens, C.: 1992, *A&A* 262, L37

Wesseling, P.: 1992, *An introduction to multigrid methods*, John Wiley & Sons Ltd., Chichester, England

Winters, J.-M., Dominik, C., & Sedlmayr, E.: 1994, *A&A* 288, 255

Winters, J.-M., Le Bertre, T., Jeong, K. S., Helling, C., & Sedlmayr, E.: 2000, *A&A* 361, 641

Woitke, P.: 2001, *Reviews in Modern Astronomy* 14

Woodrow, J. E. J. & Auman, J. R.: 1982, *ApJ* 257, 247

Xu, K.: 1998, *van Karman Institute for Fluid Dynamics Lecture Series* 1998-03

NEDERLANDSE SAMENVATTING

Sterrenkundigen zijn soms echte hokjesdenkers. Ze sorteren sterren en sterrenstelsels op kleur, vorm, grootte en leeftijd en debatteren eindeloos om elkaar te overtuigen welke sorteermethode de beste is. De kleuterschool is dan ook een niet onbelangrijk deel van de opleiding van een sterrenkundige. Veel meer dan dat is als het goed is ook niet nodig om dit deel van dit proefschrift te begrijpen. Het is het verhaal van een rode reus, die in een witte dwerg verandert omdat hij bellen blaast.

DE ÉÉN Z'N DOOD...

Dit proefschrift gaat over sterren. Om sterren in hokjes te plaatsen lijkt niet meer nodig dan wat intuïtie, want ze gedragen zich precies zoals je zou verwachten. De licht-gewichten onder de sterren[2] leven hun leven heel rustig. Ze gebruiken weinig energie en kunnen tientallen miljarden jaren oud worden om vervolgens heel onopvallend te sterven. De zware jongens, die tien keer zo zwaar zijn als de zon (of nog veel zwaarder), leven een ruig en bombastisch leven. Ze bezitten al het goud en het uranium en staan erom bekend dat ze een enorme bende van hun omgeving maken. Ze worden slechts een paar miljoen jaar oud, dus zelfs de aarde is al duizend keer ouder. Tenslotte sterven ze een zéér gewelddadige dood, waar zelfs astronomen verlangend naar uitkijken.

Tussen deze uitersten bevindt zich de grote grijze (gele eigenlijk, in dit geval) mid-denklasse, waartoe ook onze zon behoort. Deze doodgewone sterren hebben de neiging om aan het einde van hun leven, als ze een jaartje of tien miljard oud zijn, wat in omvang toe te nemen. Dat hokjesdenkers het toch vaak bij het verkeerde eind blijken te hebben bleek al uit het relaas van Rupsje Nooitgenoeg en Het Lelijke Eendje (literatuur die een beetje kleuter er gelukkig in z'n vrije tijd bijleest). Ook voor de uitdijende middenmoot-sterren moeten alle vooroordelen overboord worden gezet: ze worden alleen maar mooier, spannender en nuttiger naarmate ze ouder worden.

OVER RODE REUZEN EN WITTE DWERGEN

Sterren ontstaan als gaswolken die bestaan uit voornamelijk waterstof en een beetje (10%) helium, samentrekken. De temperatuur in de samentrekkende gaswolk zal stij-gen, omdat de onderlinge afstand tussen de gasdeeltjes in de krimpende wolk steeds kleiner wordt. Het temperatuurverschil met de omgeving wordt hierdoor groter en de wolk zal proberen dit proces tegen te gaan door 'warmte' uit te stralen. Dat helpt echter absoluut niet: door dit energieverlies is de ster niet langer in staat z'n eigen gewicht te dragen en zal hij zelfs verder moeten krimpen. Groot zijn kost immers meer energie dan klein zijn, probeer maar eens een paar minuten je armen gespreid op schouderhoogte te houden. De wolk bevindt zich nu in een vicieuze cirkel: hij zal steeds kleiner en heter worden. Als de temperatuur echt hoog wordt is de redding echter nabij: in het centrum van de ster zullen kernfusiereacties gaan plaatsvinden, waarbij waterstof tot

---

[2]Toch nog altijd 10^{29} kilo zwaar en dus twintig duizend keer zwaarder dan de aarde, maar tien keer lichter dan de zon.

helium fuseert. Bij deze reakties komt energie vrij, zodat de wolk, die nu een ster is geworden, niet langer hoeft te krimpen om te compenseren voor z'n energieverlies door straling. Omdat hij niet verder krimpt zal hij ook niet verder opwarmen en daardoor niet harder gaan stralen. De stabiele levensfase die de ster nu doormaakt noemen we de hoofdreeks-fase. Tijdens deze fase heeft de ster dus een onveranderlijke temperatuur en lichtkracht (dat is de hoeveelheid straling die per seconde wordt uitgezonden). De zon is zo'n hoofdreeksster, al zo'n vijf miljard jaar en zal dat nog eens vijf miljard jaar blijven.

De kernfusiereakties in de kern zijn niet alleen essentieel voor de energievoorziening van de ster. Toen het heelal nog heel jong was, en er nog geen sterren waren, bestonden er slechts twee gassen: waterstof en helium, iets ogenschijnlijk zo doodgewoon als zuurstof was er nog niet. Gas bestaat uit minuscule deeltjes, atomen. We kennen tegenwoordig meer dan honderd verschillende soorten atomen, maar in het jonge heelal bestonden dus alleen nog waterstofatomen en heliumatomen. Verschillende atoomsoorten onderscheiden zich door hun massa. Waterstof is het lichtste atoom, en helium het op één na lichtste. Zwaardere atoomsoorten ontstaan door het samensmelten (fuseren) van lichtere. Dit gebeurt eigenlijk alleen maar op grote schaal in sterkernen. Alle atoomsoorten anders (lees: zwaarder) dan waterstof en helium (bijvoorbeeld zuurstof, koolstof, stikstof, ijzer) zijn dus gevormd in sterren.

Na totaal 10 miljard jaar te hebben geleefd als hoofdreeksster komt er een einde aan het rustige leven van de zon als hoofdreeksster omdat alle waterstof in de kern is omgezet in helium. Wat verder naar buiten toe is nog wel waterstof aanwezig, maar de temperatuur daar is niet zo hoog dat hierin kernfusie-reakties kunnen plaatsvinden. De bruikbare brandstof (waterstof in de kern) is dus op en de energievoorziening stopt. De ster is echter nog wel erg heet, en verliest dus nog steeds energie in de vorm van straling. Door dit energieverlies kan hij zich niet permitteren groot te blijven en zal hij opnieuw moeten krimpen. De waterstoflaag rondom de heliumkern wordt daardoor naar het hete centrum van de ster toegetrokken. Hierdoor wordt de temperatuur in deze laag zo hoog dat hij zal ontbranden. De energievoorziening is opnieuw veilig gesteld. De buitenste lagen van de ster gaan uitzetten en de energie die vrijkomt in de schil waar waterstofverbranding plaatsvindt wordt zeer efficiënt naar buiten getransporteerd. Hierdoor is de lichtkracht van de ster erg hoog, maar z'n temperatuur relatief laag. Net als een gasvlam kleurt een ster blauwer naarmate hij heter is, en rood als hij relatief koel is. Omdat de ster nu groot en rood is wordt hij een *Rode Reus* genoemd.

Omdat de verbranding in een schil om de heliumkern heen plaatsvindt, zal deze zelf nog verder blijven samentrekken. De temperatuur loopt daar in korte tijd op tot zo'n honderd miljoen graden. Bij die temperatuur zal helium explosief ontbranden en worden zuurstof en koolstof gevormd. Na de 'helium flits' wordt de ster tijdelijk weer wat kleiner en minder lichtkrachtig.

Maar ook de helium voorraad in het centrum van de ster raakt op den duur op en de fusiereakties stoppen weer zodra de hele kern van de ster uit koolstof bestaat. De geschiedenis herhaalt zich, want net als de eerste keer toen de ster tijdelijk zonder brandstof zat zullen fusiereakties in een schil om de kern het weer overnemen. Ditmaal zal daarbij helium fuseren. Iets verder naar buiten, in de eerder gevormde schil, wordt nog altijd waterstof in helium omgezet. Omdat opnieuw alleen de schillen aktief zijn wordt de ster lichtkrachtiger, koeler en groter, net zoals gebeurde toen hij voor de
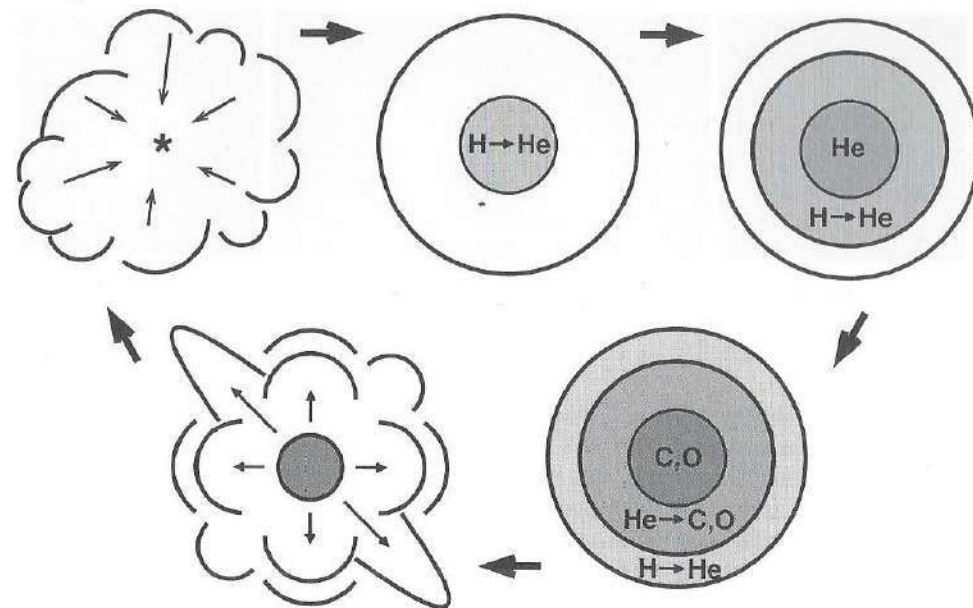

FIGUUR 1: De levenscyclus van een zon-achtige ster. 1. Een gaswolk trekt samen, wordt warmer, begint te stralen, krimpt verder, enzovoort, totdat de kern zo dicht is dat fusiereakties beginnen. 2. De ster is gedurende 10 miljard jaar een hoofdreeksster, die in zijn kern waterstof (H) in helium (He) omzet. 3. De rode-reuzenfase; de kern bestaat uit helium, in een schil er omheen wordt waterstof omgezet in helium. 4. Een AGB-ster heeft een kern van koolstof (C) en zuurstof (O) en in schillen om de kern reageert helium tot koolstof en zuurstof en waterstof tot helium. 5. De AGB-ster blaast zijn schillen weg, de kern verandert in een witte dwergster en verlicht de schil (planetaire nevel). De weggeblazen materie komt in de interstellaire ruimte en wordt gebruikt voor de vorming voor een nieuwe generatie sterren.

eerste keer in de Rode-Reuzen-fase terecht kwam. Deze tweede reuzenfase wordt de *Asymptotische Reuzenfase* genoemd, kortweg AGB, naar het engelse *Asymptotic Giant Branch*. Gedurende deze fase vindt ruwweg iedere tienduizend jaar een explosieve verbrandingsfase plaats (thermische puls).

Tegelijkertijd worden de buitenste lagen van de ster weggeblazen, dit heet de sterrenwind. Hoe en waarom dat gebeurt is het werkelijke onderwerp van dit proefschrift en komt iets verder in deze samenvatting aan bod. Dat de sterrenwind van deze reuzensterren eerder een orkaan is dan een zacht briesje blijkt uit het feit dat het massaverlies zo groot kan worden dat de ster in tienduizend jaar de helft van z'n massa kwijtraakt. Dat lijkt langzaam, maar in verhouding tot z'n leeftijd van tien miljard jaar is dat toch echt een heel 'Big Diet'. Ter vergelijking, als een mens in verhouding net zo snel zou willen afvallen zou hij in een uur tijd de helft van z'n gewicht moeten kwijtraken.

Door de thermische pulsen tijdens de AGB-fase worden helium, koolstof en zuurstof door de buitenste lagen heen gemengd. Deze stoffen worden dus in de wind naar buiten geblazen, samen met heel veel waterstof. Precies dat maakt de ogenschijnlijk saaie sterren zoals de zon zo ontzettend nuttig! Immers, wijzelf bestaan voor een heel groot deel uit water (dat een combinatie van waterstof en zuurstof is) en koolstof (spieren) en
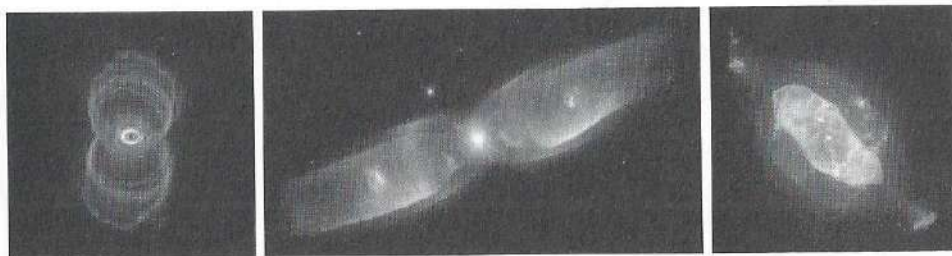
FIGUUR 2: Planetaire nevels: vuurwerk na een onopvallend leven van zo'n tien miljard jaar. Deze afbeeldingen, gemaakt met de Hubble ruimtetelescoop zijn nog veel mooier in kleur, zie http://www.stsci.edu/.

leven op een rotsachtige (silicium) planeet met een dampkring van stikstof en zuurstof. Alle essentiële bouwstenen voor ons leven zijn ooit geproduceerd in de kernen van sterren. Vervolgens zijn ze door sterrenwinden de interstellaire ruimte in geblazen en terecht gekomen in de gaswolk waaruit vervolgens ons zonnestelsel is gevormd. Deze kringloop van materie voor het ontstaan en sterven van sterren is geschetst in figuur 1. Maar, zoals gezegd helemaal aan het begin van dit verhaal: zonnen-op-leeftijd zijn niet alleen nuttig, maar ook erg mooi. Als de ster z'n hele schil heeft weggeblazen blijft alleen de kale kern over. Die kern is klein en heet, witheet zelfs, en wordt een *Witte Dwerg* genoemd. Het witte dwergsterretje zelf is niet van een betoverende schoonheid, maar het is in staat de weggeblazen gasschil te verlichten. En dat kan er spectaculair uitzien. Zulke verlichte gasschillen worden planetaire nevels genoemd. Dit omdat ze, toen ze voor het eerst werden waargenomen met kleine telescopen, er rond en groenig uitzagen en dus aan een nevelachtige planeet deden denken. Met de enorme telescopen van tegenwoordig zien we pas echt hoe mooi de planetaire nevels zijn. We zien nu ook dat de oorspronkelijk bolvormige nevel in sommige gevallen vervormd is tot een zeer complexe struktuur van schillen en soms zelfs heel langgerekt is geworden. Figuur 2 toont een paar planetaire nevels, maar eigenlijk komen ze in zwart-wit niet helemaal tot hun recht. Op de kaft van dit proefschrift staan er nog twee (de onderste twee figuren), maar hun weliswaar zeer fraaie kleuren pasten niet in het ontwerp.

Tenzij we tijdig een veilig heenkomen zoeken, bij voorkeur een eindje buiten het zonnestelsel, zullen we niet meemaken dat de zon op bovenbeschreven wijze z'n tien-miljardste verjaardagsfeestje viert. De aarde zal dan al opgeslokt zijn door de uitdijende zon. (Met reuzenster wordt dus inderdaad een *reus*achtige ster bedoeld.) Voordat dat gebeurt is de zon echter al zo groot en nabij dat de oceanen verdampen en de kleibodem van de Beemster en de Purmer als een schilfertje terracotta van het aardoppervlak springt. Want de rode reus is voor een ster dan wel koel, naar aardse maatstaven is hij met z'n 2500 graden nog altijd behoorlijk heet.

ZWARE JONGENS EN NOG MEER WITTE DWERGEN

Alvorens over te gaan naar wat er nu echt in dit proefschrift wordt beschreven gaan we nog even terug naar de allerlichtste en de zeer zware sterren. Want doen die laatste nu echt alleen maar kwaad? Hoe zwaarder een ster is, hoe hoger de temperatuur in de kern

kan oplopen en hoe meer verschillende chemische elementen (atomen) er geproduceerd worden. Alle sterren kunnen waterstof omzetten in helium. Zon-achtige sterren (tot acht keer zo zwaar als de zon) kunnen die helium vervolgens weer omzetten in koolstof en zuurstof. Nog zwaardere sterren hebben een kern waarin de temperatuur zo hoog wordt dat daaruit vervolgens magnesium, silicium en ijzer voortkomen. Dat zijn de echt zware jongens, en een probleem hebben ze wel degelijk. Het produceren van atomen zwaarder dan ijzer levert namelijk geen energie op, maar kost juist energie. Een ster die zojuist z'n kern van silicium heeft omgezet in ijzer zal weer even zonder brandstof zitten en dus gaan krimpen, net als hij deed toen z'n kern van helium was. Maar omdat kernfusiereakties met eindprodukten zwaarder dan ijzer geen energie meer opleveren is krimpen ook het *enige* wat hij nog kan doen om in z'n energiebehoefte te voorzien. Met catastrofale gevolgen: de kern van de ster zal ineen storten en onmiddellijk uiteen knallen. Dit heet een supernova explosie. Hierbij kan de kern van de ster veranderen in een zwart gat, een opeenhoping van materie die klein is, maar toch zo zwaar dat zelfs het licht er niet aan kan ontsnappen. De buitenlagen van de ster spatten met grof geweld uiteen. Daarbij wordt de interstellaire ruimte dus 'vervuild' met veel nuttig materiaal, zoals zuurstof, koolstof enzovoort, maar nu dus ook magnesium, silicium en ijzer en zelfs de echt zware metalen als uranium en plutonium die kunnen ontstaan omdat er bij de explosie heel veel energie vrijkomt. De zware jongens zijn dus best ergens goed voor. Dat ze bij hun gewelddadige dood naburige sterren een flinke dreun kunnen uitdelen vergeven we ze dus maar. Voor hetzelfde geld raken ze immers een wolk met gas, die daardoor ineenstort en een nieuwe ster wordt....

De ware uitvreters onder de sterren blijken de lichtgewichten te zijn, zij die op het eerste gezicht zo onschuldig en stil leken. Ze leven lang, maar dragen in die tijd nauwelijks bij aan de verfraaiing en ontwikkeling van hun omgeving. Ze maken immers geen koolstof, zuurstof enz. maar houden wel als een stelletje oude vrekken het waterstof en helium gas, waarmee zwaardere sterren nuttig werk hadden kunnen verrichten, lang bij zich. Uiteindelijk blazen ook zij hun buitenlagen weg, en wordt de kern een witte dwerg.

NIET SAAI MAAR WEL STOFFIG

Terug naar de zon-achtige-middenklassers-op-leeftijd. In hun buitenlagen is de temperatuur zo laag (ongeveer tweeduizend graden) dat moleculen kunnen ontstaan uit de koolstof-, stikstof- en silicium-atomen die in de kern geproduceerd zijn en die door de thermische pulsen door de buitenlagen heen gemengd zijn. Hoe lager de temperatuur, hoe groter de moleculen die kunnen ontstaan. De moleculen klonteren vervolgens samen tot kleine deeltjes vaste stof. Deze deeltjes zijn ongeveer een micrometer groot en worden door sterrenkundigen simpelweg stof genoemd. Zo kan uit koolstof roet gevormd worden en uit silicium glas. De vorming van dit stof is van groot belang voor de verdere ontwikkeling van de ster. En voor ons, omdat wij van het stof dat daar gemaakt wordt onze potloden en ramen maken.

De hoeveelheid stof die ontstaat is niet zo heel groot: slechts één procent van het het gas rondom de ster condenseert tot vaste stof. De invloed van het stof op het gas is echter enorm. Dat komt omdat het stof de straling (licht) van de ster heel
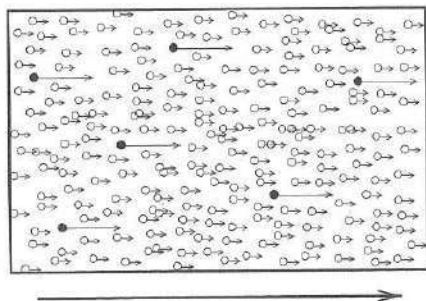
FIGUUR 3: Uitverkoop of stralingsdruk geeft aanleiding tot een kracht in de richting van de pijl. Hardlopers of stofdeeltjes (zwarte bolletjes) zijn gevoelig voor die kracht en slepen de rest van de massa (witte bolletjes) mee. Daarbij is het goed mogelijk dat er een snelheidsverschil is tussen de hardlopers (het stof) en het publiek (gas) dat ze meeslepen.

efficiënt kan absorberen. Een deel van de geabsorbeerde stralings-energie wordt door het stofdeeltje omgezet in bewegingsenergie. De straling oefent dus een kracht uit op het stof, we noemen dat stralingsdruk. Stof dat bestraald wordt zal daardoor bij de lichtbron vandaan bewegen. Het resterende deel van de energie wordt opnieuw uitgestraald. Omdat een deel van de energie al gebruikt was om te versnellen is het opnieuw uitgestraalde licht roder (minder energierijk, koeler) dan het licht dat door de ster werd uitgezonden. De aanwezigheid van de stoflaag om de ster zal er dus toe leiden dat de ster nog roder wordt dan hij al was en infrarode straling gaat uitzenden. Dat maakt het lastig dit soort sterren waar te nemen, want het menselijk oog is niet gevoelig voor infrarood licht, bovendien laat de dampkring van de aarde weinig infrarode straling door. Met speciale telescopen en vanuit de ruimte is het inmiddels wel mogelijk om stervende zonnen te bekijken.

EEN FRISSE WIND

Stofdeeltjes die versneld worden door de straling van de ster bewegen bij de ster vandaan en botsen onderweg naar buiten op de aanwezige gasdeeltjes die ze daardoor meesleuren. De gasdeeltjes zijn zelf nauwelijks gevoelig voor de straling en zouden in afwezigheid van het stof niet naar buiten bewegen. Zodra er gas wegstroomt van de ster spreken we daadwerkelijk van een sterrenwind. Het stof is dus verantwoordelijk voor de aandrijving van de sterrenwind[3]. De snelheden waarmee gas en stof naar buiten bewegen zijn allebei ruwweg 20 kilometer per seconde.

Tot nu toe werd vaak aangenomen dat het stof en het meegesleurde gas precies dezelfde snelheid hebben. Dat dat helemaal niet zo hoeft te zijn is eenvoudig in te zien. Stel dat zich in een winkelcentrum 1000 mensen bevinden waarvan er 10 (1%) graag nieuwe gympen willen kopen. Zodra er omgeroepen wordt dat de gympen op de sportafdeling in de aanbieding zijn trekken deze 10 mensen een sprintje die kant op. De

---

[3]Sterrenwinden kunnen ook op andere manieren worden aangedreven dan door stof. Onder andere omstandigheden kan het gas wel gevoelig zijn voor de straling van de ster en direct versneld worden. Ook kunnen bewegingen aan het steroppervlak (sterpulsaties) ervoor zorgen dat het gas wordt gelanceerd.

sportafdeling oefent duidelijk een kracht uit op deze mensen. De sportievelingen onder de kooplustigen behoren dus net als het stof rondom de ster tot de 1% van de massa die gevoelig is voor deze specifieke kracht. Door te gaan rennen, met een snelheid van zo'n 15 kilometer per uur, zijn botsingen met de rest van het publiek onvermijdelijk. Daardoor zullen enerzijds de hardlopers wat worden afgeremd, en anderzijds de overige mensen een kleine snelheid in de richting van de sportafdeling krijgen. We kunnen daarbij aannemen dat iedereen uit het overige publiek ongeveer dezelfde snelheid krijgt. Omdat er erg veel mensen rondlopen zal iedereen die met een hardloper in botsing is gekomen, en daardoor een hogere snelheid heeft gekregen dan de rest van de menigte, snel zelf botsen met iemand anders. Op die manier wordt de snelheid die door de hardopers wordt overgedragen aan aanvankelijk een paar mensen uit de menigte heel snel gelijkmatig verdeeld over iedereen. Het snelheidsverschil tussen de hardlopers en het overige publiek blijft echter bestaan en hangt af van een aantal factoren. Hoe meer publiek er is, hoe moeilijker het voor de hardlopers wordt om snel te lopen. Ook de grootte van de hardlopers is van belang, twintig rennende kinderen kunnen sneller door de menigte lopen dan tien volwassenen, die samen net zo groot (en zwaar) zijn. Dat komt omdat de kinderen kleiner zijn, en daarom minder vaak botsen.
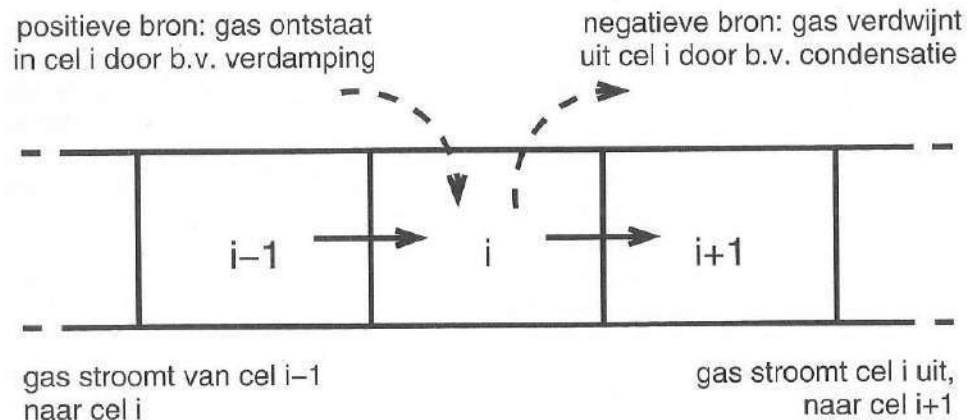
De hardlopers en het wandelende publiek, of het stof en het gas, kunnen beschouwd worden als twee 'vloeistoffen'. Er is een sterke kracht (uitverkoop of stralingsdruk) die er voor zorgt dat de ene vloeistof gaat stromen in de richting van de kracht. Doordat de versnelde, stromende deeltjes van die vloeistof in botsing komen met de deeltjes van de andere vloeistof (wandelend publiek of gas) gaat ook deze stromen in de richting van de kracht. Met de aanname dat het gas en het stof uiteindelijk dezelfde snelheid krijgen worden berekeningen aan dergelijke stromingen een stuk eenvoudiger, maar is er wel het risico dat interessante effecten over het hoofd worden gezien.

BEREKENINGEN

Het onderzoek beschreven in dit proefschrift draait om stromingsberekeningen (vloeistof-, of gasdynamica, *hydrodynamica*) voor het gas en het stof in de wind van AGB-sterren. We (onderzoek doe je niet alleen) hebben onderzocht wat de invloed van het stof op de aandrijving van de wind is als *niet* wordt aangenomen dat gas en stof voortdurend met dezelfde snelheid bewegen. In stromingsberekeningen wordt de ruimte (in dit geval een schil om de ster heen) in kleine cellen opgedeeld en de tijd in stapjes. Vervolgens wordt voor iedere tijdstap, in iedere cel berekend (zie figuur 4):

1. Hoeveel gas de cel in stroomt in de tijdstap (*flux-in*).
2. Hoeveel gas de cel uit stroomt (*flux-uit*).
3. Hoeveel gas er bijkomt in de cel op andere manieren dan door instroming, bijvoorbeeld door het verdampen van stof dat aanwezig was in de cel (*positieve 'bronnen'*).
4. Hoeveel gas er verdwijnt op andere manieren dan door uitstroming, bijvoorbeeld door condensatie van gas tot vaste stof (*negatieve 'bronnen'*).

Hetzelfde wordt gedaan voor het stof. Op deze manier kan voor ieder tijdstip, op iedere plaats worden bepaald hoeveel gas en stof aanwezig is. Op vergelijkbare manier wordt bepaald hoe op ieder tijdstip de snelheid van gas en stof is. Bij dat laatste houden we

positieve bron: gas ontstaat
in cel i door b.v. verdamping

negatieve bron: gas verdwijnt
uit cel i door b.v. condensatie

gas stroomt van cel i–1
naar cel i

gas stroomt cel i uit,
naar cel i+1

FIGUUR 4: Het principe van hydrodynamica berekeningen. Voor iedere cel, hier voor cel i, wordt bepaald hoeveel er instroomt vanuit de stroomafwaarts gelegen buurcel $(i - 1)$ en hoeveel er uitstroomt naar de volgende cel $(i + 1)$. Ook de toevoer en afvoer door de bronnen wordt in rekening gebracht.

ook rekening met de botsingen tussen beide, waarin het stof snelheid overdraagt aan het gas.

Tevens berekenen we voortdurend de chemische samenstelling van het gas (hoeveel koolstof is er, en hoeveel waterstof, komt koolstof voornamelijk voor in atomaire vorm, of zijn er moleculen?). Daaruit berekenen we weer hoeveel gas er condenseert tot stof of hoeveel stof er verdampt en weer gasvormig wordt. Daarnaast wordt de temperatuur van gas en stof bepaald uit de intensiteit van de straling en de verdeling van de materie (dichtheid) rondom de ster.

Al met al moet er heel wat berekend worden en het is onmogelijk dat uit het hoofd of op papier te doen. Dit onderzoek bestond dan ook voor een groot deel uit het schrijven van een computerprogramma dat al deze berekeningen uitvoert. Het programma is zo ontworpen dat, na het invoeren van de temperatuur, massa, lichtkracht en chemische samenstelling van de ster (en eventueel de sterkte van de pulsaties aan het oppervlak), alles vanzelf gaat. Dat betekent dat verder geen aannamen gemaakt dienen te worden over bijvoorbeeld de grootte van het stof en de plaats waar het vormt en dat de ontwikkeling van de wind dus heel natuurgetrouw nagebootst wordt.

BELLEN BLAZEN...

Toen het hydrodynamica programma klaar was[4] en we er de schil om de ster IRC +10216 (in het sterrenbeeld Leeuw) mee simuleerderen, zagen we tot onze stomme verbazing dat de wind soms sterk was en dan weer zwak. De tijdschaal van de variaties in de uitstroming was een paar honderd jaar. We zouden onmiddellijk op zoek zijn gegaan naar de fout in ons programma als niet ongeveer tegelijkertijd waarnemingen

[4]Eigenlijk is zo'n computer-programma nooit klaar, want het is een model, en als wetenschappers het over een model hebben bedoelen ze een *versimpelde weergave van de werkelijkheid*. En een versimpeling is per definitie niet volledig.
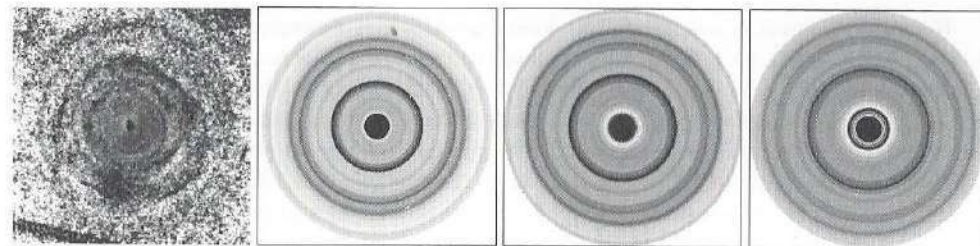
FIGUUR 5: Linker figuur: de schillen rond de ster IRC+10216 zoals waargenomen door Mauron & Huggins in 1999. Overige figuren: onze simulatie van deze schillen op drie verschillende tijdstippen tijdens de AGB-fase.

van deze ster gedaan waren die een schilstruktuur om de ster lieten zien. Deze kan ontstaan als er afwisselend veel en weinig gas bij de ster vandaan stroomt, dus als de wind afwisselend dicht en ijl is. De schillen die de waarnemers zagen bleken zeer veel gelijkenis te tonen met de schillen die geproduceerd worden door onze variabele wind, ze waren ongeveer net zo dik en ook de onderlinge afstand klopte (zie figuur 5). Omdat bekend is dat de uitstroming met een snelheid van tien tot twintig kilometer per seconde plaatsvindt, kan uit de afstand tussen de schillen worden afgeleid hoeveel tijd er zit tussen de vorming van twee achtereenvolgende schillen. Deze was, net als in onze model berekeningen een paar honderd jaar. Het leek er dus op dat een of andere instabiliteit in de hydrodynamica de oorzaak was van de schillen. Maar meer dan dat wisten we ook niet. We hadden in ons computermodel immers maar een paar gegevens van de ster ingevoerd waarna de ontwikkeling van de wind zonder verder ingrijpen werd berekend.

Toch blijkt hier het nut van computersimulaties. Het is immers moeilijk experimenteren met sterren. Tegen een ster zeggen: "Hé doe dat nog eens, ik snap nog niet hoe het werkt." is weinig zinvol, maar een computersimulatie start doe je gewoon even opnieuw. Door goed te kijken hoe gas en stof bewogen en van samenstelling veranderden kwamen we tot de volgende verklaring voor de wind-variaties.

Stel dat het gas een hoge dichtheid heeft, dan zijn er veel gasdeeltjes aanwezig en het versnelde stof zal dus vaak in botsing komen met gas. Het stof beweegt dan langzaam door het gas en blijft relatief lang dichtbij de ster. Daar is de dichtheid van het gas hoger dan verder naar buiten en is het gebied waar stofdeeltjes efficiënt kunnen groeien (door gas dat neerslaat op hun oppervlak). Een stof-deeltje dat langzaam door de groeizone beweegt zal dus groot (een paar micrometer) kunnen worden. De stofbevolking zal daarom bestaan uit relatief weinig, maar grote stofdeeltjes. De gezamenlijke oppervlakte van dit stof is veel kleiner dan de oppervlakte van een gelijke stofmassa die verdeeld is over heel veel kleine deeltjes. Precies zoals het schillen van een kilo grote aardappelen veel minder werk is dan het schillen van een kilo kleintjes: minder oppervlak per massaeenheid. Ons langzame stof dat de neiging heeft groot te worden heeft dus bovendien een vrij klein totaal oppervlak, en zal daarom betrekkelijk weinig straling van de ster onderscheppen en niet heel erg versneld worden. Dus: *langzaam stof wordt groter*, en *groot stof wordt langzamer*. Het langzame stof zorgt echter wel voor een heel efficiënte versnelling van het gas, dat in grote hoeveelheden bij de ster vandaan stroomt.

Het andere geval is ook mogelijk: kleine stofdeeltjes bewegen snel door het gas en blijven klein, want ze hebben niet genoeg tijd om te groeien. Het stof bestaat dan uit kleine deeltjes, die een groot oppervlak in verhouding tot hun gewicht hebben en efficiënt worden versneld maar minder vaak botsen met gas, omdat ze kleiner zijn. In dit geval vinden relatief weinig botsingen tussen stof en gas plaats en het gas wordt minder hard meegesleurd door het stof. Omdat het stof maar 1% van de totale materie was, is de wind op dit moment erg ijl. De kleine stofdeeltjes kunnen echter niet eeuwig kleiner en sneller worden. Immers, hoe sneller ze gaan, hoe vaker en hoe krachtiger de botsingen zullen zijn. Omdat de hoge snelheid de botsings-efficiëntie op twee manieren beïnvloedt, zal dit effect uiteindelijk sterker zijn. Alsof ze hun parachutes openen zullen de stofdeeltjes onmiddellijk afremmen, heel efficiënt het gas meeslepen en groter worden. De overgang van snel en klein stof en een zwakke wind naar de fase van groot en langzaam stof en een sterke wind is daarmee een feit.

Onopgemerkt wordt door die overgang ook al de volgende overgang (naar opnieuw een ijle wind met snel en klein stof) ingezet. Omdat de stofdeeltjes plotseling heel veel gas bij de ster vandaan slepen neemt de hoeveelheid gas in de laagste lagen van de schil af. Een verdunningsgolf beweegt daardoor naar de ster toe. Wanneer de verdunning van het gas door de stofvormingszone trekt worden de condities voor stofgroei daar ongunstiger. De hoeveelheid gas die kan condenseren neemt immers af. Een nieuwe generatie stof zal daarom weer uit kleine deeltjes bestaan, die snel door het gas bewegen, enzovoort. Op deze manier wisselen periodes van dichte en ijle wind elkaar af. Dit gebeurt overal rondom de ster, en dus zien we schillen of bellen met veel gas en en met weinig gas.

Hiermee is de cirkel rond. De tijdschaal waarop de windvariaties plaatsvinden wordt blijkbaar bepaald door de tijd die de verdunningsgolf nodig heeft om het stofvormings-gebied te doorkruisen. Essentieel voor het optreden van windvariaties is het feit dat het stof groter of kleiner kan worden, afhankelijk van de omgeving waarin het zich bevindt en de mogelijkheid dat het stof een andere snelheid heeft dan het gas. Ons programma was het eerste model waarin deze aspecten gecombineerd zijn, daarom waren voorheen geen windvariaties gevonden in modellen.

...DOE JE ALLEEN ALS JE JONG BENT

Hoewel om steeds meer planetaire nevels schillen worden gevonden, zijn er ook waar ze zeker niet zijn waargenomen. Blijkbaar treden modulaties dus lang niet altijd op en is de wind vaak ook 'glad'. Ook is het opvallend dat de schillen altijd aan de buitenkant van de planetaire nevel zitten.

Wij hebben onderzocht voor welke AGB-sterren er modulaties in het massaverlies optreden, en voor welke niet. Daartoe hebben we berekeningen gedaan voor sterren met verschillende massa, temperatuur en lichtkracht.

Eerder is al aan bod gekomen dat sterren in de AGB-fase steeds koeler en licht-krachtiger worden. Daarnaast neemt hun massa af, omdat ze door hun wind materie verliezen. Uit onze modelberekeningen volgt dat de koelste, lichtste en lichtkrachtigste en dus de oudste reuzen relatief weinig variaties in hun wind kennen. Hun massaverlies is constant hoog. Bij de iets jongere reuzen treden de modulaties in de wind wel op.

Hun gemiddelde massaverlies is låger. In de allerjongste reuzen, die nog relatief heet, zwaar en weinig lichtkrachtig zijn blijkt het stof nauwelijks in staat het gas mee te slepen.

Deze resultaten komen overeen met wat er is waargenomen. Uit het feit dat de schillen steeds aan de buitenkant van de nevel gevonden worden valt af te leiden dat een ster op 'jonge' leeftijd een wind met modulaties heeft en pas daarna een gladde wind ontwikkelt.

EN VERDER?

Hoe het de reuzenster vergaat nadat hij bellen heeft geblazen in z'n schil is bekend. Hij wordt een witte dwerg met een planetaire nevel eromheen. De restanten daarvan wor-den keurig gerecycled in de interstellaire ruimte, en wellicht ooit opnieuw samengeperst tot een ster uit een volgende generatie.

Dat voor de astronomen hiermee de kous af is, is een illusie. Al het hierboven beschreven onderzoek is slechts een model, waaraan nog jarenlang details toegevoegd kunnen worden om het nog realistischer te maken. De huidige versie van het pro-gramma kan bijvoorbeeld slechts de ontwikkeling van bolvormige strukturen om AGB-sterren berekenen. Als de AGB-ster z'n schillen uitblaast vormt dat geen beperking, want waarnemingen tonen aan dat die schillen inderdaad bolvormig zijn. Maar de planetaire nevel, die bestaat uit het gas dat tijdens de laatste, gladde en zeer dichte windfase is uitgeblazen, is meestal niet bolvormig, zie figuur 2. Het is de bedoeling het programma hieraan aan te passen. Een andere beperking van het huidige programma is dat het slechts een heel klein deel van de AGB-fase modelleert. Door steeds de massa, temperatuur en lichtkracht aan te passen kunnen we nu wel een beetje nagaan hoe de ster zich op de lange termijn ontwikkelt, maar eigenlijk zouden we liever veel langere berekeningen doen, waarbij dit tussentijds ingrijpen niet meer nodig is.

CURRICULUM VITAE

Ik ben geboren op 31 augustus 1972, in Purmerend. Daar heb ik de eerste 19 jaar van mijn leven gewoond en doorliep ik aan het Ignatius College het atheneum. Na mijn eindexamen, in 1990, begon ik met de studie wiskunde aan de Universiteit van Amsterdam. Een jaar later schreef ik me ook in voor natuurkunde. De propedeuses haalde ik in respectievelijk 1991 en 1992.

Na twee jaar gecombineerde studie besloot ik me voorlopig te richten op de theoretische natuurkunde. Het doctoraaldiploma behaalde ik in 1996. Met de keuze voor mijn afstudeeronderzoek zette ik een tweede ommezwaai in gang, ditmaal richting sterrenkunde: onder leiding van dr. Leo van den Horn bestudeerde ik criteria voor het optreden van convectie in supernovae.

Sinds 1996 heb ik onder *super*visie van prof. dr. Vincent Icke aan de Sterrewacht Leiden gewerkt aan de totstandkoming van dit proefschrift, aanvankelijk als beurspromovendus en later als assistent-in-opleiding (AIO). Daarnaast was ik enige tijd verantwoordelijk voor het onderhouden van de 'preprint bibliotheek', ben ik lid geweest van de sociale commissie en heb ik als begeleider deelgenomen aan een zomerschool voor scholieren. Ook ben ik assistent geweest bij het interacademiaal college sterrenkunde en het eerstejaars college inleiding astrofysica, beide gedoceerd door prof. dr. Vincent Icke.

Tijdens mijn promotieonderzoek heb ik deelgenomen aan zomer-, herfst-, en winterscholen in respectievelijk Brussel en Oslo, Dwingeloo en Les Diablerets (Zwitserland). Daarnaast heb ik symposia, conferenties en bijeenkomsten bezocht in Noordwijkerhout, Groningen, Garching (Duitsland), Montpellier (Frankrijk), Wenen, Cambridge (Verenigde Staten), Amsterdam en Torun (Polen). Ik ben de Leidse Sterrewacht, het Leids Kerkhoven Bosscha Fonds en NWO dankbaar voor de financiële ondersteuning voor deze reizen.

Als theoreticus heb ik het genoegen gehad een keer deel te nemen aan waarnemingen. Het betrof observaties van actief stervormende ('starburst') sterrenstelsels met de JKT (La Palma), als assistent van dr. Matt Lehnert.

Na mijn promotie zal ik mijn werkzaamheden voortzetten als post-doc aan het Astrophysikalisches Institut Potsdam (Duitsland), waar ik zal werken in de groep van prof. dr. Detlef Schönberner.

NAWOORD

Het is helaas niet mogelijk op deze plaats iedereen die op de één of andere manier heeft bijgedragen aan de totstandkoming van dit proefschrift te noemen. Ik vertrouw erop dat zij die hun naam hier niet zien staan weten waar zij bedoeld worden.

Het beoefenen van de wetenschap is een kunst. Ik bewonder de kunstenaars die mijn voorbeelden zijn en prijs mezelf gelukkig dat ik met ze heb kunnen samenwerken. Dat heb ik ruim vijf jaar en met heel veel plezier gedaan op de Sterrewacht Leiden. Veel meer sterrewachters dan ik hier kan noemen, van toen tot nu, hebben daaraan bijgedragen. Kees, het was een genoegen kamer 569 met je te delen, de overlap van onze werktijden was perfect: genoeg tijd om over van alles en nog wat te overleggen en voor beiden de ruimte om rustig te werken. Inga, door jouw komst werd onze kamer een gezellig oerwoud. Het enthousiasme waarmee je met mijn code aan de slag ging heeft me erg geholpen en m'n Duits is met sprongen vooruit gegaan. Garrelt, ook jouw (terug)komst naar de Sterrewacht en, ook daarvoor al, je betrokkenheid bij mijn werk, hebben me goed gedaan. Waardevol commentaar op stukken van de tekst kreeg ik van Marijke en Maria-Rosa. Van enig plezier in het werk op de Sterrewacht was geen sprake geweest zonder de perfecte ondersteuning van de systeemgroep en het secretariaat: Aart, David, Erik, Tycho, Janet, Jeanne, Kirsten, Marja en Yoke verdienen het daarvoor genoemd te worden.

Zware lichamelijke inspanning is de beste afleiding die er is. Alle sportievelingen van US, de meiden van Primavera en die van de zondaggroep en alle anderen: het was leuk samen met jullie te trainen op de schaats, de fiets, in het bos, en in bergachtige oorden. Gerbrand, fijn dat je m'n Nederlandse samenvatting hebt gelezen.

Geen aio, post-doc of gewoon-reizende te ver of de BBX-mail weet hem te bereiken. Zonder de mailtjes en de daaruit voortvloeiende wandelweekeindes, spellen in het park, theater- en cafébezoeken was het lang zo leuk niet geweest. En zonder de uitwisseling van LaTeXtips en stylefiles was dit proefschrift nu nog niet afgeweest. Frank, ik ben je zeer erkentelijk voor je betrokkenheid, de discussies en figuur 1.2. Coen, ik blij dat er nog meer mensen zijn die graag een uur nadenken over de juiste formulering van twee regels tekst.

Brenda, Lieseth, Sonja en Carola. Met jullie heb ik ook de nodige pagina's geschreven. Het is nog altijd leuk ze terug te lezen. Ik hoop dat we elkaar nog lang blijven zien!

Ik ben trots op mijn enorm veelzijdige (schoon)familie, en dankbaar voor hun betrokkenheid. Zo'n divers nest is bovendien enorm handig. Want wat kan een promovendus in haar laatste maanden zich nu nog meer wensen dan een vader en een broer met oog voor vormgeving en een enorme collectie grafische software; een zus voor onder meer stijl- en spellingsproblemen; en een moeder en nog een zus om examen-stresservaringen mee uit te wisselen? Lieve Jos en Wil, Annegien en Martin, Stefan, Leontien en Olaf, ik doe jullie te kort door te zeggen dat jullie aanwezigheid 'wel handig' is; want het is heel veel meer dan dat. Lieve Ruud, de laatste woorden zijn voor jou. Jij was er steeds wanneer ik je nodig had en zéker wanneer ik weer eens dacht het allemaal zelf te kunnen.